Doctoral Dissertation
博士論文

Search for Neutrinos associated with Solar Flares in Super-Kamiokande

(スーパーカミオカンデにおける太陽フレア由来のニュートリノ探索)

A Dissertation Submitted for the Degree of Doctor of Philosophy

December 2021
令和 3 年 12 月博士 (理学) 申請

Department of Physics, Graduate School of Science,
The University of Tokyo
東京大学大学院理学系研究科
物理学専攻

Kohei Okamoto
岡本 幸平

Abstract

Neutrinos associated with solar flares (solar flare neutrinos) provide information on particle acceleration mechanisms during the impulsive phase of solar flares. Solar flare neutrino search was conducted using the Super-Kamiokande detector with search time windows set by using data from solar observation satellites. Furthermore, we have established another approach to set the search windows for solar flare neutrinos analyzing the data of coronal mass ejections, and then performed the first attempt to search for neutrinos from solar flares occurring on the invisible side of the Sun. Twenty-three solar flares above the X5.0 class were selected which occurred on the visible side of the solar surface between April 1996 and May 2018. And ten solar flares were selected from the invisible side which accompanies with coronal mass ejections whose emission speed is faster than 2000 $\mathrm{km\,s^{-1}}$. Then, the neutrino events coincident with the solar flares were searched for using the Super-Kamiokande detector. The Super-Kamiokande data is divided into two samples as high-energy samples (above 100 MeV) and low-energy samples (16 - 100 MeV). For the solar flares occurring on the visible side of the Sun, there are two solar flares occurring on the visible side of the Sun with one high-energy neutrino candidate in the search time windows. For the other eighteen solar flares on the visible side, there are not any neutrino candidates. The solar flares with the neutrino candidate occurred on November 4th, 2003, and September 6th, 2017, and expected background rates are 0.20 event/flare and 0.12 event/flare, respectively. They are statistically consistent with the expected background rate. For the solar flares occurring on the invisible side, there are two solar flares with two high-energy neutrino candidates and two solar flares with one high-energy neutrino candidate. There are not any neutrino candidates with the other solar flares. The expected background rate for each solar flare on the invisible side is 0.62 event/flare. They are statistically consistent with the expected background rate. Therefore, the upper limit of solar flare neutrino fluence at 90% confidence level was calculated for each solar flare. The fluence upper limits at 90% confidence level for the solar flares occurring on the visible side of the Sun without neutrino candidates are 5.6×10^5 $\mathrm{cm^{-2}}$. For the solar flares occurring on the invisible side, The fluence upper limits at 90% confidence level in the energy region from 100 MeV to 10 GeV are 5.6×10^5 $\mathrm{cm^{-2}}$, 8.2×10^5 $\mathrm{cm^{-2}}$ and 1.2×10^6 $\mathrm{cm^{-2}}$ for solar flares with zero, one and two neutrino candidates, respectively. From the obtained fluence upper limits, the upper limits on the conversion factor, η, which is the efficiency of energy conversion from the total energy of solar flare to the energy of the neutrinos, is estimated. In the case of the largest solar flare on November 4th, 2003, it is determined as $\eta < 0.004$, which is two orders of magnitude smaller than the estimation by Fargion and Moscato. Therefore, this experimental result suggests that the theoretical assumption of the energy conversion during solar flares should be re-considered. In addition, the fluence upper limit at 90% confidence level for the solar flare occurring on the invisible side on November 7th, 2003, which followed the largest solar flare, is 1.2×10^6 $\mathrm{cm^{-2}}$. The fluence upper limits at 90% confidence level in the energy region from 16 to 100 MeV for the solar flares occurring on the visible and invisible side of the Sun are 1.7×10^7 $\mathrm{cm^{-2}}$. In order to compare the results with the other experimental fluence limits, the

model independent fluence upper limit below 100 MeV is also obtained. The result does not rule any theoretical models but gives the most stringent upper limits on the fluence of solar flare neutrinos in the tens of MeV region.

Acknowledgments

I would first like to express my gratitude to Prof. Masayuki Nakahata for giving me the opportunity to do research at Super-Kamiokande. He showed me around the Kamioka Mine even before I entered the graduate school and gave me a historical background of the Kamiokande from its beginning to the present. He also gave me various advice and support for my research. I would not have been able to complete this research without his support.

I would like to thank Dr. Yuuki Nakano for giving me so much of his time to help me with all aspects of the radon detector calibration experiments and solar flare research. He taught me how to connect pipes, how to make slide presentations, and how to analyze data from Super-Kamiokande. In addition to my research, I also learned how to prepare for drinking parties and delicious food in Toyama, which made my research in Kamioka enjoyable.

Prof. Yoshitaka Itow of Nagoya University provided me with the necessary environment to conduct research on solar flares and taught me the basics.

Associate Professor Satoshi Masuda of Nagoya University taught me the basics of how to analyze data from solar observation satellites and how to accelerate particles in solar flares. Thanks to Dr. Masuda, I have a better understanding of solar flares.

Dr. Shintaro Ito of KEK analyzed the high-energy data in the search for neutrinos from solar flares, and made the event displays.

I would like to express my gratitude to Associate Professor Hiroyuki Sekiya for providing me with various experimental materials, including the detector itself, and a lot of advice on the calibration experiment of the radon detector. When I broke the radon detector due to my carelessness, he encouraged me to find out what the cause was as soon as possible and to restore it immediately.

Prof. Yasuo Takeuchi of Kobe University gave me advice on calibration experiments of radon detectors and data analysis of Super-Kamiokande. He also came to our drinking party and offered us some delicious drinks.

I would like to thank my members in Kamioka, Dr. Asato Orii, Dr. Masatoshi Kobayashi, Dr. Ryosuke Akutsu, Mr. Yutaro Sonoda, Dr. Akira Takenaka, and Mr. Takumi Suzuki, Nobuyuki Kato, Pedersen Juan William, and Toshiki Mochizuki for making my life in Kamioka enjoyable.

I would like to express my sincere gratitude to my high school baseball teammates, Ryo Abe, Rin Abe, Ryo Izaki, Tomoyuki Ito, Ryosuke Oshima, Arata Okawa, Kaoru Okamoto, Takuya Kijima, Yuji Sunazuka, Toshiyuki Tanaka, Tsubasa Tsuchiya, Shotaro Tsunoda, Hiroshi Nagatomi, Hiroshi Nagayama, Ryosuke Ninomiya, Yudai Hakata, Tatsumi Hiraga, Naoya Fukushima, Yunosuke Hosokawa, Yuji Norihashi, Shunpei Murakami, Masayuki Yokoyama, Wataru Yoneda, and Yuta Watanabe, for their continuous support and friendship even after graduating from high school.

Finally, I would like to express my sincere gratitude to my family for their support.

Contents

List of Figures

List of Tables

Chapter 1

Introduction to Solar Flares and Neutrinos

In this chapter, the physics of neutrinos, solar flares, and neutrino emission associated with solar flares are discussed.

1.1 Neutrinos

Neutrinos are elementary particles with no electric charge and interact with other particles via the weak force and gravity only. Neutrinos interact with other matter only rarely, so if neutrinos which are produced by high-energy phenomena in the universe can be observed, they can be used to investigate phenomena occurring at the source. So far, neutrinos from fusion reactions at the center of the Sun [1], supernova explosions [2] and Blazer [3] have been observed.

1.1.1 Neutrino oscillation

One of the important properties of neutrinos is neutrino oscillation. They were thought to be particles with zero mass in the standard model of particle physics. However, neutrino oscillation was discovered with observations of atmospheric and solar neutrinos, with the consequence that neutrinos have masses [4, 5]. The flavor eigenstates of neurinos, $|\nu_\alpha\rangle$ ($\alpha = e, \mu, \tau$), can be expressed as superposition of their mass eigenstates, $|\nu_i\rangle$ ($i = 1, 2, 3$):

$$|\nu_\alpha\rangle = \sum_i U_{\alpha i} |\nu_i\rangle , \tag{1.1.1}$$

where U is a 3×3 unitary matrix which is call Pontecorvo-Maki-Nakagawa-Sakata (PMNS) matrix [6, 7]. This PMNS matrix can be written by using 4 independent parameters, which are mixing angles $\theta_{12}, \theta_{23}, \theta_{13}$ and the Charge-Parity (CP) violation phase $\delta_{\rm CP}$:

$$\begin{aligned} U &= \begin{pmatrix} 1 & 0 & 0 \\ 0 & c_{23} & s_{23} \\ 0 & -s_{23} & c_{23} \end{pmatrix} \begin{pmatrix} c_{13} & 0 & s_{13}e^{-i\delta_{\rm CP}} \\ 0 & 1 & 0 \\ -s_{13}e^{i\delta_{\rm CP}} & 0 & c_{13} \end{pmatrix} \begin{pmatrix} c_{12} & s_{12} & 0 \\ -s_{12} & c_{12} & 0 \\ 0 & 0 & 1 \end{pmatrix} \\ &= \begin{pmatrix} c_{12}s_{13} & s_{12}c13 & s_{13}e^{-i\delta_{\rm CP}} \\ -s_{12}c_{23} - c_{12}s_{13}s_{23}e^{-i\delta_{\rm CP}} & c_{12}c_{23} - s_{12}s_{13}s_{23}e^{i\delta_{\rm CP}} & c_{13}s_{23} \\ s_{12}s_{23} - c_{12}s_{13}c_{23}e^{i\delta_{\rm CP}} & c_{12}s_{23} - s_{12}s_{13}c23e^{i\delta_{\rm CP}} & c_{13}c_{23} \end{pmatrix}, \end{aligned} \tag{1.1.2}$$

where $c_{ij} = \cos\theta_{ij}$ and $s_{ij} = \sin\theta_{ij}$. If $\sin\delta_{\rm CP} \neq 0$, the PMNS matrix contains imaginary parts, which cause CP violation. In vaccum, the time evolution of of a mass eigenstate can be derived from the Schrödinger equation,

$$i\frac{\mathrm{d}}{\mathrm{d}t}\left|\nu_i(t)\right\rangle = \mathcal{H}\left|\nu_i(t)\right\rangle = E_i\left|\nu_i(t)\right\rangle \tag{1.1.3}$$

$$\left|\nu_i(t)\right\rangle = \exp(-iE_it)\left|\nu_i(0)\right\rangle, \tag{1.1.4}$$

where E_i is the energy of mass eigenstate, $\mathcal{H}$ represents Hamiltonian and t is a travering time of the neutrino. From Eqs. 1.1.1 and 1.1.4, The flavor eigenstate $|\nu_\alpha\rangle$ at a time t can be written as

$$\left|\nu_\alpha(t)\right\rangle = \sum_i U_{\alpha i}\exp(-iE_it)\left|\nu_i(0)\right\rangle \tag{1.1.5}$$

When the mass of a neutrinos, m_i^2, are too small compared to their momenta, $\boldsymbol{p}_i$, an approximation,

$$E_i = \sqrt{p_i^2 + m_i^2} \approx p_i + \frac{m_i^2}{2p_i} \approx p + \frac{m_i^2}{2E_i}, \tag{1.1.6}$$

where the neutrino energy, expressed as $E \sim |p_i| \sim |p_j|$. Then, Eq. 1.1.5 becomes as following:

$$\begin{aligned}\left|\nu_\alpha(t)\right\rangle &= \sum_i U_{\alpha i}\exp(-ipt)\exp(-\frac{im_i^2t}{2E})\left|\nu_i(0)\right\rangle \\ &= \sum_{i,\beta} U_{\alpha i}\exp(-ipt)\exp(-\frac{im_i^2t}{2E})U^\dagger_{\beta i}\left|\nu_\beta\right\rangle.\end{aligned} \tag{1.1.7}$$

the $\nu_\alpha \to \nu_\beta$ transition probability $P(\nu_\alpha \to \nu_\beta)$ is calculated as:

$$\begin{aligned}P(\nu_\alpha \to \nu_\beta) &= |\left\langle\nu_\beta|\nu_\alpha(t)\right\rangle|^2 \\ &= |\sum_{i,\beta} U_{\alpha i}\exp(-ipt)\exp(-\frac{im_i^2t}{2E})U^\dagger_{\beta i}|^2 \\ &= \sum_{i,j} U^\dagger_{\alpha i}U_{\beta i}U_{\alpha j}U^\dagger_{\beta j}\exp\left(-\frac{i(m_i^2-m_j^2)t}{2E}\right) \\ &= \sum_{i,j} U^\dagger_{\alpha i}U_{\beta i}U_{\alpha j}U^\dagger_{\beta j}\exp\left(-\frac{i\Delta m_{ij}^2L}{2E}\right) \\ &= \delta_{\alpha\beta} - 4\sum_{i>j}\mathrm{Re}(U^\dagger_{\alpha i}U_{\beta i}U_{\alpha j}U^\dagger_{\beta j})\sin^2(\frac{\Delta m_{ij}^2L}{4E}) \\ &+ 2\sum_{i>j}\mathrm{Im}(U^\dagger_{\alpha i}U_{\beta i}U_{\alpha j}U^\dagger_{\beta j})\sin(\frac{\Delta m_{ij}^2L}{2E})\end{aligned} \tag{1.1.8}$$

where $\Delta m_{ij}^2 \equiv m_i^2 - m_j^2$ is a mass-squared difference, t is replaced with a travel distance $L = ct$ and $\delta_{\alpha\beta}$ is the Kronecker's delta. According to this equation, neutrino oscillation will happen when at least two neutrino masses are not degenerate ($m_i \neq m_j$) and there is nonzero mixing angle ($\theta_{ij} \neq 0$). Neutrino oscillation in a vauum can be described by six parameters: three mixing

angles ($\theta_{12}, \theta_{23}, \theta_{13}$), two mass squeared difference[1] ($\Delta m^2_{12}, \Delta m^2_{23}$), and a CP phase ($\delta_{\rm CP}$). These parameters have been measured by using various neutrino sources: solar, reactor, atmospheric and accelerator neutrinos. The parameters $\theta_{12}, \Delta m^2_{12}$ are measured by solar neutrino experiments [8–10]. Atmospheric neutrino and accelerator neutrino experiments [11–14] established the parameters, $\theta_{23}, \Delta m^2_{23}$. Measurements at reactor experiments [15–17] established that the mixing angle, θ_{13}, was small but nonzero. The value of the CP phase ($\delta_{\rm CP}$) is still unknown but Tokai to Kamioka (T2K) experiment [18] showed non-zero $\delta_{\rm CP}$ with 95% Confidence Level (C.L.). The best fit values of global analysis of neutrino data are summarized in Table. 1.1. There are two possibilities of mass hierarchy, which depend on the ordering of the neutrino mass eigenstates. The order, $m_1 < m_2 < m_3$ ($m_3 < m_1 < m_2$), is called to Normal Ordering (NO) (Inverted Ordering (IO)).

Table 1.1: Three flavor ν oscillation parameters obtained from different global analysis of neutrino data. In all cases the numbers labeled as NO (IO) are obtained assuming NO (IO), *i.e.*, relative to the respective local minimum.

Parameter	Best fit value
NO	
$\sin^2\theta_{12}[10^-1]$	$3.10^{+0.13}_{-0.12}$
$\sin^2\theta_{23}[10^-1]$	$5.63^{+0.18}_{-0.24}$
$\sin^2\theta_{13}[10^-2]$	$2.237^{+0.066}_{-0.065}$
$\delta_{\rm CP}[^\circ]$	221^{+39}_{-28}
$\Delta m^2_{21}[10^{-5}{\rm eV}]$	$7.39^{+0.21}_{-0.20}$
$\Delta m^2_{23}[10^{-3}{\rm eV}]$	$2.454^{+0.029}_{-0.031}$
IO	
$\sin^2\theta_{12}[10^-1]$	$3.10^{+0.13}_{-0.12}$
$\sin^2\theta_{23}[10^-1]$	$5.65^{+0.17}_{-0.22}$
$\sin^2\theta_{13}[10^-2]$	$2.259^{+0.065}_{-0.065}$
$\delta_{\rm CP}[^\circ]$	282^{+23}_{-25}
$\Delta m^2_{21}[10^{-5}{\rm eV}]$	$7.39^{+0.21}_{-0.20}$
$\Delta m^2_{23}[10^{-3}{\rm eV}]$	$-2.510^{+0.030}_{-0.031}$

[1] $\Delta m^2_{12} + \Delta m^2_{23} + \Delta m^2_{31} = 0$

1.2 The Sun and Its Activity

The sun is a multi-layered, spherical mass of gas that is composed of hydrogen and helium with a radius of about 7.0×10^5km. The structure is as follows:

- Core – The region where the nuclear fusion reaction occurs. Its size is about 1.0×10^5km, which is 20% of the solar radius.
- Radiative zone – In this region, convection cannot occur. Therefore, The energy generated in the core is transferred by means of radiation rather than by convection. It appears between 20% and 70% of the solar radius.
- Convective zone – between 70% of the solar radius and the visible surface.
- Photosphere – The light emitted to the outside of the Sun is generated in this layer, which corresponds to the visual stellar surface.
- Chromosphere – A dilute gas layer on the photosphere. It is several thousand to ten thousand kilometers thick.
- Corona – The Sun's corona extends 10 solar radii into outer space and is most easily seen during a total solar eclipse.

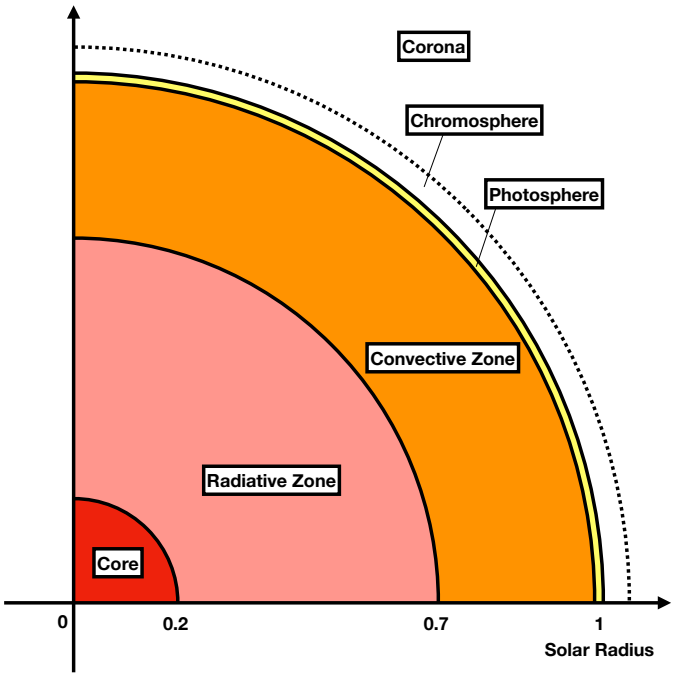

Figure 1.1: The schematic diagram of the Sun's layered structure. The scale is based on a solar radius as unit.

Solar activity goes through an 11-year cycle of activity and quiescence. As shown in Figure 1.2, the frequency of solar flares is synchronized with the sunspot number, and about 3,000 solar flare events are observed per year during the maximum season.

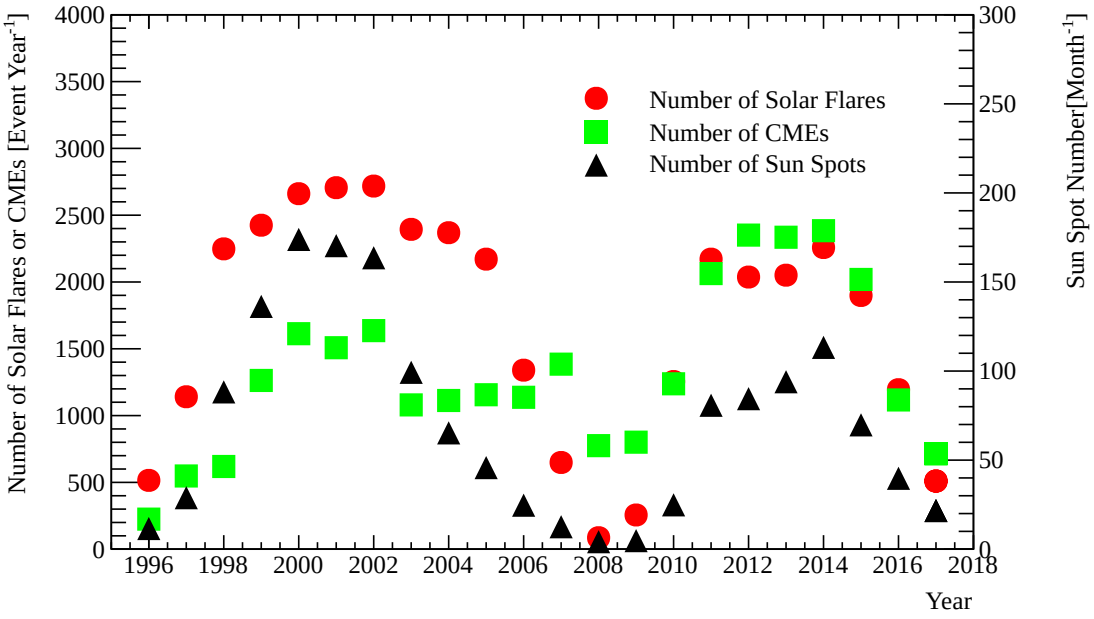

Figure 1.2: The yearly occurrence rate of the solar flares and CMEs, and the monthly variation of the number of the sun spots at the surface of the Sun during solar cycle 23 and 24. The number of solar flares, CMEs and sunspots are taken from NOAA's solar flare list[2], LASCO CME Catalog[3] and Sunspot Index and Long-term Soalr Observations[4], respectively.

[1]https://www.ngdc.noaa.gov/stp/solar/solarflares.html
[2]https://cdaw.gsfc.nasa.gov/CME_list/UNIVERSAL/1999_02/univ1999_02.html
[3]https://wwwbis.sidc.be/silso/datafiles

1.3 Solar Flares

A solar flare is a process in which magnetic energy is converted into thermal, kinetic, and particle acceleration energy in the outer layers of the solar atmosphere which is shown as chromosphere and corona in Fig. 1.1. The amount of energy generated by a single solar flare is typically $10^{26} - 10^{32}$ erg, making it the largest energy release event in the solar system. The typical timescale for energy release is $100 - 1000$ seconds based on electromagnetic wave observation [19]. Solar flares occur mainly in the vicinity of active regions which is seen as a sunspot. The frequency of flares depends on the solar activity cycle and can be more than 10 events per day during the maximum period, while it can be only one event per month during the minimum period as shown in Fig. 1.2. Figure 1.3 shows the relationship between the frequency of solar flares and their energy.

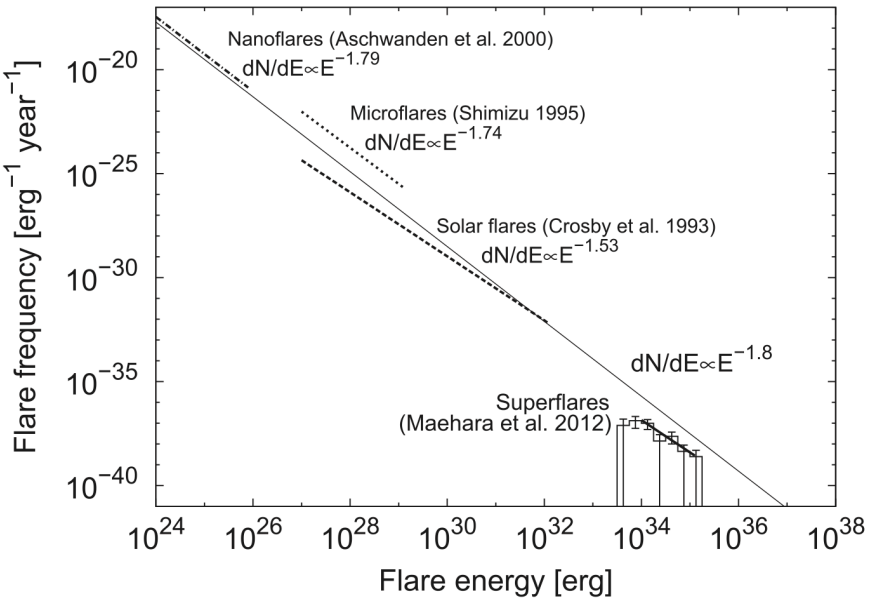

Figure 1.3: The frequency of solar flares as a function of their total energy. The higher the energy released, the smaller the frequency of flares [20].

Solar flares accelerate ionized particles, such as electrons and protons, and carry nonthermal energy from the acceleration site to the energy loss site in the chromosphere.

Neutral particles associated with solar flares are important to testify to theoretical aspects of particle accelerations in magnetic reconnection because they can escape from the acceleration site. Their observations reveal both spatial and time profiles of primary particle acceleration while primary and secondary charged particles are trapped by a magnetic field.

Magnetic Reconnection

Magnetic reconnection is thought to play an important role in solar flares because magnetic energy is converted into kinetic and thermal energy of particles in a short period which agrees with

solar flare observations. When antiparallel magnetic field lines are pressed against each other in the plasma, a surface current called a current sheet flows between them. As long as the current is flowing, the opposing lines of magnetic force do not connect, but if the current dissipates for some reason, the lines of magnetic force are reconnected, and the strong magnetic tension of the newly created lines of magnetic force causes the plasma to accelerate violently [21]. Figure 1.4 shows the schematic view of magnetic reconnection site. Figure 1.5 shows the numerical simulation result of magnetic reconnection. The numerical simulation of magnetic reconnection reproduces well the cusp shape as seen in soft X-ray observations.

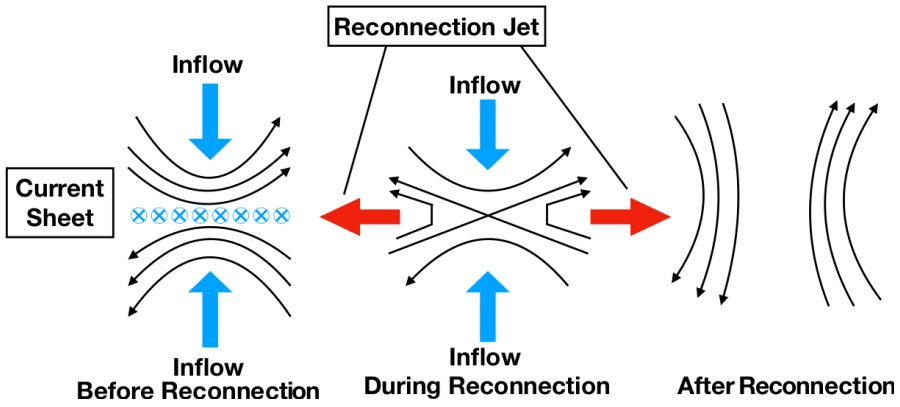

Figure 1.4: A schematic view of magnetic reconnection site. Black solid arrows show magnetic force lines, the light blue cross shows current which is perpendicular to the magnetic force. Based on Fig.1 of Ref. [21].

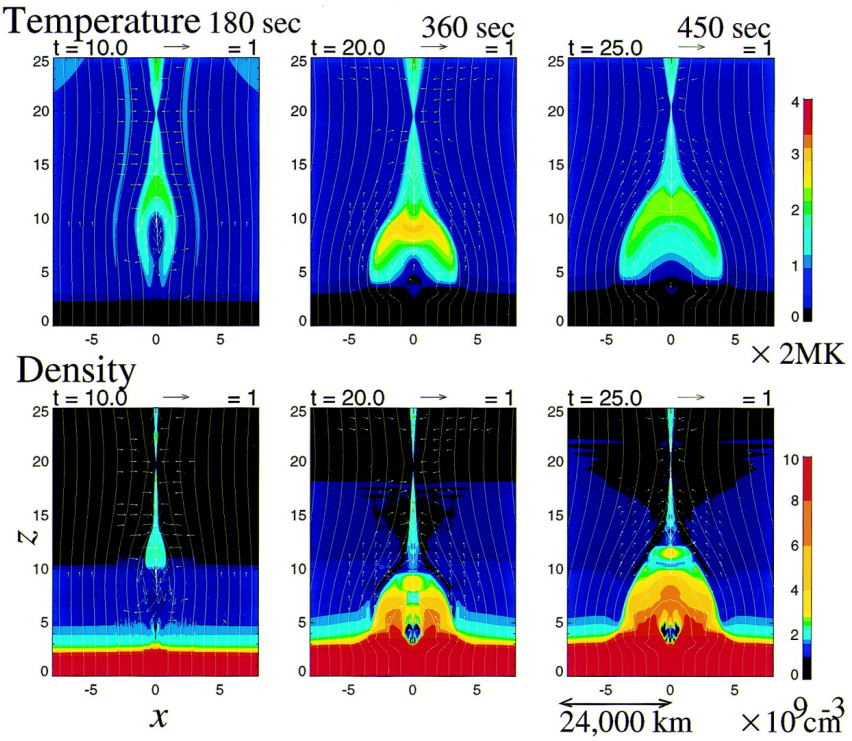

Figure 1.5: Numerical simulation results by T.Yokoyama and K.Shibata [22]. The top and bottom figures show the temporal evolution of temperature and density distribution, respectively. The arrows show the velocity, and the lines show the magnetic field lines. The units of length, velocity, time, temperature, and density are 3000 km, 170 kms^{-1}, 18 s, 2×10^6 K, and 10^9 cm^{-3} respectively. In the initial condition ($t = 0$) a dense region is located near the bottom of the simulation box in which the density is about 10^5 times that of another region.

1.4 Observations of Solar Flares

Solar flares have been observed since the first observation in 1859 with electromagnetic waves in various wavelength ranges. In this section, the observational information on solar flares which is used in this study are described.

1.4.1 Soft X-ray

Soft X-rays are originally produced by bremsstrahlung from electrons in thermal motion. Because the energy of a particle accelerated by a solar flare is finally converted into thermal energy, the total intensity of the soft X-ray is used to represent the total energy released by the solar flare. A peak value of the soft X-ray flux in the range of 1–8 Å (1.5–12 keV) observed by *Geostationary Operational Environmental Satellite* (GOES) is widely used as an indicator in the classification of solar flares. The correspondence between the classifications and the peak intensity of the X-rays is shown in Table 1.2. On the basis of this classification, a solar flare whose peak value exceeds 1.0×10^{-4} W/m^2 (X1.0 class) is considered to be the largest order [23].

Table 1.2: The Classification of a Solar Flare.

Solar Flare Class	Soft X-ray intensity [W/m^2]
A	10^{-8}–10^{-7}
B	10^{-7}–10^{-6}
C	10^{-6}–10^{-5}
M	10^{-5}–10^{-4}
X	$> 10^{-4}$

1.4.2 Hard X-ray

Hard X-rays are produced by bremsstrahlung from nonthermal electrons and the energy ranges from a few keV to MeV. Such non-thermal electrons are accelerated by the solar flare; hence they provide information about the energy distribution of the nonthermal electrons. Nonthermal electrons lose their energy by scattering in the solar atmosphere and eventually generate thermal bremsstrahlung. In contrast with soft X-rays, hard X-rays provide information about the electron acceleration site and its time frame.

It is empirically known that the peak times of the hard X-ray flux occur close to the inflection points of the soft X-ray light curve [24]. Therefore, by differentiating the light curve of soft X-rays with respect to time, we obtain a light curve similar to that of hard X-rays, and we can similarly extract information about electron acceleration.

1.4.3 γ-ray

Because neutrinos are produced via hadronic decay, the timing of these interactions should be identified in order to determine the search window. The time profile of γ-rays is the most important in this study because observation of γ-rays implies the acceleration and nuclear reactions of protons. In a solar flare, there are several different reactions which produce γ-rays; γ-rays due to bremsstrahlung from high energy electrons, γ-rays due to electron-positron annihilation, line γ-rays due to neutron capture on hydrogen nuclei, and γ-rays due to de-excitation from nuclei, such as carbon (^{12}C) and oxygen (^{16}O) [25,26]. Among these, line γ-rays due to neutron capture on hydrogen nuclei are the most important channel and are discussed below, along with γ-ray

emission due to neutral pions. Hard X-ray and γ-ray had been observed by *Reuven Ramaty High Energy Solar Spectroscopic Imager* (RHESSI) satellite from 2003 to 2018. This spacecraft was able to make an image of solar flares with 3 keV to 17 MeV energy range. So, not only temporal information but also the precise position of solar flares can be obtained from RHESSI's data.

1.4.4 Coronal Mass Ejection (CME)

CMEs are known as phenomena associated with solar flares. It is a shock wave of plasma which is accelerated in solar flare location. The observation of CMEs occurring on the invisible side of the Sun is performed by coronagraph method with the LASCO, the Large Angle Spectroscopic Coronagraph on the Solar and Heliospheric Observatory (SOHO) [27, 28]. The catalog of CMEs observed by the SOHO spacecraft is maintained by NASA [29][2] and this catalog summarizes the time of CMEs emission and its locations. CMEs can be observed even if the active region is on the invisible side of the Sun. Therefore, this information is useful for making a search time window for solar flares on the invisible side.

[2] `https://cdaw.gsfc.nasa.gov/CME_list/`

1.5 Particle Acceleration in Solar Flares

When solar flares occur, high-energy particles that do not normally exist in the solar atmosphere are observed. Therefore, the particles must be accelerated by some acceleration mechanism during solar flares, but it has not been clarified yet. In this section, candidates for the acceleration mechanism are described. It is noted that three candidates are listed below, but many other particle acceleration mechanisms have been considered and their combination is also possible.

Stochastic Acceleration (Fermi's second-order)

There is an acceleration mechanism called stochastic acceleration, which was proposed by E. Fermi in 1949 [30]. Charged particles are accelerated to high energy by repeated collisions with a molecular cloud with a magnetic field.

Consider the case where a charged particle with energy E and speed v_p collides with a molecular cloud moving at speed v_m [31]. The change in energy in one collision can be written as

$$\Delta E_\pm / E = \pm 2(v_\mathrm{m}/v_\mathrm{p}) \tag{1.5.1}$$

where ΔE_+ is the energy obtained in a head-on collision with a molecular cloud, and that in a rear collision is ΔE_-.

Frequency of frontal and rear collision per unit time R_front and R_rear are

$$R_\mathrm{rear} = \frac{1 + v_\mathrm{m}/v_\mathrm{p}}{t_\mathrm{coll}} \tag{1.5.2}$$

$$R_\mathrm{front} = \frac{1 - v_\mathrm{m}/v_\mathrm{p}}{t_\mathrm{coll}} \tag{1.5.3}$$

where t_coll is the average time taken from the first collision to the next one. Thus, the energy change per unit time can be written as

$$\frac{\mathrm{d}E}{\mathrm{d}t} = R_\mathrm{rear}\Delta E_+ + R_\mathrm{front}\Delta E_- = 4\left(\frac{v_\mathrm{m}}{v_\mathrm{p}}\right)^2 \frac{E}{t_\mathrm{coll}} \tag{1.5.4}$$

This is called quadratic acceleration because the increment in energy is proportional to the square of $v_\mathrm{m}/v_\mathrm{p}$. It takes a very long time for a charged particle to be accelerated to high energy since the speed of a molecular cloud v_m is very small compared to the speed of charged particle v_p. The application of statistical acceleration to particle acceleration in solar flares has been made by various theorists [32–36].

Shock Wave Acceleration

If the location of the stochastic acceleration process is near the shock wavefront, the collisions between the molecular cloud and the charged particles are not random, and more efficient acceleration occurs. This mechanism is most effective if shocks with an angle of the upstream magnetic field to the shock normal larger than 45° [37]. In this acceleration mechanism, the incremental energy of the particle is proportional to $v_\mathrm{m}/v_\mathrm{p}$.

Coherent Acceleration

The origin and strength of the electric field in a solar flare are not clear but acceleration models with an electric field have been considered. A possible way that an electric field will appear in a solar flare is magnetic reconnection. The first suggestion that particle acceleration is caused by magnetic reconnection in solar flares was made by Giovanelli [38]. Magnetic reconnection has been applied to solar flare models.

There have been several attempts to estimate the electric field produced by resistive tearing mode instability but the results disagree. The reason for the disagreement is that induced electric fields depend on the small-scale structure of the magnetic field and the transport properties of the instability.

1.6 Predictions for Solar Flare Neutrinos

Last several decades, an emission model of solar flare neutrinos has been theoretically discussed [39–44]. For example, Fargion and Moscato predicted a possibility of observing neutrinos from a large solar flare of energy greater than 10^{32} erg using Super-K and IceCube [42]. On the other hand, Takeishi et.al. predicted a rather small possibility of observing neutrinos even in Hyper-Kamiokande [45] by numerical simulations [44]. In this section, general knowledge of pion production by proton collision and the theoretical predictions of solar flare neutrino flux at the Earth will be introduced.

If protons are accelerated during solar flares to sufficiently high energies (more than about 300 MeV), pions are produced by collisions with other nuclei in the solar atmosphere [46, 47]. The main mechanism for the production of charged pions, the source of neutrinos, is as follows:

$$\mathrm{p} + \mathrm{p} \to \Delta^{++} + \mathrm{n} \to \mathrm{p} + \pi^{+} + \mathrm{n} \tag{1.6.1}$$

$$\mathrm{p} + \mathrm{p} \to \Delta^{+} + \mathrm{p} \begin{array}{l} \nearrow \mathrm{p} + \mathrm{p} + \pi^{0} \\ \searrow \mathrm{p} + \mathrm{n} + \pi^{+} \end{array} \tag{1.6.2}$$

or by scattering with neutrons, produced as follows:

$$\mathrm{p} + \mathrm{n} \to \Delta^{+} + \mathrm{n} \begin{array}{l} \nearrow \mathrm{n} + \pi^{+} + \mathrm{n} \\ \searrow \mathrm{p} + \pi^{-} + \mathrm{p} \end{array} \tag{1.6.3}$$

$$\mathrm{p} + \mathrm{n} \to \Delta^{0} + \mathrm{p} \begin{array}{l} \nearrow \mathrm{p} + \mathrm{p} + \pi^{-} \\ \searrow \mathrm{p} + \mathrm{n} + \pi^{0} \end{array} \tag{1.6.4}$$

The proton energy threshold required for pion production can be derived from the kinetics of proton scattering. When a solar flare occurs, the accelerated protons are inelastically diffused by the protons in the solar atmosphere, which is considered to be almost stationary. Let A be an accelerated proton and B be a proton at rest, and let T_{A} be the kinetic energy and p be the momentum of proton A in the system where proton B is at rest. The total kinetic energy of A and B in the center-of-mass system is T, and we consider the case of forward scattering. Letting the total energy be E, since $E^2 - p^2c^2$ is invariant under the Lorentz transformation, we have

$$(T_{\mathrm{A}} + 2m_{\mathrm{p}}c^2)^2 - p^2c^2 = (2T + m_{\mathrm{p}}c^2)^4 \tag{1.6.5}$$

where m_{p} is the mass of proton and c is the speed of light in the vacuum, respectively. On the other hand, T_{A} can be written as

$$T_{\mathrm{A}} = \sqrt{p^2c^2 + m_{\mathrm{p}}^2c^4} - m_{\mathrm{p}}c^2 \tag{1.6.6}$$

From Eqs. 1.6.5 and 1.6.6, we have

$$T_{\mathrm{A}} = 4T\left[1 + \frac{T}{2m_{\mathrm{p}}c^2}\right] \tag{1.6.7}$$

In a center-of-mass system, the sum of the momenta of proton A and proton B is zero, so the state in which both A and B are at rest after the collision satisfies the law of conservation of momentum. Therefore, the energy produced in this collision is $2T$. Considering that a particle of mass m is produced in this collision, the condition $2T \geq mc^2$ must be satisfied.

From Eq. 1.6.7, we can find the minimum value of T_{A} to be charged pions generated, which is

$$T_{\mathrm{A}} \geq 2m_{\pi}c^2\left[1 + \frac{m_{\pi}}{4m_{\mathrm{p}}}\right] \tag{1.6.8}$$

where m_{π} is invariant mass of pion. Substituting $m_{\mathrm{p}} = 938\mathrm{MeV/c^2}$ and $m_{\pi} = 139.5MeV/c^2$, we get the minimum kinetic energy of the proton required to produce a pion as

$$T_{\mathrm{th}} = 293\ \mathrm{MeV} \tag{1.6.9}$$

Therefore, the amount of proton with kinetic energy greater than T_{th} is important for estimating the amount of solar flare neutrinos.

There are mainly three predictions for solar flare neutrino flux at the Earth with different assumptions. Generation of solar flare neutrinos was simulated assuming the isotropic and beam-like proton acceleration with the Monte Carlo methods by Kocharov, Kovaltsov, and Usoskin [43], and Takeishi *et al.* [44]. For Fargion's and Moscato's prediction [42], the neutrino flux was estimated using the amount of energy taken up by pion production out of the total energy of solar flares.

Prediction of Kocharov, Kovaltsov, and Usoskin

They performed Monte Carlo simulations of particle production reactions in the solar atmosphere, and present the expected number of neutrino events for two cases. In the first model, protons that are isotropically accelerated are scattered by the solar atmosphere to produce pions, and a solar flare on the visible side of the sun is assumed. In the second model, protons are accelerated as beam-like and scattered with protons in the photosphere of the Sun to produce pions. It is corresponding to a solar flare on the invisible side of the Sun.

Prediction of Takeishi *et al.*

As in Kocharov, the proton energy spectrum is assumed to have a power spectrum and the number of protons contributing to neutrino production N_{p} (> 500 MeV) is estimated from the number of protons with the energy above 30MeV obtained from γ-ray observations. The calculation is done for two conditions: the case where the power index is 3 and the highest proton energy is 10 GeV, and the case where the power index is 1 and the highest proton energy is 100 GeV. The results are several orders of magnitude smaller than those from Fargion and Kocharov, and they indicate that it is difficult to observe solar flare neutrinos with the Super-Kamiokande detector.

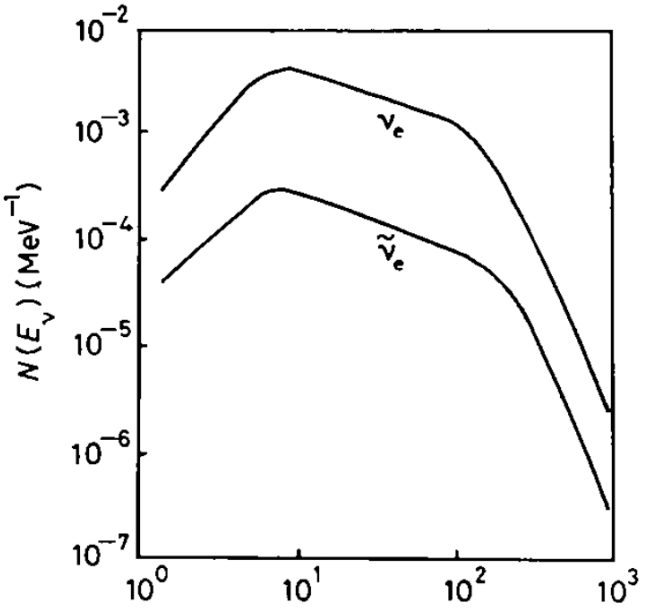

Figure 1.6: The prediction of Solar Flare neutrino flux by Kocharov [43]

Prediction by Fargion and Moscato

Fargion [42] calculated the neutrino energy spectrum by considering the energy conversion from the magnetic reconnection into proton accelerations. Assuming the conversion efficiency is 10%, Fargion estimated several neutrino interactions in the SK detector when solar flare classified as the largest explosion ($\geq 10^{32}$ erg) occurs at the invisible side of the Sun as listed in Table 1.3.

The ν generation conditions and numbers of the expected event in Super-Kamiokande (SK) are summarized in Table 1.3.

Table 1.3: Summary of the predicted solar flare models.

Model	Power index of parent proton	ν generation condition	The number of expected event in SK [/flare]
Kocharov, Kovaltsov, and Usoskin [43]	3 – 4	isotropic	1.36×10^{-4}
	1	beam like	0.85
Takeishi *et al.* [44]	3	isotropic	9.0×10^{-5}
	1	beam like	3.8×10^{-6}
Fargion and Moscato [42]	-	isotropic	0.75
	-	isotropic	7.5

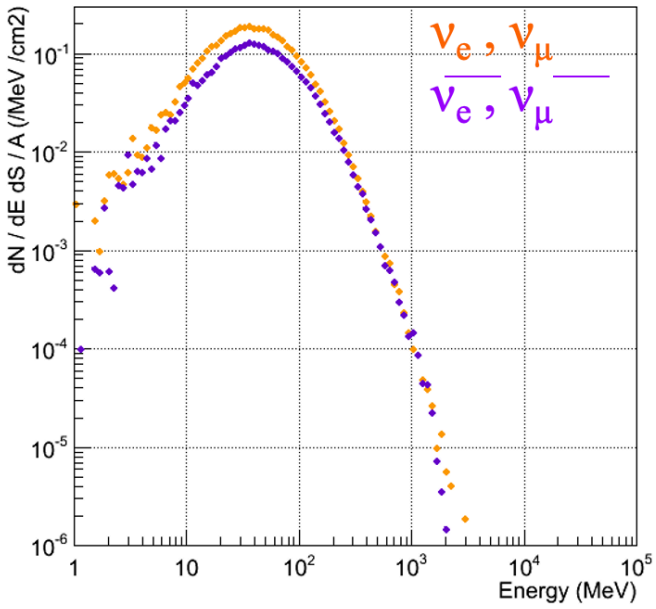

Figure 1.7: The prediction of Solar Flare neutrino flux by Takeishi *et al.* [44]

1.7 Current Situaion and Importance of Solar Flare Neutrino Detection

In 1988, the Homestake experiment reported an excess of neutrino events when energetic solar flares occurred. This observation suggested a relation between solar flares and the neutrino capture rate on ^{37}Cl [48, 49] and proposed neutrino magnetic moment spin precession to explain the time variation of the capture rate [50, 51]. However, the Kamiokande [52], SNO [53] and Borexino [54] experiments searched for neutrino signals using different solar flare samples and found no excess of signals related to solar flares.

Observations of solar flare neutrinos are important in the following two respects. The first is the investigation of the acceleration mechanism of hadrons in solar flares. If the neutrino energy spectrum can be measured, it will tell us the conditions of the accelerated protons, and this will provide new insights into the mechanism of ion acceleration in solar flares. The second is that neutrinos from solar flares on the invisible side of the Sun could be directly observed. In the case of a solar flare occurring on the invisible side of the Sun, the generated neutrinos penetrate through the Sun to reach the Earth. Therefore, if we can observe neutrinos originating from solar flares on the invisible side of the Sun, we may be able to obtain information on the acceleration mechanism toward the center of the Sun.

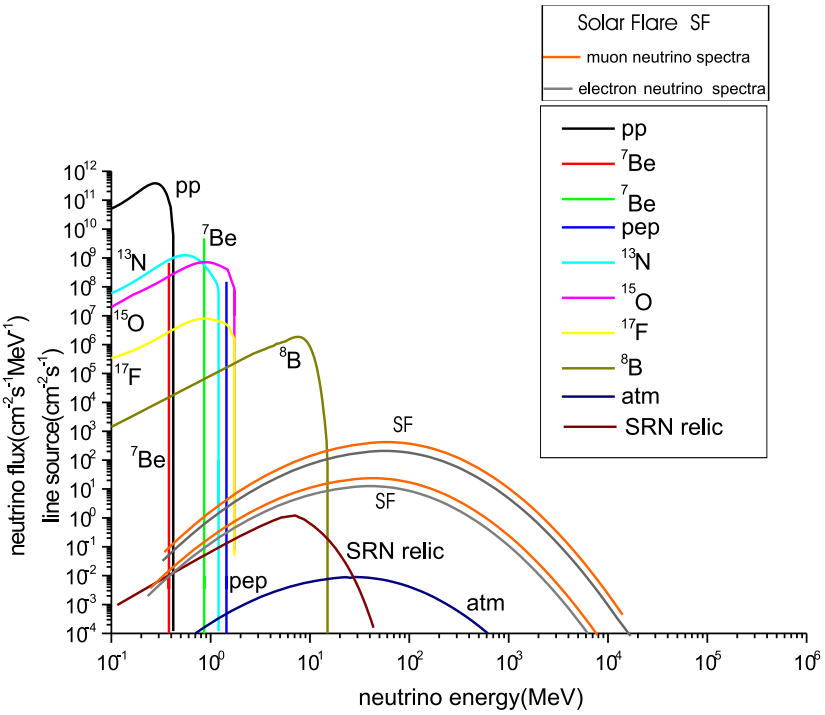

Figure 1.8: The prediction of solar flare neutrino flux by Fargion and Moscato [42]

Chapter 2

Super-Kamiokande Detector

In this chapter, the detection principle, the overview of the Super-Kamiokande detector, the water and air purification system and the data acquisition are described.

2.1 Cherenkov Radiation

The Cherenkov light is the light emitted when a charged particle passes through a dielectric medium with a speed faster than the speed of light in vacuum. It is in the form of a cone along the trail of a charged particle. The angle θ_c between the trajectory of the charged particle and the direction of the Cherenkov light is given as

$$\cos\theta_c = \frac{1}{\beta n} \tag{2.1.1}$$

where n is the refractive index of the dielectric medium and β is the velocity of the charged particle when the velocity of light in vacuum, c, is 1. In water, n is about 1.34, and the Cherenkov angle is about 42 degrees for a particle with $\beta \sim 1$.

Since a charged particle must have a velocity faster than the speed of light in the medium to emit the Cherenkov light, the velocity of the charged particle satisfies

$$\beta > \frac{1}{n}. \tag{2.1.2}$$

The lowest energy of the charged particle that satisfies this condition, which is called critical energy E_c, can be expressed as

$$E_c = \frac{nm_0}{\sqrt{n^2-1}}. \tag{2.1.3}$$

where m_0 is the mass of the charged particle. Table 2.1 shows the summary of critical energies for typical charged particles in water.

The Cherenkov light is detected as a ring pattern in SK, from which the point of occurrence of the event, the direction of travel of the charged particle, and the time of occurrence of the event can be reconstructed.

The number of emitted photons N depends on the wavelength of the emitted photon λ:

$$\frac{\mathrm{d}N}{\mathrm{d}x\mathrm{d}\lambda} = 2\pi\alpha\left(1-\frac{1}{n^2\beta^2}\right)\frac{1}{\lambda^2}, \tag{2.1.4}$$

Table 2.1: The list of critical energies of charged particles in water.

Charged Particle	Invariant Mass [MeV/c^2]	Critical Energy E_c [MeV]
$e^{\pm}$	0.511	0.767
$\mu^{\pm}$	105.7	157.4
$\pi^{\pm}$	139.7	207.9

where x stands for the path length of the particle, and $\alpha \sim 1/137$ is the fine structure constant. The number of emitted photons integrated from 300 to 600 nm with respect to λ (the sensitive wavelength region of SK PMTs) is about 340 photons/cm.

2.2 Overview of the Super-Kamiokande detector

The Super-Kamiokande (SK) detector is a 50 kton water Cherenkov detector located in Hida City, Gifu Prefecture, Japan [55]. It is located at 36°25′32.6″ N latitude and 137°18′37.1″ E longitude, about 370 m above sea level, approximately 1000 m under the Ikenoyama-mountain. The detector is a cylindrical water tank 39.3 m in diameter and 41.4 m high as shown in Figure 2.1. Because it is covered by a overburden about 1000 m thick, the event rate of muons from the atmosphere, which are the background of this analysis, are reduced to 1/100,000 compared to that at the ground level. About 11,000 photomultiplier tubes are installed on the inner surface of the detector to detect the Cherenkov light.

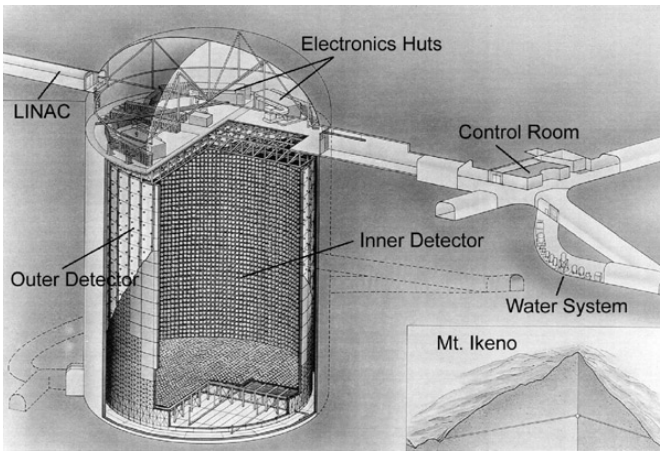

Figure 2.1: Schematic illustration of the Super-Kamiokande detector. Taken from [55].

2.3 PMTs for SK Detector

The SK detector structure is divided into an inner detector (ID) and an outer detector (OD), with a stainless steel frame called a supermodule between them. The inner detector has a diameter of 33.8 m and a height of 36.2 m. It can store about 32.5 kton of ultrapure water and is

equipped with 11129[1] 20-inch photomultiplier tubes facing inward. This 20-inch photomultiplier tube covers about 40% of the surface area of ID. The surfaces of ID other than the 20-inch photomultiplier tubes are covered with black sheets to optically separate it from OD and in order to prevent light leak from one side to the other. On the other hand, OD surrounds ID with a thickness of 2 m and is capable of storing about 17.5 kton of ultrapure water. 1885 8-inch photomultiplier tubes with a wavelength shifter plate of 60 cm wide and 60 cm high are mounted in the OD layer. The wall and supermodule sides of the OD layer are covered with a highly reflective Tyvek sheet in order to increase light collection efficiency in OD.

2.3.1 20-inch PMTs (ID PMTs)

The model number of the 20-inch photomultiplier tube (hereafter ID PMT or 20-inch PMT) used in the inner tank is Hamamatsu R3600 and has a spherical shape with a diameter of 20-inch (50 cm). Figure 2.2 shows a schematic diagram of the ID PMT. As shown in Fig. 2.3, the quantum efficiency is wavelength dependent, and it is 22% at 390 nm. The sensitive wavelength range is 280-660 nm. Figures 2.4 and 2.5 shows the pulse height distribution and the transit time distribution for one photoelectron. The performance is summarized in Table 2.2. From the 2nd phase of SK (i.e. from 2002), the ID PMTs are covered with fiber-reinforced plastic (FRP) and acrylic cases to prevent a chain reaction implosion.

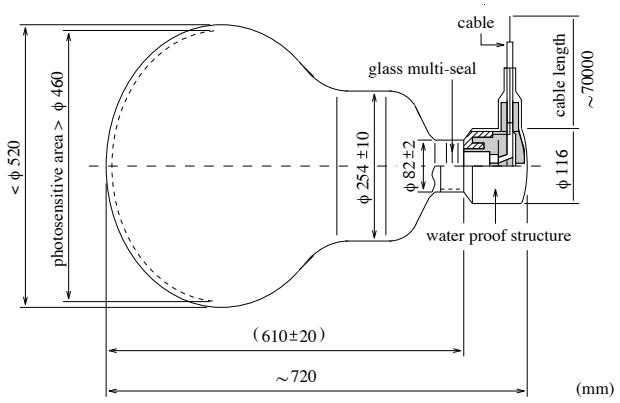

Figure 2.2: The schematic view of 20-inch PMT. Taken from [55].

2.3.2 Compensation Coils

Since the photoelectrons produced on the photocathode are collected by the electric field to the dynode, the geomagnetic field affects the collection efficiency of the photoelectrons. In order to reduce the effect of geomagnetic field in the detector, 26 sets of coils are wound around the tank to cancel out the geomagnetic field inside the tank. Thanks to the effect of these coils, the magnetic field in the tank is below 100 mG everywhere. Figure 2.6 shows a schematic view of the compensation coils of SK and Table 2.3 shows the currents which are flowing in the compensation coils.

[1]This is the number in the 3rd and 4th phases of SK. Those for the 1st and 2nd phases are 11146 and 5182, respectively. SK phases are explained in Sec. 2.4

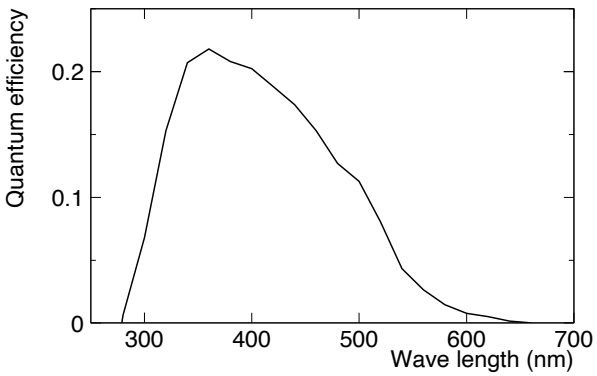

Figure 2.3: Quantum efficiency as a function of incident photon wavelength. Taken from [55].

Table 2.2: The summary of 20-inch PMT charactaristics [55].

Model number	Hamamatsu R3600
Material of photocathode	Bialkali (Sb-K-Cs)
Quantum Efficiency	22% at $\lambda \sim 390$ nm
Dynode type	Venetian blind type, 11 stages
Pressure tolerance	Pressure tolerance
Gain	10^7 at 2000 V
Dark current	200 nA at gain = 10^7
Dark noise rate	$\sim$ 3 kHz at gain = 10^7
Transit time	90 nsec typical at gain = 10^7
Transit time spread	2.2 nsec at single photoelectron

2.4 SK Phases

Since the start of observations in April 1996, Super-Kamiokande has been divided into six data acquisition phases. Table 2.4 summarizes the performance of the Super-Kamiokande detectors in each phase.

SK-I

The data of SK-I was collected from April 1996 to July 2001. In July 2001, the faulty PMTs were replaced. Later, while pouring ultrapure water into the detector, a PMT at the bottom ruptured, causing other PMTs to rupture in a chain reaction. As a result of this accident, 6777 of the PMTs in the inner detector and 1100 of the PMTs in the outer detector were lost.

SK-II

After the accidental breakage of the PMTs, the number of PMTs in the inner tank was decreased to 5182, and the data were taken from October 2002. The ID PMTs were equipped with shock wave protection cases.

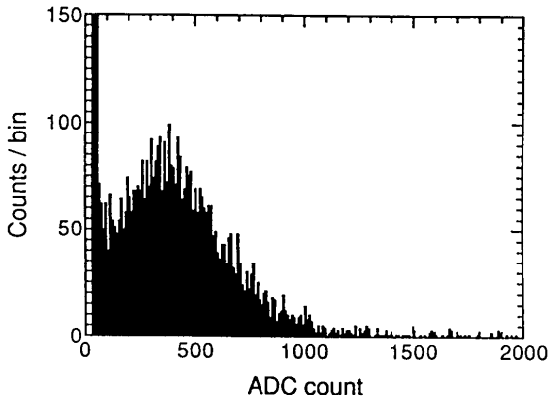

Figure 2.4: Single photoelectron distribution of the ID PMT. Taken from [55].

Table 2.3: The Current flowing in the compensation coils [56].

Coils in Fig. 2.6	A	B	C	D	E	F	G
Current [A]	31.35	31.35	31.35	28.80	30.10	28.60	30.10

SK-III

New PMTs were installed to replace the ones lost due to the PMT breakage accident. As a result of this work, the number of PMTs in the inner tank was 11129 and the coverage rate was 40% again.

SK-IV

In August 2008, the electronics for data acquisition were redesigned, and a new set of electronics called QBEE was introduced in SK-IV, replacing the ATM used in SK-I, SK-II, and SK-III.

SK-V

After refurbishing the tank for "Super Kamiokande Gadolinium" (SK-Gd), the observation was resumed using ultrapure water.

SK-VI (SK-Gd)

Gadolinium with a concentration of 0.01% was added to improve the detection efficiency of neutrons in July 2020.

2.5 Water and Air Purification System

The ultrapure water used in the Super-Kamiokande detector is purified from groundwater in the Kamioka mine. The groundwater contains many impurities. The impurities absorb and scatter

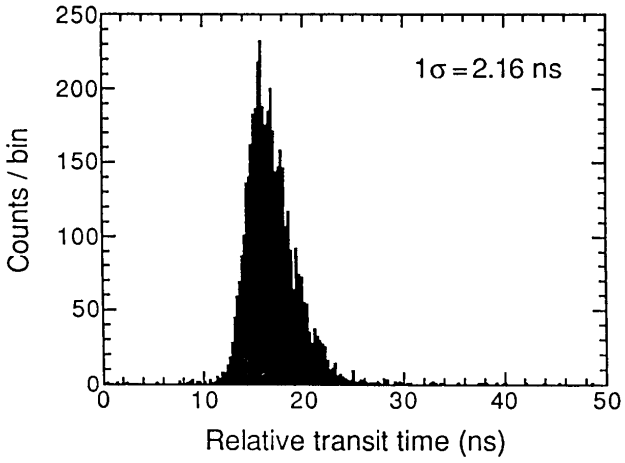

Figure 2.5: Transit time distribution of the ID PMT. Taken from [55].

Table 2.4: The summary of SK phases.

SK Phase	SK-I	SK-II	SK-III	SK-IV	SK-V	SK-VI
Start Date	Apr. 1996	Oct. 2002	Jul. 2006	Sep. 2008	Jan. 2019	Jul. 2020
Stop Date	Jul. 2001	Oct. 2005	Aug. 2008	May 2018	Jul. 2020	Running
Number of ID PMT	11146	5182	11129	11129	11129	11129
Gadolinium dope	×	×	×	×	×	○
PMT Acrylic case	×	○	○	○	○	○
Electronics	ATM	ATM	ATM	QBEE	QBEE	QBEE

light and reduce light transmission, as well as radioactive impurities create background events in neutrino observation. So, it is necessary to remove them. In addition to this, the bedrock contains many radioactive elements, and the air inside the mine, for example, has a concentration of radon more than 100 times higher than the air on the ground. In the Super-Kamiokande experiment, the air outside the mine is purified and blown to the experimental area which includes dome of the SK detector, water system area and etc.

2.5.1 Water Purification System

The ultrapure water production system as shown in Fig. 2.7 in SK. A different system has been used for gadolinium dissolution in 2020, but the details are omitted because the data in ultrapure water were used in this study. The following is a brief description of the ultrapure water production process.

- 1μm filter – Removes dust particles larger than 1 μm in size.
- Heat exchanger – The water pump used for circulation and the photomultiplier tubes emit heat. This heat causes the water temperature to rise, which increases

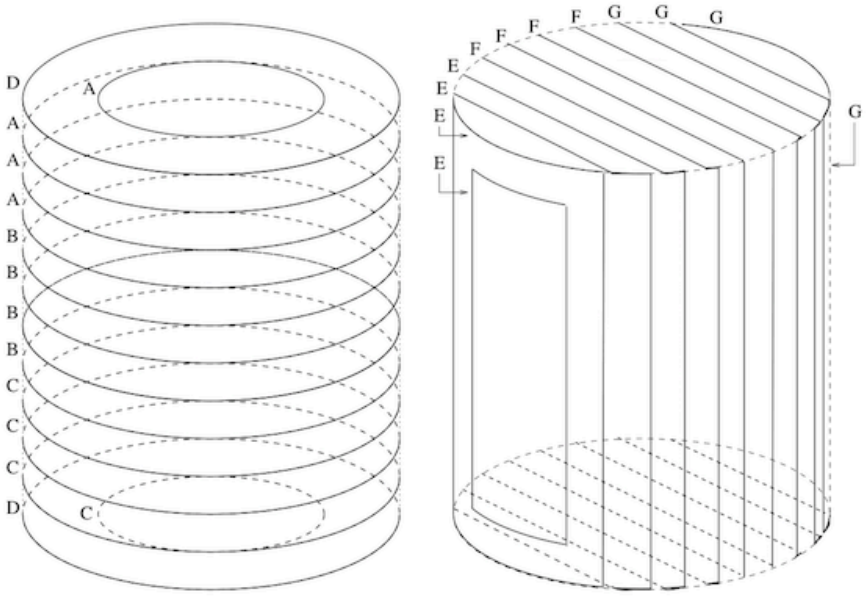

Figure 2.6: A schematic view of the compensation coils of SK. Taken from [56].

the dark noise and causes convection inside the tank. To prevent the rise in the water temperature, the temperature of the supply water is adjusted to be about 13 degrees Celsius.

- Ion exchanger – Removes metal ions dissolved in the water.
- UV sterilizer – Irradiates with ultraviolet light to kill bacteria that breed in the water.
- Rn-free-air dissolving system – In order to improve the removal efficiency of radon gas in the vacuum degassing process, the air with the radon removed as much as possible is dissolved in pure water.
- Reverse osmosis filter – Perform filtration using osmotic pressure to remove organic compounds with a molecular weight of about 100.
- Vacuum degasifier – Removes gases dissolved in water.
- Cardridge Ion Exchanger – Cartridge ion exchanger further reduces ions in the water.
- Ultra Filter – Removes small dust particles larger than 10 nm in size.
- Membrane Degasifier – Removes gases dissolved in the water.

2.5.2 Air Purification System

Figure 2.8 shows the outline of the air purification system. The process of air purification is shown below.

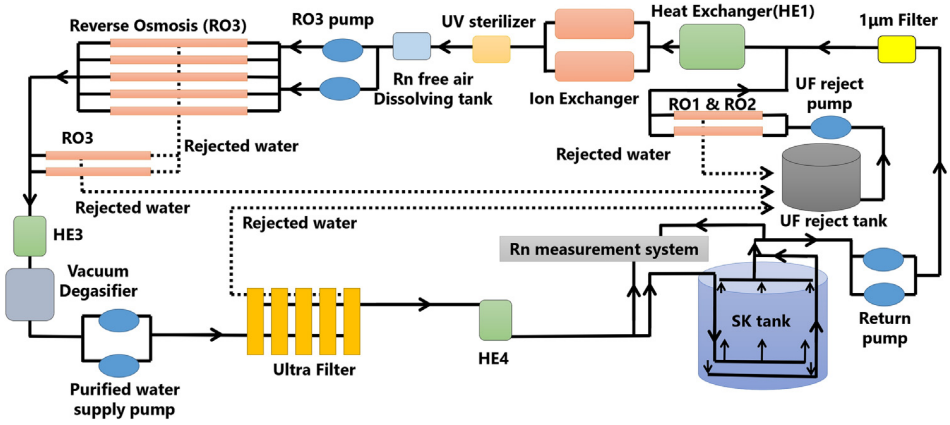

Figure 2.7: Water purification system of the Super-Kamiokande detector. Taken from [57].

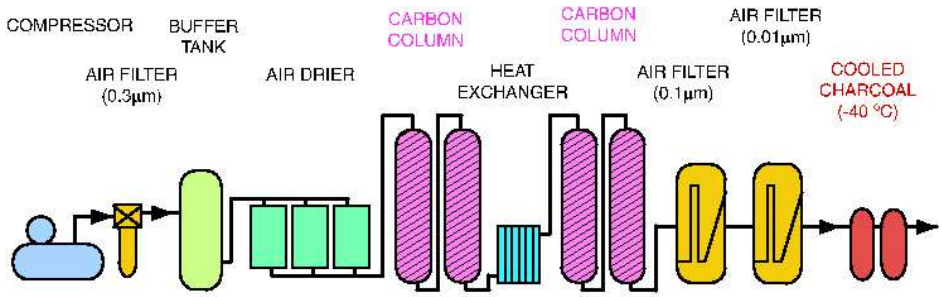

Figure 2.8: Air purification system of the Super-Kamiokande detector. Taken from [55].

- Compressor – Compresses the air to 7-8.5 atm.
- Filter – Dust is removed from the air. There are three types of filters: 0.3 μm, 0.1 μm, and 0.01 μm.
- Dehumidification, CO_2 removal system – Removes H_2O and CO_2 contained in the air.
- Activated charcoal – By passing air through the activated carbon, radon contained in the air is adsorbed.
- Cooled activated charcoal – To increase radon removal efficiency, radon is adsorbed by activated carbon cooled to -40 degrees Celesius.

2.6 Data Acquisition and Electronics

From the start of SK observations until August 2008, an electronic circuit called Analog-Timing-Modules (ATM) was used for data acquisition. In September 2008, a new electronic circuit called QTC-Based Electronics Ethernet (QBEE) and software trigger system were introduced. In this section, these two types of DAQ system are described.

2.6.1 DAQ system of SK-I to SK-III

DAQ system for Inner Detector

Figures 2.9 and 2.10 show a schematic view of analog input blocks of ATM and the DAQ system of SK-I to SK-III. The ATM combines the functions of an analog-to-digital converter (ADC) and a time-to-digital converter (TDC) to record the integrated charge and arrival time of each PMT signal. 12 PMT signals are fed to a ATM board. The PMT signal in current splitter is divided into four signals.

When one of the PMT signal is sent to the ATM channel and its amplitude is greater than -1 mV (0.25 photoelectron), the ATM channel converts the amplitude and detection time of the signal into an analog charge and holds it. At the same time, the ATM board sends an analog signal whose amplitude is proportional to the number of hit channels (HITSUM signal) to the trigger module. All HITSUM signals are summed up, and if the total amplitude exceeds a threshold, a global trigger is issued. When a global trigger is generated, all ATMs digitize the charge and time information which is held in the previous step. The digital signals are sent to and stored at SMP (Super Module Partner). These data are sent to the online computers, finally.

DAQ system for Outer Detector

A schematic diagram of the OD data acquisition system for SK-I to -III is shown in Fig. 2.11. A single coaxial cable feeds high voltage to each PMT and carries back its analog signals. Each channel is connected to a custom “paddle card” which fans out the voltage to 12 PMTs. These cards also pick off the analog PMT signals through a high voltage capacitor and resistor network, allowing a single cable to be used for both HV and signal.

A signal from one OD PMT is sent to a charge-to-timing converter (QTC) module, which converts it to a rectangular pulse whose width is proportional to the input charge. Similarly to ID, a HITSUM signal is generated at the QTC module and sent to the trigger module. If a global trigger is issued, the leading edge and the width of the pulse is converted to the timing and charge information of the OD PMT by the TDC module.

Hardware Trigger

There are three types of global triggers for ID and one type for OD. The SLE trigger rate is most sensitive to the detector ambient background level, for example, γ-rays from rock, β-rays from ^{214}Bi and so on. Therefore, the SLE trigger threshold value was changed many times. They have different threshold voltage values, and their values are summarized in Table 2.5.

2.6.2 DAQ system for SK-IV

Figures 2.12 and 2.13 shows the block diagram of the QTC and its surroundings and the data acquisition system of SK-IV. One QBEE module has eight QTCs (Charge to Time Converters), and each QTC handles the signals of three PMTs. When a signal is sent to a QBEE channel,

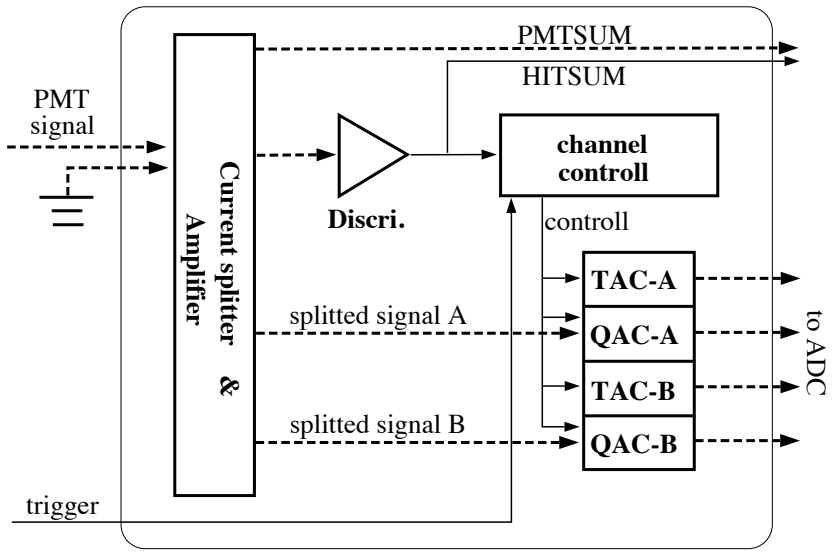

Figure 2.9: A schematic view of the analog input blocks of the ATM. Only one channel is shown in the figure. Dashed arrows show the PMT signal, its split signals, and accumulated time and charge signals. Solid arrows show the logic signals which control the processing of the analog signals. Taken from [55].

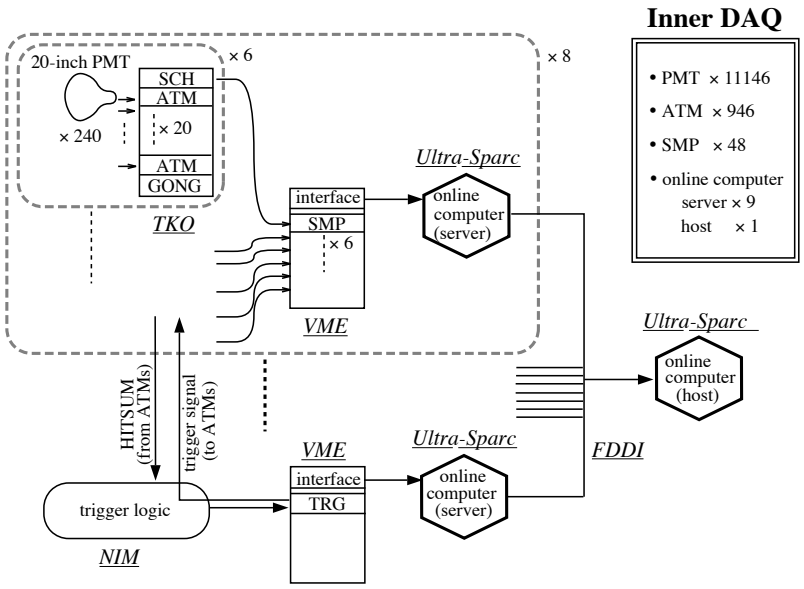

Figure 2.10: The schematic view of the DAQ system for the SK-I to SK-III inner detector. Arrows show data flow. Taken from [55].

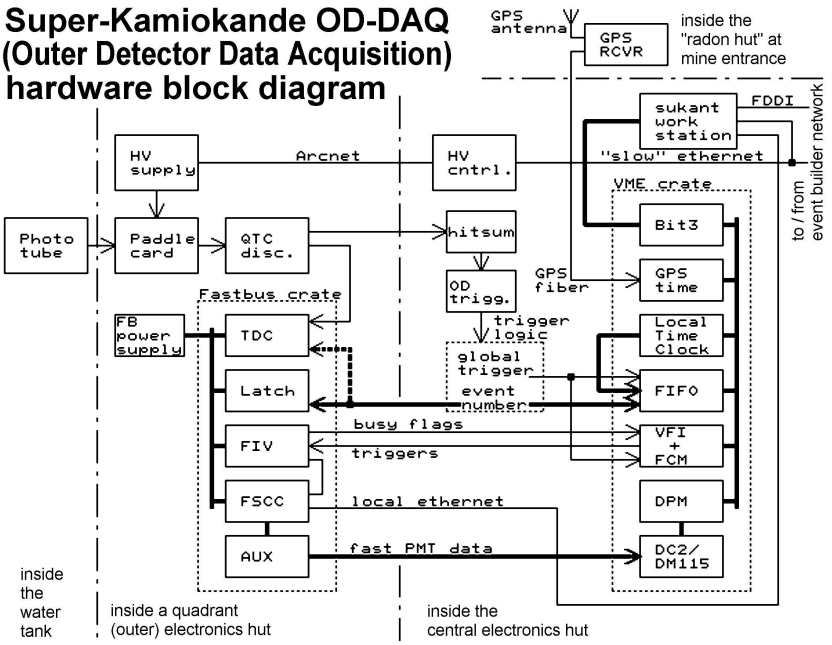

Figure 2.11: The schematic view of DAQ system for SK-I to SK-III outer detector. Taken from [55].

Table 2.5: The summary of Hardware Trigger threshold in SK-I to SK-III. About -11 mV corresponds to one PMT hit.

SK Phase	SK-I	SK-II	SK-III
HE	-340 mV	-180 mV	-320 mV
LE	-320 mV	-152 mV	-302 mV
SLE	$-260 \rightarrow -180$ mV	-110 mV	$-212 \rightarrow -186$ mV
OD	-380 mV	-380 mV	-380 mV

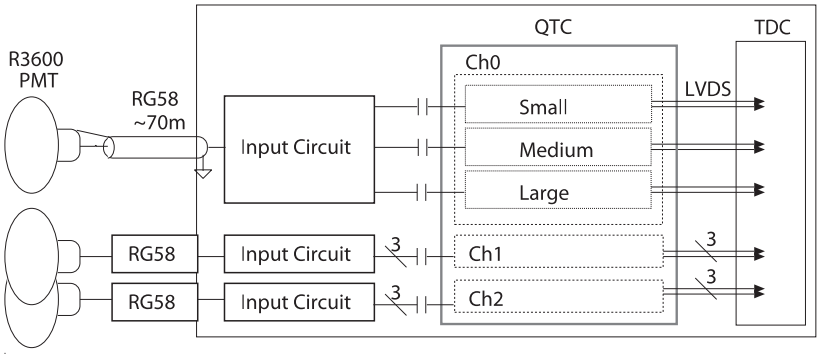

Figure 2.12: Block diagram of the QTC and its surroundings. PMT signals, transmitted through coaxial cables, are divided into three QTC gain ranges. Combined with the input circuits, the QTC provides full analog signal processing for the PMT signals. Output signals are generated by LVDS drivers and read by TDCs. Taken from [58].

Table 2.6: Observable charge range for each of the three input channels of QBEE. Taken from [58].

Channel	Observable range [pC]	Charge resolution [pC/count]
Small	0–51	0.1
Medium	0–357	0.7
High	0–2500	4.9

and its amplitude exceeds the threshold, 1/4 photoelectrons, the QTC module integrates the signal and outputs a rectangular pulse, whose leading-edge represents the signal timing and width represents the integrated charge. The rectangular pulse is sent to the TDC module and digitized. The digitized charge and timing information is sent to the front-end PC through the Ethernet cable after being processed by FPGA (Field Programmable Gate Array). The front-end PCs arrange the received data in a timing order and send them to the merger PCs, where a software trigger is issued.

In order to improve the charge resolution at a few p.e. levels and to handle a wider range of charges than ATM, QTC has three gain range channels (Small, Medium, and High). Table 2.6 shows the observable charge range and resolution. Overall, the charge range is 0.2 pC to 2500 pC.

Software Trigger

In the merger PC, the software triggering is performed by looking for events where the number of PMTs hit within 200 nsec, N_{200}, exceeds a certain threshold. Table 2.7 summarizes the trigger types, N_{200} thresholds, and typical event rates. The time width for an event with LE or HE trigger is 40 μsec. In the case of the SLE trigger, the event time width is set to 1.3 μsec to reduce the amount of data. The SHE (Super High Energy) and AFT (AFTer) triggers were added for the study of supernova relic neutrinos. The SHE trigger is triggered when N_{200} exceeds 70, and the AFT trigger is issued only if the OD trigger is not issued and the SHE trigger is issued. When the AFT trigger is issued, data are acquired without setting a trigger threshold for 500

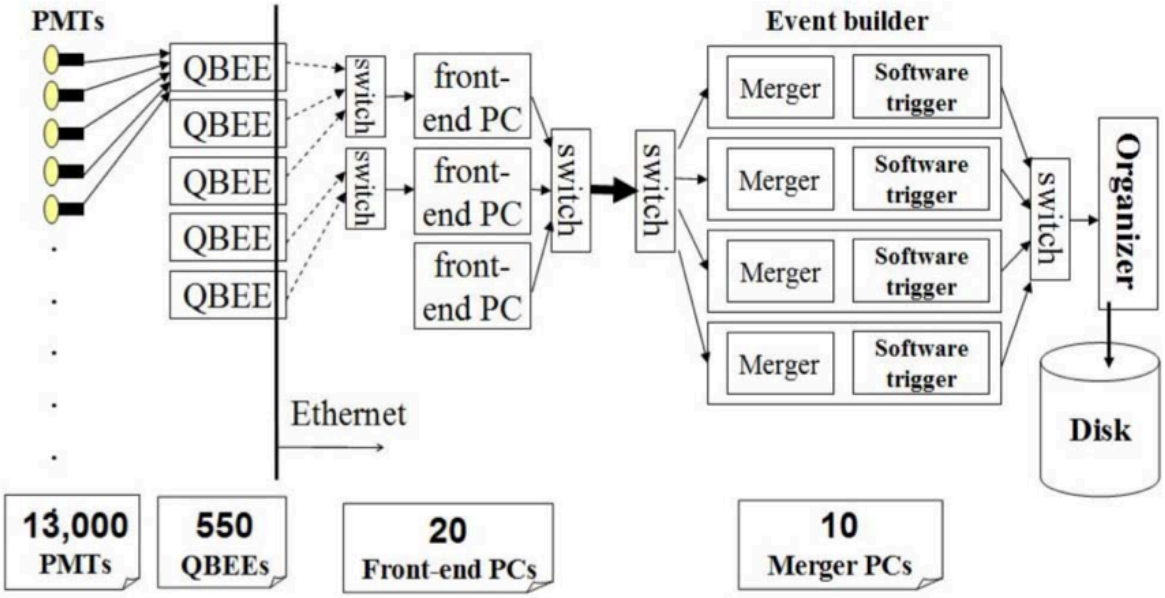

Figure 2.13: Schematic view of the data acquisition system of SK-IV. In the left part, newly developed front-end electronics boards connected with PMTs are shown. In the right part, components of the new online system are shown. The data are transferred from QBEEs to the organizer PC via 100 Base-T (broken line), Gigabit Ethernet (solid line) or 10-Gigabit Ethernet (bold solid line). Taken from [59].

Table 2.7: The summary of software trigger in SK-IV.

Trigger type	N_{200} threshold [hit]	Recorded event time width [μsec]	Event rate [Hz]
SLE	34	1.3	$\sim$3500
LE	47	40	$\sim$40
HE	50	40	$\sim$ 10
SHE (before Sep. 2011)	70	40	-
SHE (after Sep. 2011)	58	40	-

μsec after the event.

The SHE and AFT triggers can detect 2.2 MeV γ-rays emitted when neutrons are captured by hydrogen nuclei. The hit threshold of the SHE trigger was lowered from 70 to 58 in September 2011.

Chapter 3

Search Time Window Determination

This chapter describes the importance of determining the time window and how it was done in this thesis.

3.1 The Importance of Determining Search Time Window

The GOES satellite provides data relating only to the intensity of soft X-rays produced by thermal electrons. Hence, the GOES data may not be particularly useful for identifying the time window for the search for solar flare neutrinos because neutrinos originate from interactions of protons.

In the previous study, Wasseige [60] proposed a method for determining the search window for solar flare neutrinos using γ-rays above 70 MeV for neutral pion decays ($\pi^0 \rightarrow 2\gamma$) observed by the Fermi-LAT satellite. The appearance of neutral pions implies the production of neutrinos in solar flares because charged pions are expected to be produced simultaneously with neutral pions. Therefore, it is natural to set the search window for solar flare neutrinos based on the occurrence time frame of γ-ray emission caused by neutral pions. However, as the Fermi-LAT satellite data is available only after its launch in 2008, this method cannot be applied to the solar flares before that time, notably to the largest solar flare on record November 04, 2003, class X28.0 [61]. For those reasons, an alternative method must have been developed to determine the time window for the flare neutrino search.

Neupert [24] pointed out an empirical correlation between the soft X-ray flux and the integral of the microwave flux during solar flares (hereafter Neupert effect). In many flares, the behavior of the time derivative for the soft X-ray intensity is similar to a temporal variation of the radio, hard X-ray and γ-ray flux during the impulsive phase. Although the statistics are low, Veronig et al. [62] examined the moment of appearance for the γ-ray including that from π^0 in large flare and found the time coincidence with the moment of main energy release determined by hard X-rays and line γ-rays. Kurt et al. [63] systematically analyzed the γ-rays from π^0 decays and neutron emissions recorded by the SONG (*SOlar Neutrons and Gamma rays detector*) detector [64] and compared their time profiles with those of soft X-ray by GOES and ULYSSES [65], hard X-ray by Yohkoh [66] and RHESSI [67], line γ-ray by INTEGRAL (*INTErnational Gamma-Ray Astrophysics Laboratory*) [68]. The temporal relation among the γ-ray emission from π^0 decay, the derivative of soft X-ray and hard X-ray is shown in Fig. 3.1. Therefore, we used the time

Table 3.1: Observation targets for each solar satellite. Circles (◯) show the main target whose energy and timing can be measured by the satellite's devices. Triangles (△) indicate secondary target, hardly detectable by the satellite as direct measurements; the counting rate alone can indirectly imply target existence. Details are described in the later sections.

Satellite	Launch year	End year	Soft X-ray	Hard X-ray	Line γ-ray	γ-ray
GOES	1975	–	◯	△	–	–
RHESSI	2002	2018	◯	◯	◯	◯
GEOTAIL	1992	–	–	△	△	△

Table 3.2: Summary of satellites and energy ranges in this study. As described in the main text, GEOTAIL cannot measure the energy of neutral particles above 50 keV.

Type	Satellite	Energy range (wave length)
Soft X-ray	GOES	1.5–12 keV (1–8 Å)
Hard X-ray	RHESSI	100–800 keV
Line γ-ray	RHESSI	2.218–2.228 MeV
Hard X-ray and soft γ-ray	GEOTAIL	Above 50 keV

profile of the time derivative for the soft X-ray instead of the γ-ray emission from π^0 decay to determine search time windows.

3.2 The Visible Side Solar Flares

The flares on the visible side are observed by various satellites, which provide data in a wide range of wavelengths. To search for solar flare neutrinos, we used public data from solar satellites and computational resources of the Center for Integrated Data Science (CIDAS) at Nagoya University. In this study, we analyzed the data recorded by three satellites; GOES, RHESSI, and GEOTAIL. The main targets of each satellite are summarized in Table 3.1.

Using CIDAS, we analyzed the GOES satellite's soft X-ray data, as well as the RHESSI satellite's hard X-ray and γ-ray data, as summarized in Table 3.2. For the analysis of GEOTAIL data, we used the raw data to recover hard X-rays above 50 keV including soft γ-rays.

3.2.1 Solar Flare Event Selection

We used data obtained by the GOES satellite to select solar flares for our neutrino search because the GOES satellite series have continually monitored solar flares since 1975. Its long operation permits the use of the same indicator in comparisons between older and more recent flares.

For this study, we first registered all solar flares occurring from 1996 to 2018 in the NOAA list. Then, we selected the 23 solar flares whose peak soft X-ray intensity exceeds 5.0×10^{-4} W/m^2 (X5.0 class). The date, class, and location on the Sun (active region, so-called AR) for each selected flare are summarized in Table 3.3.

Table 3.3: List of solar flares selected for this study. The data, class and active region (AR) location are taken from a National Oceanic and Atmospheric Administration source (NOAA, https://www.ngdc.noaa.gov/stp/space-weather/solar-data/solar-features/solar-flares/x-rays/goes/xrs/).

Date	Class	AR location
1997 Nov. 6	X9.5	S18W63
2000 Jul. 14	X5.7	N22W07
2001 Apr. 2	X20.0	S21E83
2001 Apr. 6	X5.6	S21E31
2001 Apr. 15	X14.4	S20W85
2001 Aug. 25	X5.8	S17E34
2001 Dec. 13	X5.3	N16E09
2002 Jul. 23	X5.1	S13E72
2003 Oct. 23	X5.4	S21E88
2003 Oct. 28	X17.2	S16E08
2003 Oct. 29	X10.0	S15W02
2003 Nov. 2	X9.2	S14W56
2003 Nov. 4	X28.0	S19W83
2005 Jan. 20	X7.1	N14W61
2005 Sep. 7	X18.2	S11E77
2005 Sep. 8	X5.4	S12E75
2005 Sep. 9	X6.2	S12E67
2006 Dec. 5	X9.0	S07E68
2006 Dec. 6	X6.5	S05E64
2011 Aug. 9	X7.4	N14W69
2012 Mar. 7	X5.4	N22E12
2017 Sep. 6	X9.4	S09W34
2017 Sep. 10	X8.3	S08W88

3.2.2 Time Window Determination

Soft X-rays (GOES)

A typical soft X-ray light curve observed by the GOES satellite is shown in the top panel of Fig. 3.2. In the NOAA list, the timing at which four consecutive flux increases occur was determined as the start time of each solar flare. The flare end time was typically determined as the timing at which the event's flux decline to half the value of its peak. However, this end time depends on the flare class which makes unsuitable for our analysis. We, therefore, set the flare end time as the timing at which the flux declines to 1.0×10^{-4} W/m^2 (X1.0 class).

To extract information about light curve brightening correlated with particle acceleration, we took a calculation of the time derivative of the light curve as shown in the bottom panel of Fig. 3.2. For setting the time window, we first fitted the light curve with a Gauss function ($A \exp\{(t - t_{\rm peak})^2/\sigma^2\}$). We then selected the region of $[t_{\rm peak} - 3\sigma,\ t_{\rm peak} + 3\sigma]$ as the search window.

Hard X-ray (RHESSI)

The RHESSI satellite was launched in February 2002 to monitor solar flares. It records electromagnetic waves in the range of 3 keV to 17 MeV and can observe continuous spectra from bremsstrahlung of high energy electrons, line γ-rays of 2.223 MeV, and γ-rays from ^{12}C and ^{16}O nuclei [67]. Owing to its wide energy range, the RHESSI satellite provides important information for extracting acceleration time scales for electrons, protons, and ions.

In this study, we scanned the energy spectrum in the range of 100–800 keV for hard X-ray analysis as shown in the top panel of Fig. 3.3 (a). We then determined the count rate within this energy range using the front detector on the RHESSI. To set the search window, we fitted the light curve via a combination of basic functions. For the fitting, we used a constant value for the background before the brightening, a linear function for the brightening phase of the light curve, and an exponential function for the dimming phase. The start time ($t_{\rm start}$) was defined as the time when the liner function intercepts the background constant. The time window was determined by selecting the region where the exponential function is 2σ beyond the background constant. The end time ($t_{\rm end}$) is the last point satisfying this condition. In this way, the search window by hard X-ray is determined as $[t_{\rm start},\ t_{\rm end}]$.

Line γ-rays (RHESSI)

For line γ-ray analysis, we first scanned the energy spectrum before and after each solar flare as shown in the top panel of Fig. 3.3 (a). Here we defined the energy spectrum before (after) as OFF (ON) FLARE. Then, we took a ratio between them as shown in the bottom panel of Fig. 3.3 (a). When we confirmed the line γ-ray in the spectrum after the solar flare, we plotted the light curve using the energy range of 2.218–2.228 MeV as shown in Fig. 3.3 (b). To determine the search window, we used the same method described above for hard X-rays. It is reported in Ref. [70] that line γ-ray signal of neutron capture is delayed by 100 sec because it takes some time for the neutron to be thermalized and captured by hydrogen in the solar atmosphere. Therefore, we selected the region of $[t_{\rm start} - 100\ {\rm sec},\ t_{\rm end}]$ as the time window for line γ-rays.

GEOTAIL satellite hard X-ray events

The GEOTAIL satellite was launched in July 1992 to observe the Earth's magnetosphere. Its main targets are electrical field, magnetic field, plasma, and high energy particles in the magnetosphere. The LEP (low energy particle) instrument mounted on the satellite, can measure counts of ions and electrons independently based on energy-per-charge separation [71]. The LEP

detector consists of an electrostatic analyzer and particle counters: microchannel plates for ions, and channel electron multipliers for electrons.

GEOTAIL has occasionally been exposed to the intense fluxes of energetic ions >50 MeV and photons of >50 keV after strong solar flares or giant flares of magnetars [72–74]. These energetic ions and photons do not follow the electrostatic analyzer's energy-per-charge regulation, but rather penetrate through the satellite wall and hit the particle counters directly. For the solar flare case, energetic photons include hard X-ray photons from bremsstrahlung by high energy electrons, as well as line γ-ray photons from nuclear interactions. Figure 3.4 shows an example of this situation. During the interval 10:35:00–11:35:00 UTC on October 28, 2003, GEOTAIL was in the solar wind upstream of the Earth's bow shock and continued to measure solar wind particles as well as nonthermal ions (10–40 keV/q) accelerated by the bow shock. However, during the interval 11:01:40–11:15:30 UTC, GEOTAIL was hit by the solar flare hard X-ray photons, which produced the energy-independent stripes in the first to third panel of Fig. 3.4. It is noted that tailward-flowing solar wind ions (less than ∼20 keV/q colored with yellow-red-black) overwrapped with the hard X-ray stripes as shown in the fourth panel of Fig. 3.4. The penetration depth for hard X-ray photons from the satellite wall to the counter depends on the satellite spin phase so that the colors of the energy-independent stripes differ slightly sector by sector. The electron detector (not shown) responded to the solar flare hard X-ray photons similarly. However, because the form factor of the electron detectors is two orders of magnitude smaller than that of the ion detectors, the apparent contribution of solar flare hard X-ray photons is much weaker.

In the present study, we estimated the time profiles of particle acceleration by selecting data from the four sectors and the energy range that was not "contaminated" by ions, taking count averages every 12 s. Figure 3.5 shows the photon counts from 10:50:00 to 11:20:00 UTC, as calculated from the data in the dawnward, sunward, and duskward sectors in Fig. 3.4. Finally, the time window for GEOTAIL is determined using the same method as that used in the analysis for line γ-ray above, because a component of the GEOTAIL signal contains line γ-rays.

Because all satellite data are available for the solar flare occurring on November 2, 2003, we used this example to illustrate the method for the time window determination developed in this study, shown in Fig. 3.6.

The analysis results for 23 solar flares selected in this study are summarized in Tables 3.4 and 3.5. It is noted that, we failed to obtain the time window determined by the derivative of soft X-ray for the solar flare occurring on September 9, 2005, because the brightening of its soft X-ray light curve was relatively slow and the derivative of soft X-ray was not large enough. Figure 3.7 summarizes the distribution of timing window duration for each channel. On the basis of these results, the average time duration for each channel is as follows;

- Soft X-ray: $4,178$ s
- Derivative of soft X-rays: 700 s
- Hard X-rays: 944 s
- Line γ-rays from neutron capture: $1,586$ s
- Hard X-rays (GEOTAIL): 776 s

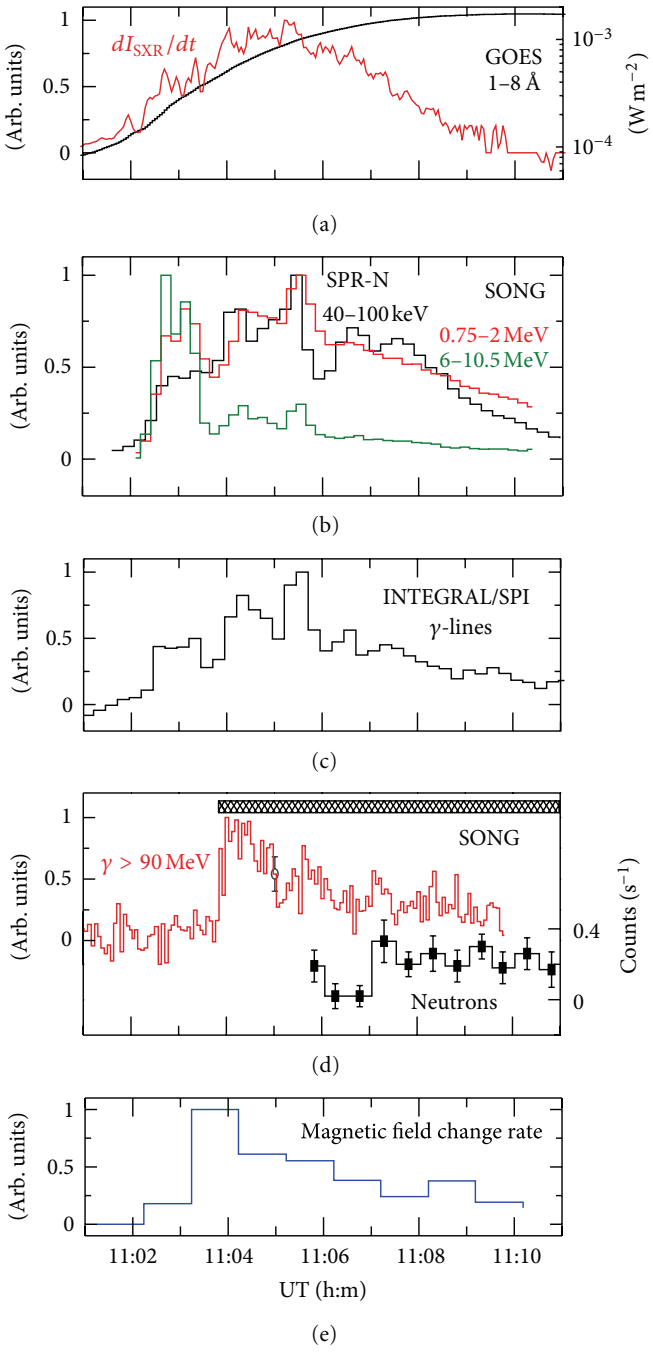

Figure 3.1: Normalized time profiles of selected emissions from the solar flare occurring on October 28, 2003.(a) soft X-ray flux and its derivative from GOES; (b) hard X-ray 40-100 keV from CORONAS-F/SPR-N (black curve); gamma-rays from SONG 0.75-2 MeV (red) and 6-10.5 MeV (green); (c) line γ-rays from INTEGRAL/SPI; (d) γ-rays > 90 MeV (red, left y-axis) and neutrons (black, right y-axis) from SONG. (e) magnetic field change rate [69]. Taken from [63].

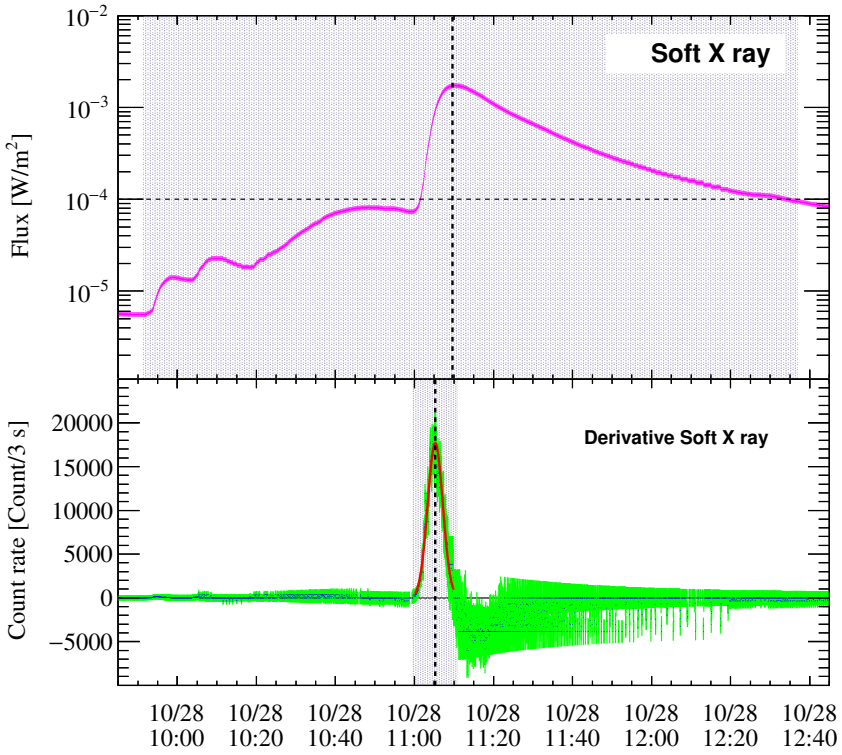

Figure 3.2: An example solar flare occurring on October 28, 2003, showing the soft X-ray light curve (top) observed by the GOES satellite and the derivative of the flux of soft X-rays (bottom). In the top panel, the horizontal axis is universal time and the vertical axis is the flux of soft X-rays. The black dotted horizontal line indicates a flux of 1.0×10^{-4} W/m^2. The region drawn in gray shows the time window selected in this study. In the bottom panel, the horizontal axis is universal time and the vertical axis is the derivative of the flux of soft X-rays with respect to time. The blue dots and the green region depict the data and their error, respectively; the red curve is the result of Gaussian fitting. The gray region shows the time window selected by this study.

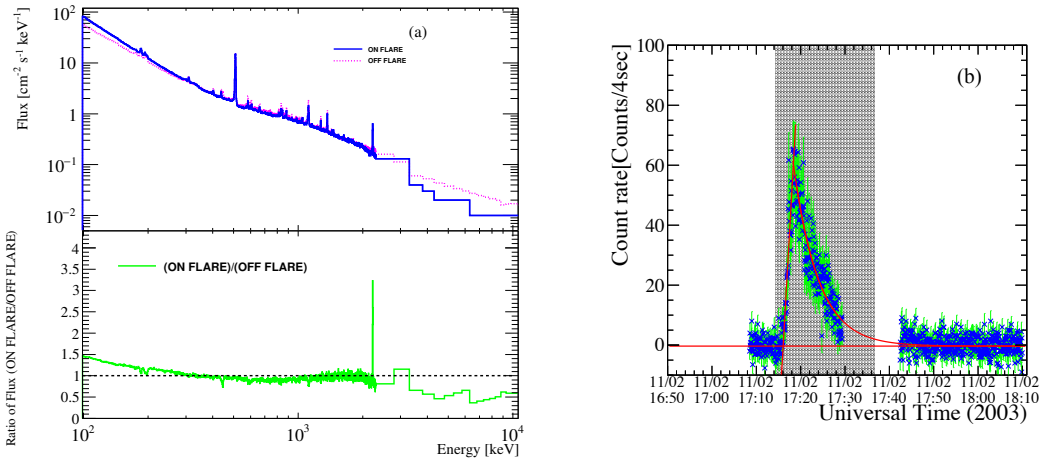

Figure 3.3: (a) Energy spectra of γ-rays associated with the solar flare occurring on November 2, 2003, as recorded by the RHESSI satellite. The blue solid histograms show ON FLARE and the pink dashed histograms represent OFF FLARE. The horizontal axis shows energy in keV and the vertical axis in the top panel shows the flux of γ-rays in units of $\mathrm{cm}^{-2}\mathrm{sec}^{-1}\mathrm{keV}^{-1}$ The vertical axis in the bottom panel shows the ratio between fluxes in dimensionless units. (b) Light curve of the solar flare as shown in (a). The horizontal axis shows universal time and the vertical axis shows the count rate in units of count per 4 s. The blue points and green bars depict the data and their error, respectively. The red curves show the fitting results and the shaded region shows the time window determined by this method.

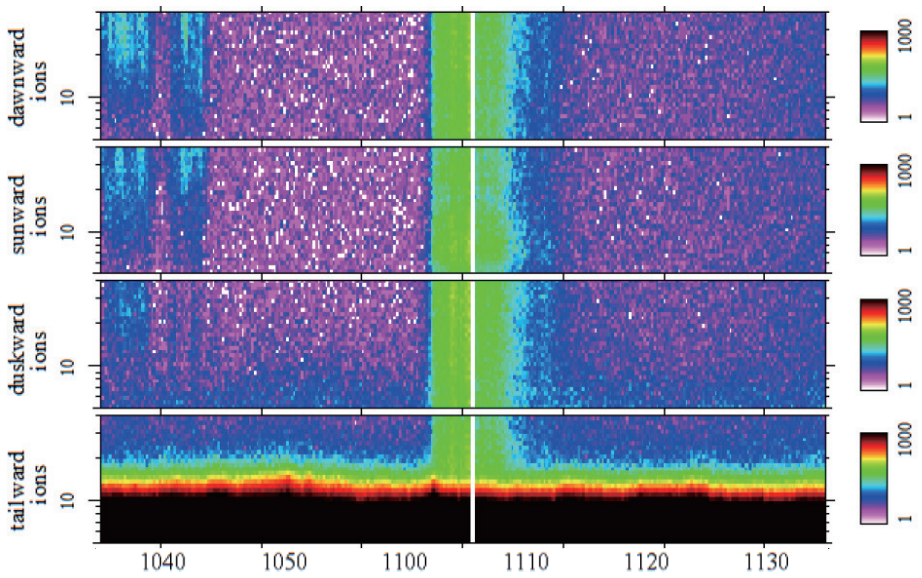

Figure 3.4: Count rates recorded by the LEP detector when this solar flare occurring on October 28, 2003 are color-coded (white-blue-green-yellow-red-black). The horizontal axis shows the universal time (HH:MM) of particle detection. The vertical axis shows the energy of nonthermal ions in units of energy-per-charge (5–40 keV/q). Four panels, top to bottom, show ion counts in the four sectors pointed dawnward, sunward, duskward, and tailward, respectively, where the ion flow directions are defined with respect to the relative magnetosphere geometry of the Sun and Earth.

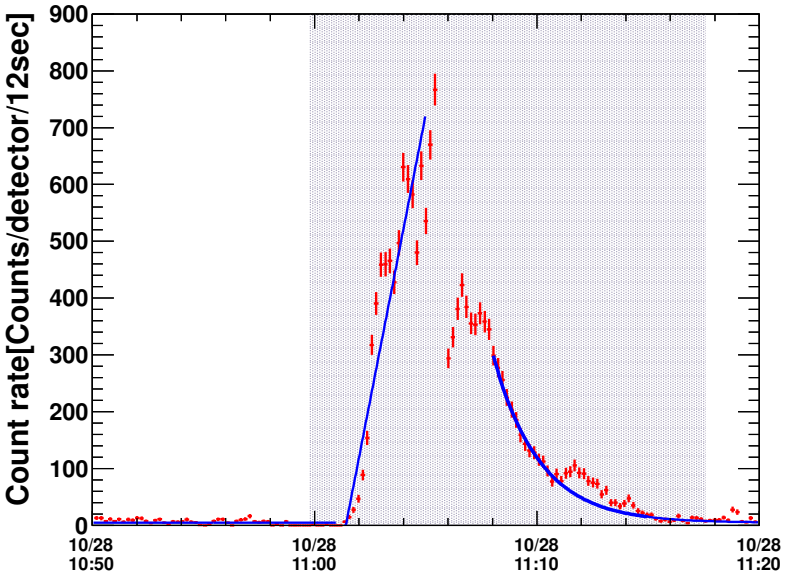

Figure 3.5: Light curve associated with the solar flare occurring on October, 28, 2003 as recorded by the GEOTAIL satellite. The horizontal axis shows the universal time, and the vertical axis shows count rate in units of [counts/detector/12 s]). Red points show the data, and blue lines show the fitting results. This flare is the same flare as shown in Fig. 3.4.

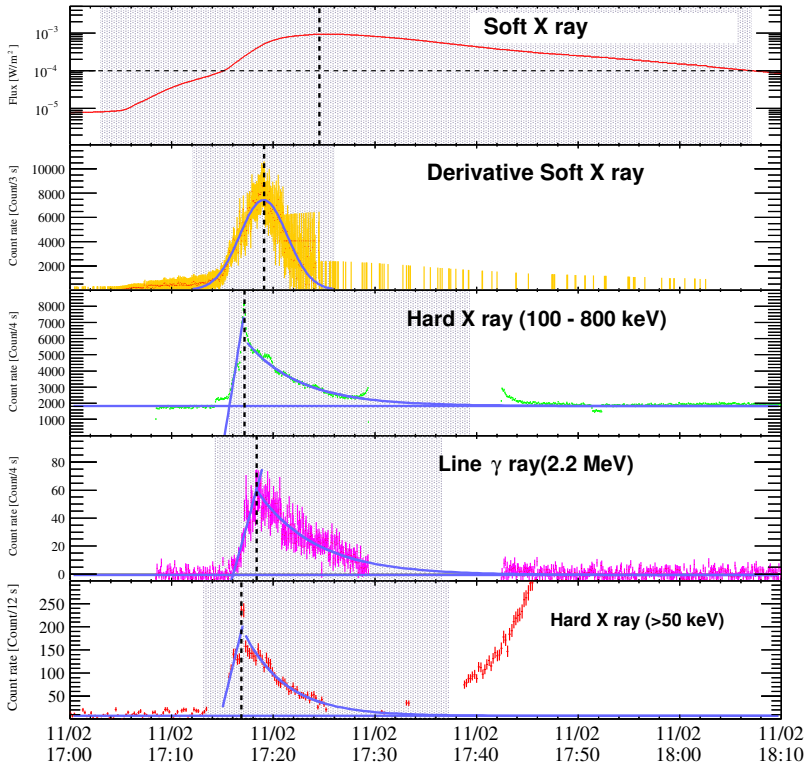

Figure 3.6: Light curves of the solar flare occurring on November 2, 2003. Gray regions show the time windows extracted by the analysis methods developed in this study. From top to bottom, the panels show the light curves for soft X-rays, derivative of soft X-rays, hard X-rays (100–800 keV), line γ-rays (2.223 MeV), and hard X-rays (GEOTAIL, above 50 keV), respectively. For the hard X-ray light curve (above 50 keV), the count rate gradually increased from 17:40 onward because protons in the range of 30–50 MeV were observed. These protons masked other counts due to plasma particles and hard X-ray photons.

Table 3.4: Time windows determined for soft X-rays, derivative of soft X-rays and hard X-rays. The time is described in units of UTC ([HH:MM:SS]).

Date	Soft X-rays (GOES)			Derivative of soft X-rays (GOES)			Hard X-rays (RHESSI)		
	t_{start}	t_{end}	Δt [s]	t_{start}	t_{end}	Δt [s]	t_{start}	t_{end}	Δt [s]
1997 Nov. 6	11:49:00	12:12:21	1,401	11:52:13	11:54:58	165	–	–	–
2000 Jul. 14	10:03:00	11:05:03	3,723	10:08:44	10:28:31	1,187	–	–	–
2001 Apr. 2	21:32:00	22:56:12	5,052	21:35:10	21:52:57	1,067	–	–	–
2001 Apr. 6	19:10:00	19:43:15	1,995	19:12:32	19:21:31	539	–	–	–
2001 Apr. 15	13:19:00	14:23:39	3,879	13:43:48	13:51:03	435	–	–	–
2001 Aug. 25	16:23:00	17:36:18	4,398	16:28:36	16:33:38	302	–	–	–
2001 Dec. 13	14:20:00	14:41:57	1,317	14:24:25	14:31:05	400	–	–	–
2002 Jul. 23	00:18:00	01:08:27	3,027	00:25:08	00:31:36	388	00:25:44	00:36:46	562
2003 Oct. 23	08:19:00	09:13:9	3,249	08:20:32	08:36:03	931	–	–	–
2003 Oct. 28	09:51:00	12:36:54	9,954	10:59:30	11:10:57	687	–	–	–
2003 Oct. 29	20:37:00	21:23:39	2,799	20:38:46	20:50:07	681	–	–	–
2003 Nov. 2	17:03:00	18:07:03	3,843	17:12:01	17:26:03	842	17:15:41	17:39:22	1421
2003 Nov. 4	19:29:00	21:10:12	6,072	19:36:59	19:56:03	1,144	–	–	–
2005 Jan. 20	06:36:00	08:05:48	5,388	06:39:22	06:57:12	1,070	06:43:27	06:57:57	870
2005 Sep. 7	17:17:00	18:48:57	5,517	17:23:34	17:39:48	974	–	–	–
2005 Sep. 8	20:52:00	21:31:48	2,388	21:00:27	21:08:05	458	–	–	–
2005 Sep. 9	19:13:00	21:20:36	7,656	–	–	–	–	–	–
2006 Dec. 5	10:18:00	10:56:09	2,289	10:24:18	10:35:43	685	–	–	–
2006 Dec. 6	18:29:00	19:16:30	2,850	18:41:29	18:47:06	337	18:42:33	18:49:19	406
2011 Aug. 9	07:48:00	08:11:47	1,427	08:00:50	08:05:40	290	–	–	–
2012 Mar. 7	00:02:00	01:31:34	5,374	00:04:21	00:25:16	1,255	–	–	–
2017 Sep. 6	11:53:00	13:30:00	5,820	11:54:39	12:03:20	521	–	–	–
2017 Sep. 10	15:35:00	17:26:06	6,666	15:49:12	16:06:32	1,040	15:54:42	16:19:03	1,461

Table 3.5: Time windows determined for line γ-rays (RHESSI) and hard X-rays (GEOTAIL). Time is described in units of UTC ([HH:MM:SS]).

Date	Line γ-ray (RHESSI)			Hard X-ray (GEOTAIL)		
	$t_{\rm start}$	$t_{\rm end}$	Δt [s]	$t_{\rm start}$	$t_{\rm end}$	Δt [s]
1997 Nov. 6	–	–	–	11:50:55	11:57:04	369
2000 Jul. 14	–	–	–	–	–	–
2001 Apr. 2	–	–	–	–	–	–
2001 Apr. 6	–	–	–	–	–	–
2001 Apr. 15	–	–	–	13:43:42	13:51:58	469
2001 Aug. 25	–	–	–	16:28:29	16:34:54	385
2001 Dec. 13	–	–	–	–	–	–
2002 Jul. 23	00:26:28	00:56:22	1,794	–	–	–
2003 Oct. 23	–	–	–	–	–	–
2003 Oct. 28	–	–	–	10:59:45	11:17:36	1,071
2003 Oct. 29	–	–	–	–	–	–
2003 Nov. 2	17:14:14	17:36:41	1,347	17:13:08	17:37:11	1,443
2003 Nov. 4	–	–	–	19:38:35	19:53:32	897
2005 Jan. 20	06:42:54	07:09:52	1,618	–	–	–
2005 Sep. 7	–	–	–	17:32:44	17:45:32	7678
2005 Sep. 8	–	–	–	–	–	–
2005 Sep. 9	–	–	–	–	–	–
2006 Dec. 5	–	–	–	–	–	–
2006 Dec. 6	–	–	–	–	–	–
2011 Aug. 9	–	–	–	–	–	–
2012 Mar. 7	–	–	–	–	–	–
2017 Sep. 6	–	–	–	–	–	–
2017 Sep. 10	–	–	–	–	–	–

Figure 3.8 shows the time duration of search windows as a function of the maximum value of the soft X-ray peak. The correlation coefficients between the maximum value of the soft X-ray peak and the time duration of search windows are 0.436 for soft X-rays, 0.341 for soft X-rays (derivative), 0.236 for hard X-rays (100–800 keV), -0.344 for line γ-rays, and 0.307 for hard X-rays (>50 keV). Therefore, no strong correlation is found among them, as summarized in Table 3.6.

To investigate the difference in time profile between channels, we calculated the time elapsed between the peak timing of a given channel and the peak timing of soft X-rays (Fig. 3.9), because the peak timing of each channel is earlier than that of soft X-rays. The mean differences are -320 s for the derivative of soft X-rays, -482 s for hard X-rays, -471 s for line γ-rays, and -342 s for hard X-rays (GEOTAIL).

Each panel in Fig. 3.10 shows the time correlation between two variables: on the x-axis, the peak timing of soft X-rays; on the y-axis, a given channel after subtracting the peak timing of soft X-rays. To extract the difference between peak timings, the plots are fitted with a linear function; the fitting results are summarized in Table 3.7. The y-intercept of the linear function gives the difference in peak timings.

In Fig. 3.10 (c), the fitting results are 0.9 ± 0.1 for the slope and 7 ± 55 s for the y-intercept. We found a good timing correlation between the derivative of soft X-rays and hard X-rays because the y-intercept is close to the origin of coordinates $(0, 0)$, thus confirming the Neupert effect

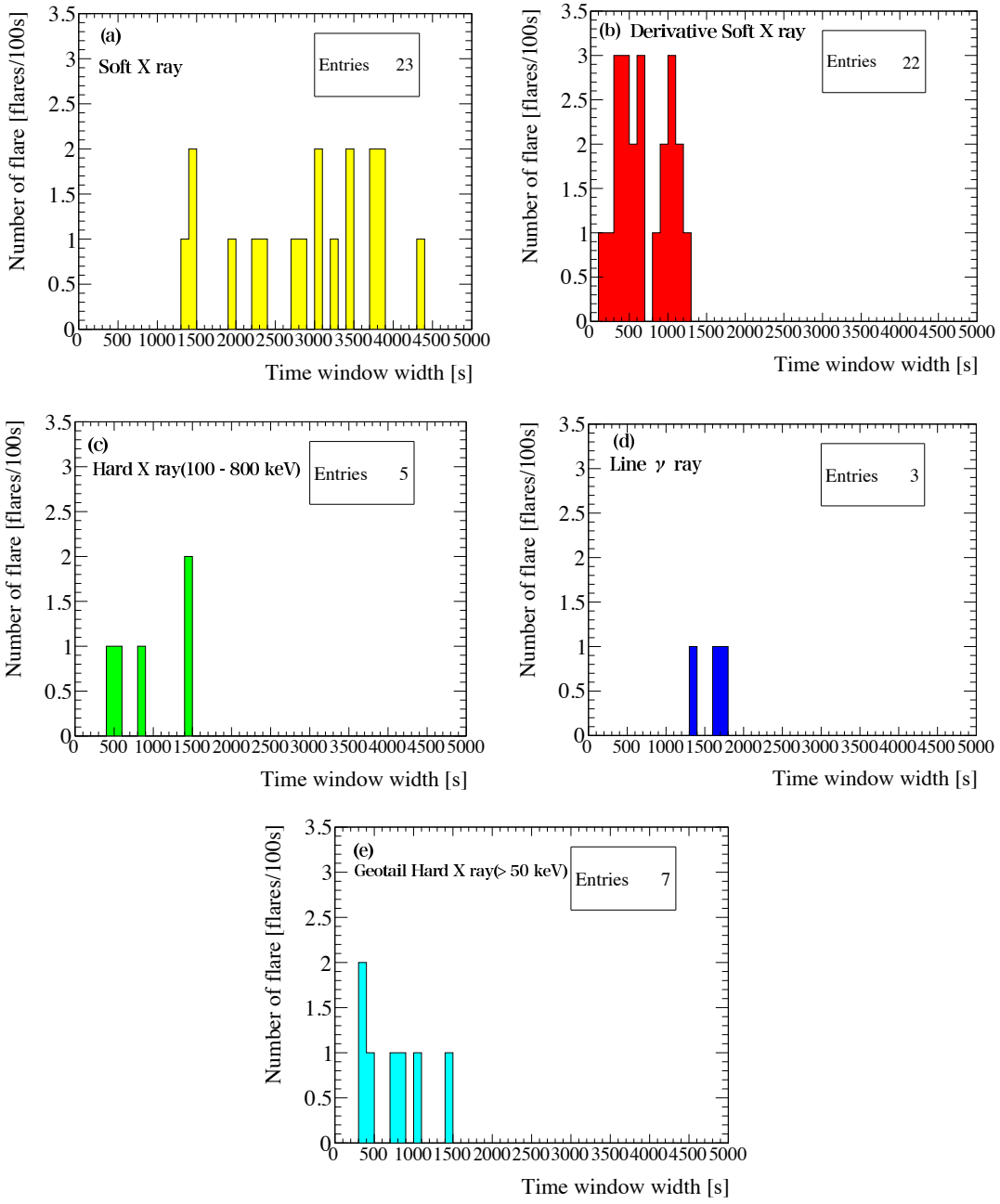

Figure 3.7: Distributions of the width of time window determined by each method: (a) light curve of soft X-rays, (b) derivative of the light curve of soft X-rays, (c) hard X-rays, (d) line γ-rays, and (e) hard X-rays (GEOTAIL). The Horizontal axis shows the duration of the time window. The vertical axis shows the number of entries.

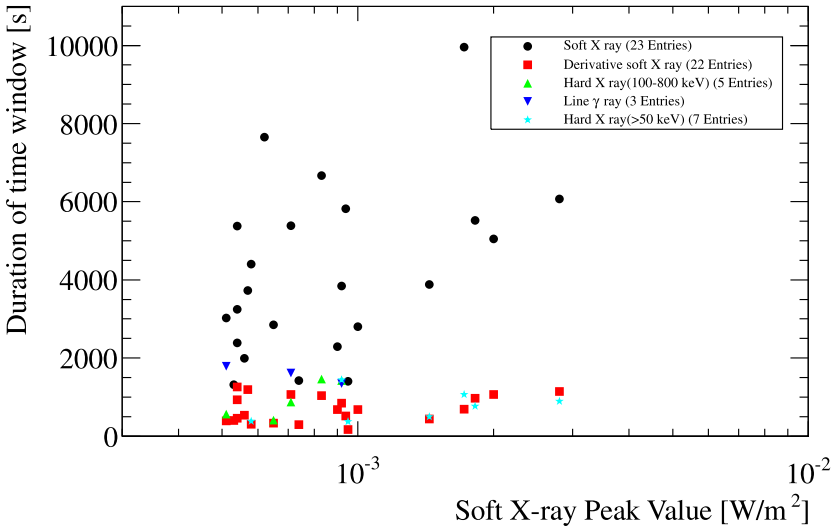

Figure 3.8: Time duration as a function of the peak intensity of soft X-ray. Black dots, Red squares, Green up-triangles, Blue down-triangles, and Light blue stars show soft X-ray, Detivative of soft X-ray, Hard X-ray(100–800 keV), Line γ-ray, and Hard X-ray(above 50 keV) emissions, respectively.

Table 3.6: Summary of timing information obtained in this study. Average time durations are calculated from the distributions shown in Fig. 3.7. Correlation coefficients are calculated from the distribution shown in Fig. 3.8. The differences in peak timing are calculated relative to a soft X-ray peak time of 0 (Fig. 3.9).

	Entries	Average duration [s]	Correlation coefficient	Peak timing difference [s]
Soft X-ray	23	4,178	0.436	–
Soft X-ray (derivative)	22	700	0.341	−320
Hard X-ray	5	944	0.236	−482
Line γ-ray	3	1,586	−0.344	−471
Hard X-ray (GEOTAIL)	7	776	0.307	−342

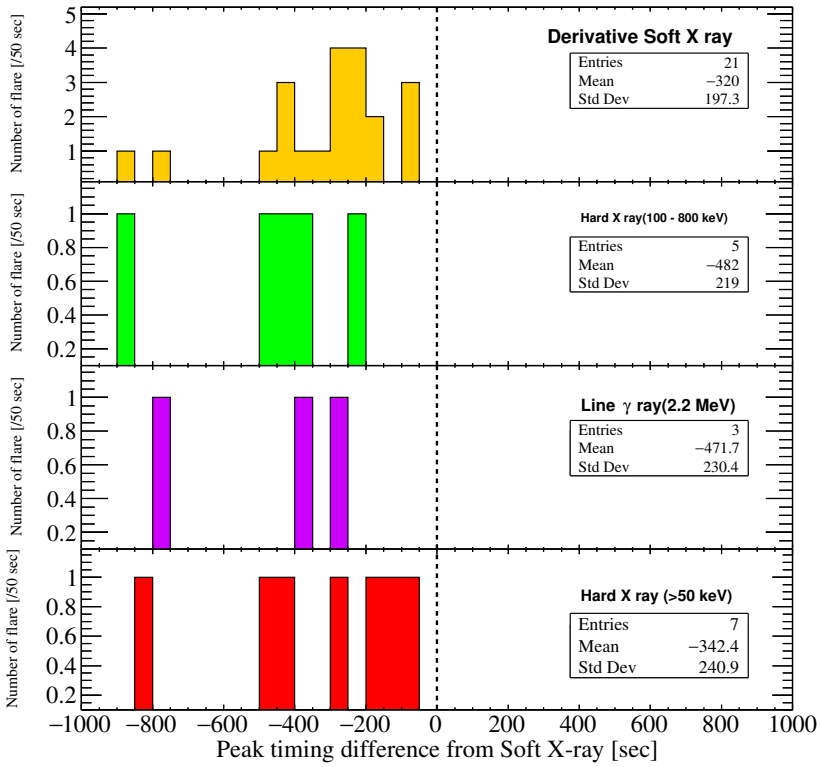

Figure 3.9: Time difference distribution after subtracting the peak timing of soft X-rays. The horizontal axis shows the time difference in units of seconds; the vertical axis shows the entry per 50 s.

Table 3.7: Summary of results from fits in Fig. 3.10. Each axis in Fig. 3.10 represents the time elapsed between the peak timing of a given channel and that of soft X-rays.

Figure 3.10	x-axis	y-axis	Fitting result	χ^2/d.o.f
(a)	Soft X-ray (derivative)	Hard X-ray (100–800 keV)	$(1.1 \pm 0.4)x$ $+(41 \pm 166)$	1.0/3
(b)	Soft X-ray (derivative)	Line γ-ray	$(1.4 \pm 1.1)x$ $+(331 \pm 548)$	0.3/1
(c)	Soft X-ray (derivative)	Hard X-ray (>50 keV)	$(0.9 \pm 0.1)x$ $+(7 \pm 55)$	0.3/4
(d)	Hard X-ray (100–800 keV)	Line γ-ray	$(1.0 \pm 0.5)x$ (141 ± 286)	0.1/1

between them. Notably, this confirmation takes place by comparing the peak timing without considering the shape of light curves.

In Fig. 3.10 (d), the y-intercept is 141 ± 285 s, suggesting that the peak timing of line γ-rays is delayed from that of hard X-rays (100–800 keV). If the acceleration of both electrons and ions occurs simultaneously, this difference between their timings is explained by considering neutron capture since the neutron capture time is estimated to be 100 sec [70, 75].

Figure 3.10 (e) overlays the plots shown in Fig. 3.10 (a) and Fig. 3.10 (b). We found that the peak timing of hard X-rays is earlier than that of line γ-rays, where their difference is about 100 s.

3.3 The Invisible Side Solar Flares

3.3.1 Search window for solar flares at invisible side

As briefly explained in Section 1.6, proton flux directed back to the Sun generates a nuclear cascade in the solar atmosphere. Such flux results in a narrow beam of relativistic protons with a rather hard spectrum from solar flares on the invisible side of the Sun. Hence the searches for neutrinos associated with solar flares occurring at the invisible side provide information about the acceleration mechanism of downward going proton flux. However, no satellite, except for a limited number of planet explorers, directly monitors an explosive phenomenon at the invisible side before the launch of STEREO (*Solar Terrestrial Relations Observatory*) satellites in 2006 [76]. The STEREO satellites have performed the CME imaging [77] and indeed observed the solar high energy particles originated from the CMEs occurring on July 23rd, 2012 [78].

The time of CMEs allows one to infer the occurrence time of a solar flare on the invisible side of the Sun because large energetic solar flares are usually accompanied by CMEs. Andrews [79] found the association rate of CMEs with solar flares increases with the flare's peak flux of soft X-rays, fluence, and time duration.

As explained in Section 1.4, the observation of CMEs occurring on the invisible side of the Sun is performed by coronagraph method with the LASCO on SOHO. The catalog of CMEs observed by the SOHO spacecraft is maintained by NASA [29][1] and this catalog summarizes the time of CMEs and its locations.

[1] `https://cdaw.gsfc.nasa.gov/CME_list/`

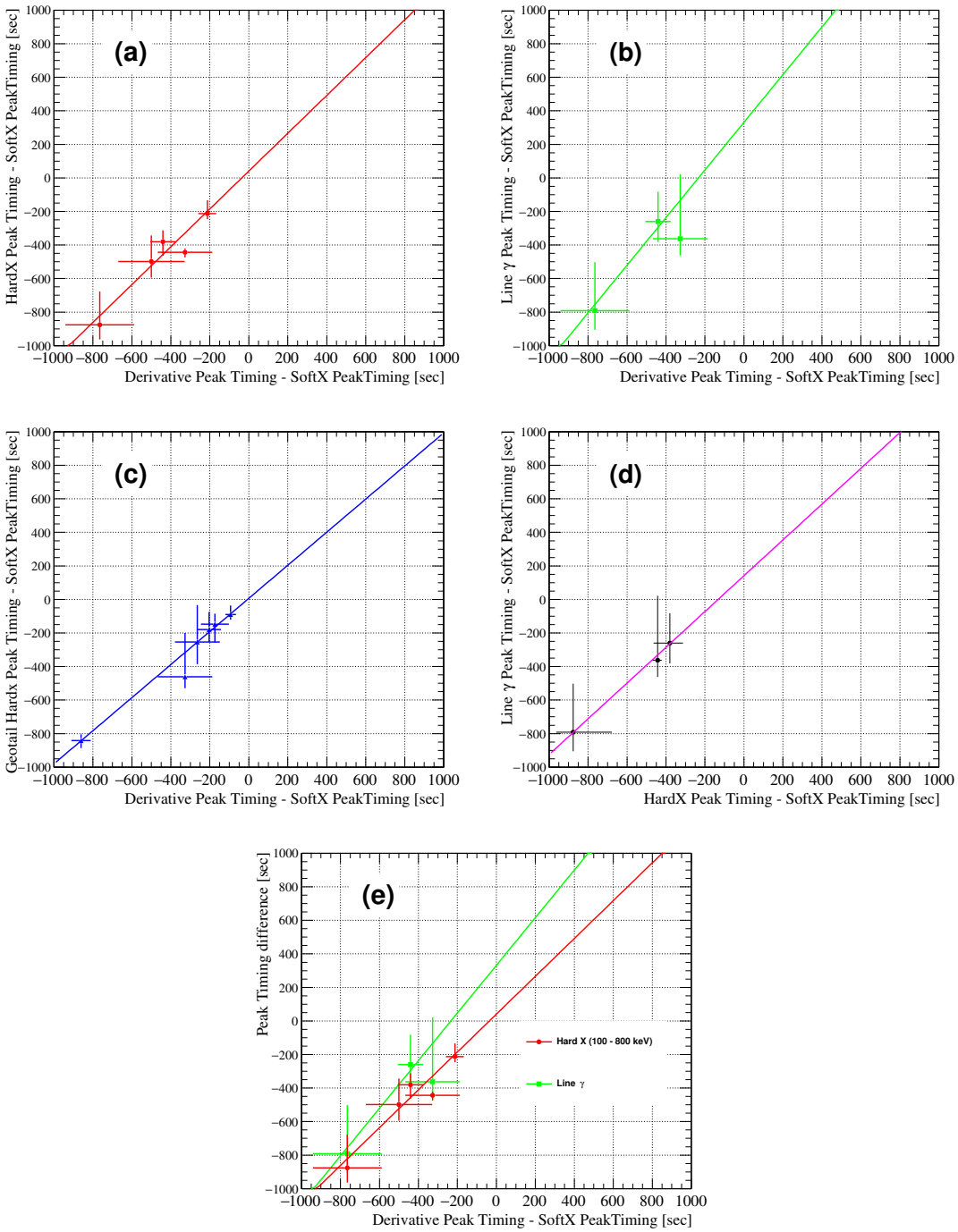

Figure 3.10: Relationship between each channel's peak timing after subtracting the peak time of soft X-rays. The fitting results are summarized in Table 3.7. For (e), the plots shown in both (a) and (b) are overlaid.

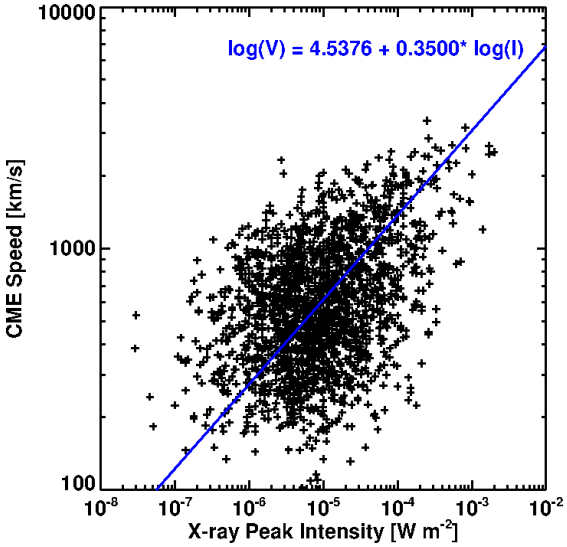

Figure 3.11: The correlation between the speed of the CMEs and the peak intensity of soft X-rays from solar flares monitored by the GOES satellite. The black plus signs show the parameters taken from the catalog [29]. The blue line shows the regression line.

3.3.2 Solar Flare Event Selection

Yashiro *et.al.* [29] statistically examined a possible correlation between the kinetic energy of CMEs and the intensity of the solar flare monitored by the GOES satellite and found a weak positive correlation between them. Based on that study, we collected about 20,000 CMEs listed in NASA and evaluated the threshold of the speed of CMEs associated with the solar flare with X class. Figure 3.11 shows the correlation between the speed of the CMEs and the intensity of soft X-rays from solar flares. As expected, we found a weak positive correlation between them. Finally, we conservatively determined the threshold as 2000 $\mathrm{km\,s^{-1}}$ in order to select the solar flare of X class. This criterion roughly corresponds to solar flares with X2.0.

3.3.3 Time Window Determination

Yashiro *et.al.* [29] also investigated the time difference between the CMEs and the solar flares. That study found the standard deviation of time difference is 1020 s from its distribution. In this study, we set the start time of the search window to be 3060 s before the time of CMEs emission, which corresponds to three standard deviation of the time difference. For the end time, we conservatively set 4178 s after the time of CME emission, where this wide duration is determined from the light curve of soft X-ray recorded by GOES since all processes, such as acceleration, energy release, etc, occurring during a solar flare complete within this time duration. Hence, the search window for solar flares occurring on the invisible side of the Sun is the same time duration, which corresponds to 7238 s in total.

In this analysis, we selected energetic CMEs whose speed is more than 2000 $\mathrm{km\,s^{-1}}$. Ten CMEs from 1996 April to 2018 May were selected with this criterion. Table 3.8 summarizes the date, search window and location of the selected CMEs.

Table 3.8: The summary of the search windows estimated in this study for energetic CMEs occurring on the invisible side of the Sun. The date, time, and active region (AR) are taken from SOHO LASCO CME CATALOG [29].

Date	Time [UTC]	$t_{\rm start}$	$t_{\rm end}$	AR location	Speed [$\mathrm{km\,s^{-1}}$]
2001 Apr. 18	02:06:24	01:15:24	03:16:02	SW90b	2464.2
2002 Jul. 18	18:58:20	18:07:20	20:07:58	E90b	2191.3
2002 Jul. 19	16:04:34	15:13:34	17:14:12	S15E90	2046.6
2003 Nov. 2	09:00:23	15:13:34	17:14:12	SW90b	2036.0
2003 Nov. 7	15:32:19	14:41:19	16:41:57	W90b	2237.0
2003 Nov. 9	05:57:57	05:06:57	07:45:29	E90b	2008.1
2005 Jul. 24	13:35:51	12:44:51	14:45:29	E90b	2527.8
2011 Jun. 4	21:42:42	20:51:42	22:52:20	N16W153	2425.5
2012 Jul. 23	02:10:07	01:19:07	03:19:45	S17W132	2003.2
2014 Dec. 13	13:57:34	13:06:34	15:07:12	S20W143	2221.6

3.4 Summary of the Search Time Windows

We determined the search time windows with the time profile of soft X-ray, the derivative of soft X-ray, hard X-ray, and line γ-ray emissions for the twenty-three solar flares on the visible side. The line γ-rays should be from hadronic processes and directly indicate neutrino existence in a solar flare. This method can be applied to three solar flares. The derivative of soft X-ray light curve can be applied to all solar flares observed by GOES and would be substituted for the time window determined by the γ-ray emission from π^0. For the reason above, the search time windows that are determined from the line γ-rays and the derivative of soft X-rays are finally used in this study.

We determined the search time window for ten solar flares on the invisible side with CME data from LASCO. Although the time window was almost 10 times longer than that for the solar flares on the visible side, it enabled us to search for the solar flares on the invisible side.

Tables 3.9 and 3.10 show summaries of time windows which are used to search for solar flare neutrinos in this study.

Table 3.9: The time windows that used to search for neutrinos from solar flares on the visible side in this study. The time is described in units of UTC ([HH:MM:SS]).

Date	Derivative of soft X-rays (GOES)			Line γ-ray (RHESSI)		
	start	end	duration [s]	start	end	duration [s]
1997 Nov. 6	11:52:13	11:54:58	165	–	–	–
2000 Jul. 14	10:08:44	10:28:31	1,187	–	–	–
2001 Apr. 2	21:35:10	21:52:57	1,067	–	–	–
2001 Apr. 6	19:12:32	19:21:31	539	–	–	–
2001 Apr. 15	13:43:48	13:51:03	435	–	–	–
2001 Aug. 25	16:28:36	16:33:38	302	–	–	–
2001 Dec. 13	14:24:25	14:31:05	400	–	–	–
2002 Jul. 23	00:25:08	00:31:36	388	00:26:28	00:56:22	1,794
2003 Oct. 23	08:20:32	08:36:03	931	–	–	–
2003 Oct. 28	10:59:30	11:10:57	687	–	–	–
2003 Oct. 29	20:38:46	20:50:07	681	–	–	–
2003 Nov. 2	17:12:01	17:26:03	842	17:14:14	17:36:41	1,347
2003 Nov. 4	19:36:59	19:56:03	1,144	–	–	–
2005 Jan. 20	06:39:22	06:57:12	1,070	06:42:54	07:09:52	1,618
2005 Sep. 7	17:23:34	17:39:48	974	–	–	–
2005 Sep. 8	21:00:27	21:08:05	458	–	–	–
2005 Sep. 9	19:13:00	21:20:36	7,656	–	–	–
2006 Dec. 5	10:24:18	10:35:43	685	–	–	–
2006 Dec. 6	18:41:29	18:47:06	337	–	–	–
2011 Aug. 9	08:00:50	08:05:40	290	–	–	–
2012 Mar. 7	00:04:21	00:25:16	1,255	–	–	–
2017 Sep. 6	11:54:39	12:03:20	521	–	–	–
2017 Sep. 10	15:49:12	16:06:32	1,040	–	–	–

Table 3.10: The time windows that used to search for neutrinos from solar flares on the invisible side in this study. The time is described in units of UTC ([HH:MM:SS]). The durations are 7238 s for all solar flares in this table.

Date	start	end
2001 Apr. 18	01:15:24	03:16:02
2002 Jul. 18	18:07:20	20:07:58
2002 Jul. 19	15:13:34	17:14:12
2003 Nov. 2	15:13:34	17:14:12
2003 Nov. 7	14:41:19	16:41:57
2003 Nov. 9	05:06:57	07:45:29
2005 Jul. 24	12:44:51	14:45:29
2011 Jun. 4	20:51:42	22:52:20
2012 Jul. 23	01:19:07	03:19:45
2014 Dec. 13	13:06:34	15:07:12

Chapter 4

Detector Calibration

In this chapter, ID PMT calibration, water transparency calibration, and energy scale calibration in SK are briefly described. A more detailed explanation about the calibrations is described in Ref. [80].

4.1 ID PMT Calibraion

The energy and vertex of an event are reconstructed from the charge and timing information of hit PMTs.

Relative Gain of Each PMT

In order to calibrate the charge of the PMT, gain, a factor that converts from the observed charge in a PMT in a unit of pico Coulomb (pC) to the number of photoelectrons, is needed. There were two steps to obtain this value for all PMTs. First, the relative difference of the PMT gain, which is called "Relative gain", is measured, Then, the overall average gain, which is called "Absolute gain", is determined.

To measure the relative gain difference, a stable light source emitting constant-intensity flashes is deployed at a certain position in the tank. There are two measurements: the first uses high-intensity flashes from which every PMT gets multiple photoelectrons. The second measurement uses low-intensity flashes in which tens of PMTs get hits, i.e. occupancy of hits in each PMT is much less than 0.1, and the observed charge is mainly from single photoelectron. The average charge for the ith PMT, $Q_{\mathrm{obs},i}$ of the first measurement and the number of hits for the ith PMT, $N_{\mathrm{obs},i}$, from the second measurement can be parameterized as follows:

$$Q_{\mathrm{obs},i} \propto I_{\mathrm{s}} \times a_i \times \varepsilon_{\mathrm{qe},i} \times G_i, \tag{4.1.1}$$

$$N_{\mathrm{obs},i} \propto I_{\mathrm{w}} \times a_i \times \varepsilon_{\mathrm{qe},i} \tag{4.1.2}$$

where I_{s} and I_{w} are the aberage intensities of high and low intensity flashes, respectively, a_i is acceptance of ith PMT, $\varepsilon_{\mathrm{qe},i}$ is quantum efficiency (QE), and G_i is the ith PMT's gain. Then, relative gain of each PMT was extracted by taking the ratio of Eqs.4.1.1 and 4.1.2. Figure 4.1 shows the distribution of the relative gain of the ID PMTs after being normalized by the overall average gain.

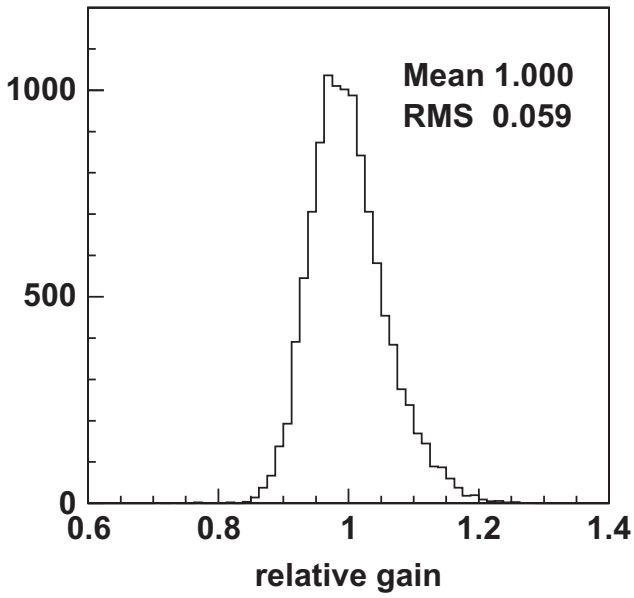

Figure 4.1: Relative gain distribution of the ID PMTs. Values are normalized to their mean value. Taken from [80]

Absolute Gain

The absolute gain is determined using the charge distribution of the single photoelectron signal and is obtained using a Ni-Cf source calibration. Figure 4.2 is a picture of the Ni-Cf source which is used in SK. γ-rays with total energy of 7-9 MeV from thermal neutron capture on nickel emit Cherenkov photons, and the photon yield is about 0.004 p.e.′s/PMT/event. These signals are considered to be single photoelectron contributions. The observed charge distribution is shown in Fig. 4.3. The mean value of the charge distribution corresponds to the absolute gain value and it is shown in Tab. 4.1.

Table 4.1: Summary of absolute gain values in SK.

SK Phase	Absolute gain value [pC/p.e.]
SK-I	2.055
SK-II	2.297
SK-III	2.243
SK-IV	2.645

Relative QE

In order to measure energy using the number of photoelectrons from PMTs, the QE of each PMT is also needed. How to determine the relative QE for each PMT is described here. If the intensity of a light source is low enough, the observed hit probability should be proportional to the QE, as can be seen from Eq. 4.1.2. A MC simulation is used to predict the number of photons arriving

Figure 4.2: Picture of Ni-Cf source. This ball is made of 6.5 kg of NiO and 3.5 kg of polyethylene. The Cf source (neutron source) was inserted into the center of the ball. Taken from [80].

at each PMT and we took the ratio of the observed number of hits to the predicted number of hits. It is noted that when this calibration was conducted, the water was convected in the entire detector to make its quality uniform and the remaining cause of the geometrical effect is only the acceptance from the source to each PMT. Figure 4.4 shows the position dependence of the photon detection probability of each PMT. In Fig. 4.4, the number of observed hits is corrected with the distance between the Ni-Cf source and the position of ith PMT, r_i, as well as the PMT acceptance a_i:

$$N_{\mathrm{obs},i} \times r_i^2 / a_i. \tag{4.1.3}$$

Even after this correction, some position dependence remains because of reflection from neighboring surfaces, and scattering and absorption by the water. These further corrections were estimated by the MC. Once these light propagation effects are considered, the remaining difference is attributed to the QE of individual PMTs.

Timing Calibration

The time response of each readout channel, including PMTs and readout electronics, has to be calibrated for precise reconstruction of the event vertices and track directions. The response time of readout channels can vary due to differences in transit time of PMTs, lengths of PMT signal cables, and relative differences of readout electronics. In addition, the response time of readout channels depends on the detected charge of PMTs, since the rise time of a large pulse is faster than that of a smaller one. This is called the "time-walk" effect. This was calibrated by injecting various intensities of light into PMTs. A schematic diagram of the timing calibration system is shown in Fig. 4.9. A nitrogen laser light source whose wavelength is shifted to 398 nm by a dye is used. The nitrogen laser pulse is split into two outputs, one goes to the trigger PMT which creates an external trigger for timing calibration events, and the other is sent to the dye laser module to generate laser pulses. The dye laser pulse with a wavelength of 398 nm and a

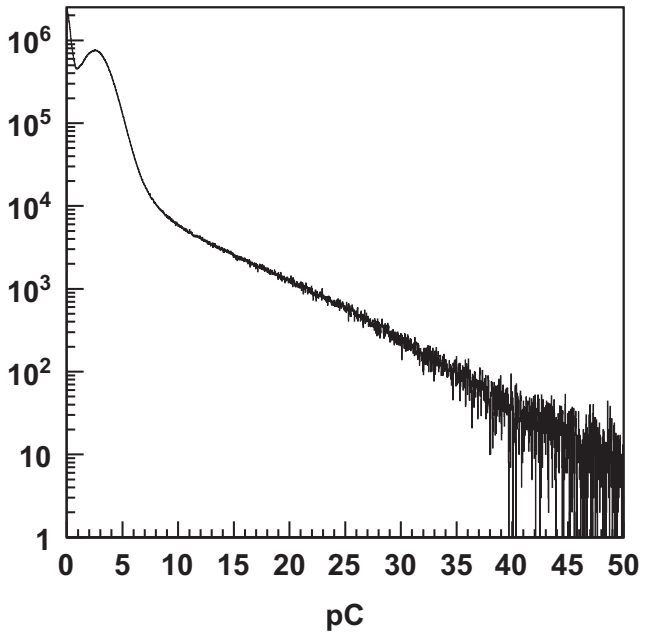

Figure 4.3: Charge distribution in units of pC obtained in the absolute gain calibration. Taken from [80].

pulse width of 0.2 ns passes through a variable filter to adjust the laser intensity. The filtered light is distributed into the whole ID PMTs through a diffuser ball.

From this calibration, two-dimensional correlation distribution of timing versus pulse height (charge) called " TQ-distributions " is obtained. A typical TQ distribution for one readout channel is shown in Fig. 4.6. Calibration constants, called the " TQ-map ", are derived by fitting the TQ distribution to polynomial functions. The timing resolution of the SK detector is evaluated using the vertically sliced distributions of the TQ-distribution. This was conducted by fitting the sliced one-dimentinal timing distribution for each charge region with an asymmetric Gaussian:

$$f(t) = \begin{cases} A_1 \exp\left(\dfrac{-(t-T_{\rm peak})^2}{\sigma_t^2}\right) + B_1 (t > T_{\rm peak}) \\ A_2 \exp\left(\dfrac{-(t-T_{\rm peak})^2}{\sigma'^2_t}\right) + B_2 (t \leq T_{\rm peak}) \end{cases} \tag{4.1.4}$$

where A_1, A_2, B_1, B_2, σ_t and σ'_t are fit parameters. A typical timing distribution for a certain charge region and fit functions are shown in Fig. 4.7. The obtained timing resolutions are plotted as a function of observed charge in Fig. 4.8.

4.2 Water Transparency

Water transparency is important in determining the number of generated Cherenkov photons from the number of observed photoelectrons because the photons are observed after passing

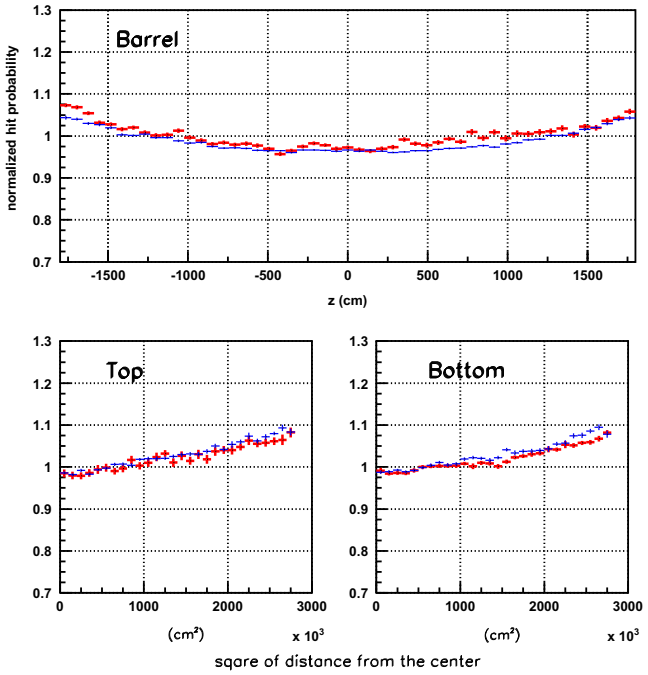

Figure 4.4: The position dependence of the photon detection probability in the detector. The vertical axis values are normalized by the average value of all PMTs. The top plot shows the PMTs on the sidewall, and the horizontal axis is the Z position of PMTs in cm. The bottom left (right) plot shows the top (bottom) PMTs, and the horizontal axis is the square of the distance from the detector center in unit of cm^2. red points show data and blue points show MC. Taken from [80]

through the water in the tank. To calibrate the absorption and scattering of light in water, lasers that have various wavelengths are used. Figure 4.9 shows the schematic view of the calibration system for water transparency. The sidewall of the detector is divided into five regions, and the parameters of the scattering component are estimated from the hit timing and charge of the PMTs in each region. Water absorption and scattering parameters are determined by comparing MC simulations with data obtained from laser irradiation. Figure 4.10 shows the comparison of Time-Of-Flight subtracted hit timing distributions between best-tuned laser MC and calibration data. The number of photons with a wavelength (λ) in water decreases gradually according to

$$I(\lambda) = I_0(\lambda)\exp(-l/L(\lambda)) \tag{4.2.1}$$

where l is the travel length of the light, $I_0(\lambda)$ is the initial intensity, $I(\lambda)$ is the intensity at l, and $L(\lambda)$ is the total attenuation length caused by scattering and absorption, which we call water transparency. The total attenuation length caused by scattering and absorption, $L(\lambda)$, is defined as

$$L(\lambda) = \frac{1}{\alpha_{\rm abs}(\lambda) + \alpha_{\rm sym}(\lambda) + \alpha_{\rm asymm}(\lambda)} \tag{4.2.2}$$

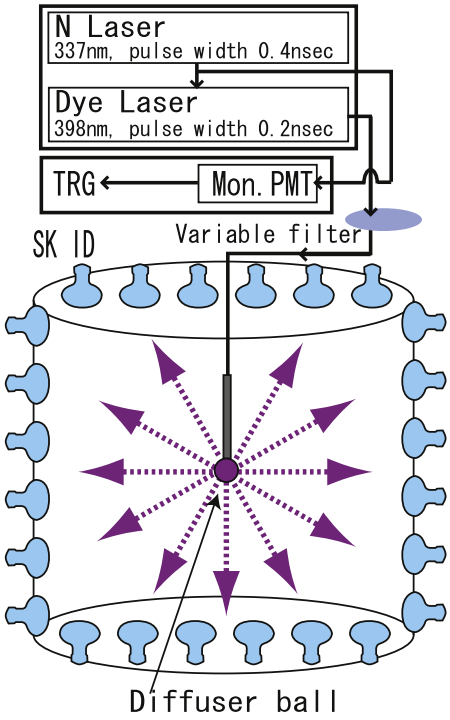

Figure 4.5: The schematic diagram of the timing calibration system. Taken from [80]

where $\alpha_{\rm abs}(\lambda)$, $\alpha_{\rm sym}(\lambda)$ and $\alpha_{\rm asymm}(\lambda)$ are parameters for absorption, symmetric scattering and asymmetric scattering, respectively. Those factors are parametrized as follows:

$$\alpha_{\rm abs}(\lambda) = P_0 \times \frac{P_1}{\lambda^4} + C, \tag{4.2.3}$$

$$\alpha_{\rm sym}(\lambda) = \frac{P_4}{\lambda^4} \times \left(1.0 + \frac{P_5}{\lambda^2}\right), \tag{4.2.4}$$

$$\alpha_{\rm asymm}(\lambda) = P_6 \times \left(1.0 + \frac{P_7}{\lambda^4} \times (\lambda - P_8)^2\right), \tag{4.2.5}$$

where the second term C in the first line is the amplitude based on the experimental data for > 464 nm [81] and $C = P_0 \times P_2 \times (\lambda/500)^{P_3}$ for < 464 nm, P_{0-8} are constant coefficients.

These parameters are used in MC and tuned by this calibration. Figure 4.11 shows typical fitted water parameters used in MC. The points are the data obtained in April 2009.

The water transparency is also measured by the Cherenkov light from cosmic ray muons passing through the detector. The water transparency measured by cosmic ray muons gives an averaged water transparency weighted over the spectrum of Cherenkov photons and the quantum efficiency as a function of wavelength. Since this transparency is essentially what we need in the physics analysis, this water transparency is used for correcting the number of hit PMTs and the number of photoelectrons for the energy measurement. Details of the method to measure the water transparency by muons are described in Ref. [80]. Figure. 4.12 shows the measured water transparency over the period analyzed in this thesis.

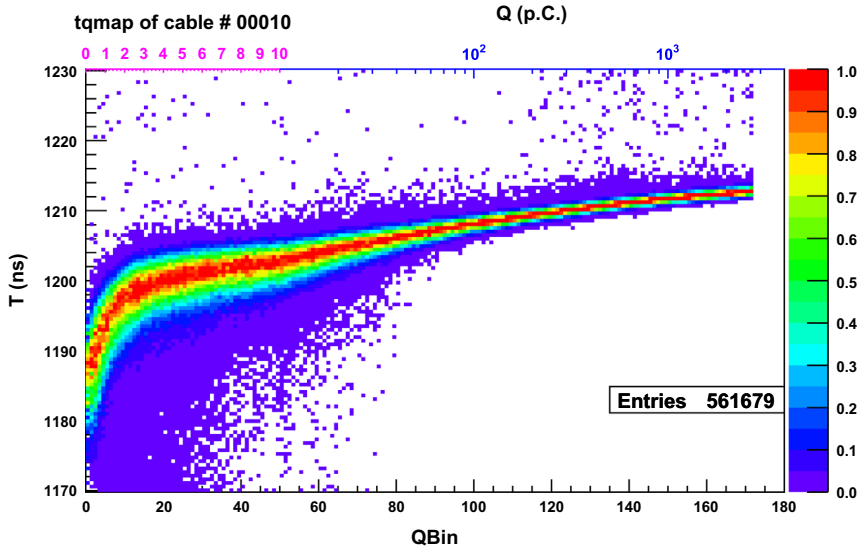

Figure 4.6: A typical TQ distribution for one readout channel. The horizontal axis corresponds to observed charge. The vertical axis shows detection timing. Larger value in the vertical axis corresponds to earlier hits in this plot. Taken from [80]

4.3 Absolute Energy Calibration

The method used for the absolute energy calibration in SK depends on the energy range. The methods (or control samples) which are listed below are related with this study.

- "High" energy stopping muons (1-10 GeV)
- "Low" energy stopping muons (200-500 MeV)
- γ-rays from neutral pions (about 130 MeV)
- Decay electrons from stopping muons (about 50 MeV)
- LINAC calibration (below 20MeV)

The accuracy of the absolute energy scale is checked by comparing data from all calibration sources with the MC simulation.

"High" Energy Stopping Muons

For energy calibration, muon events that stopped in SK, which is called "stopping muons", are used. The momentum of Cosmic-Ray (CR) muon can be determined by track length since the energy loss ($\mathrm{d}E/\mathrm{d}x$) is approximately constant in water. The track length is defined by the distance between the entering position at the detector and the vertex position of the subsequent decay electron. Stopping muons which satisfy the following criteria are used:

- The entering position is at the top wall of the detector.
- The direction is downward.
- Only one decay electron is detected.

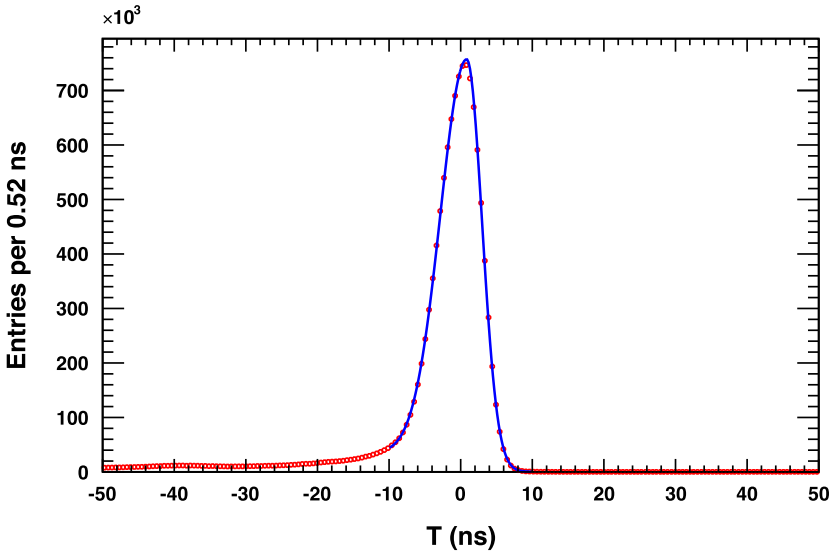

Figure 4.7: Timing distribution added over all the readout channels. The observed charge region used in the distribution is about 3 pC (1 photoelectron level). The result of the fit to an asymmetric Gaussian is shown by the solid curve. Taken from [80]

- Reconstructed range of the muon track is $7 < L < 30$ m.

The first three criteria are used to select vertical downward-going muons that have a clear Cherenkov ring. Therefore, it can be well reconstructed. The fourth criterion selects high energy muon events.

"Low" Energy Stopping Muons

The momentum of stopping muons having low energy (< 500 MeV/c) can be estimated using the Cherenkov angle. The relationship between the Cherenkov angle and momentum can be expressed as follows:

$$\cos\theta_{\rm c} \quad = \quad \frac{1}{n\beta} = \frac{1}{n}\sqrt{1+\frac{m^2}{P^2(\theta_{\rm c})}} \tag{4.3.1}$$

where $\theta_{\rm c}$ is the Cherenkov angle, $n \sim 1.33$ is the refraction index of water, β is the speed of muon in a unit of speed of light (c), m is the invariant mass, and P is momentum, respectively. Stopping muons which satisfy the following criteria are used:

- The entering position is at the top wall of the detector.
- The direction is downward.
- Only one decay electron is detected.
- Total number of photoelectrons in the ID is less than 1,500 p.e.′s (750 p.e.′s for SK-II).

The first three criteria are the same as those for the "high" energy stopping muon events. The fourth criterion selects "low" energy cosmic muons having momenta less than 380 MeV/c.

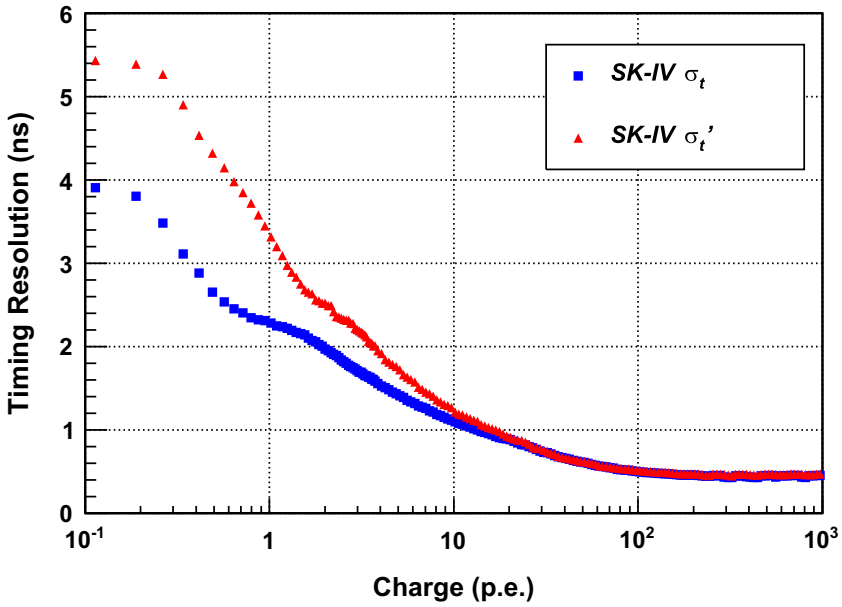

Figure 4.8: Timing resolution σ_t (square) and σ'_t (triangle) as a function of charge (photoelectron) for SK-IV. Taken from [80]

γ-rays from Neutral Pions

Single π^0 events are produced by Neutral Current (NC) interactions of atmospheric neutrinos in the detector. The π_0 decays into two photons with a lifetime of 8.5×10^{-17} sec, i.e. almost immediately in the water Cherenkov detectors. The invariant mass of π_0 can be calculated using the reconstructed momentum of two γ-rays as

$$M_{\pi_0} = \sqrt{2P_{\gamma,1}P_{\gamma,2}(1-\cos\theta)} \tag{4.3.2}$$

where $P_{\gamma,1}$ and $P_{\gamma,2}$ are the momenta of the two obserbed γ-rays, and θ is the opening angle between the γ-rays. π_0 like events which satisfy the following criteria are used:

- Two electron-like rings are detected.
- An electron from muon decay is not detected.
- Vertex position is reconstructed within the Fiducial Volume (FV).

The second criterion rejects events in which charged pions are produced with the π^0 or Charged Current (CC) events.

Decay Electrons from Stopping Muons

Stopping muons produce decay electron events. Decay electrons have a continuous energy spectrum which is called the Michel spectrum. The mean of the energy spectrum is about 37 MeV. The selection criteria for decay electron are listed follows:

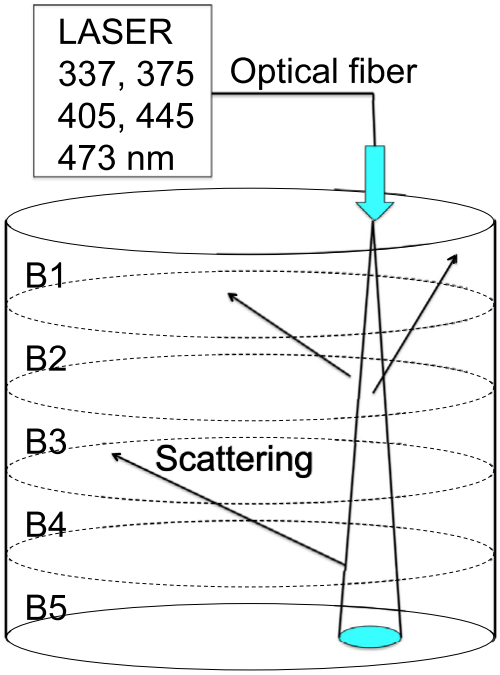

Figure 4.9: The schematic view of the calibration system for water transparency. The side wall of the detector is divided into five regions, and the parameters of the scattering component are estimated from the hit timing and charge of the PMTs in each region. Taken from [80]

- Time interval from a stopping muon is 2.0 to 8.0 μsec.
- The number of hit PMTs in a 50 nsec window is greater than 60 hits (30 hits for SK-II).
- The goodness of vertex fit which is defined as Eq. 6.2.6 is greater than 0.5.
- Vertex position is reconstructed within the FV

The first criterion involves the efficient timing of decay electron tagging. The second criterion rejects γ-rays of 6 MeV or more emitted from muon capture on nucleons.

The absolute energy scale is calibrated by various methods for different momentum ranges. To estimate the systematic uncertainty of the energy scale, the ratio of values between data and MC in each calibration method is used as shown in Fig. 4.13.

LINAC calibration

For energy calibration for lowest energy region ($3.5 < E < 20$ MeV) in SK analysis, a linear accelerator (LINAC) for electrons is used [83]. Since the calibration hole positions are fixed and the length of the beam pipe is also fixed, the calibration data were taken at the fixed 9 points as shown in Fig. 4.14.

In order to measure the energy of the single electron generated by the LINAC calibration system, a germanium detector is used. This germanium detector is calibrated with γ-rays from

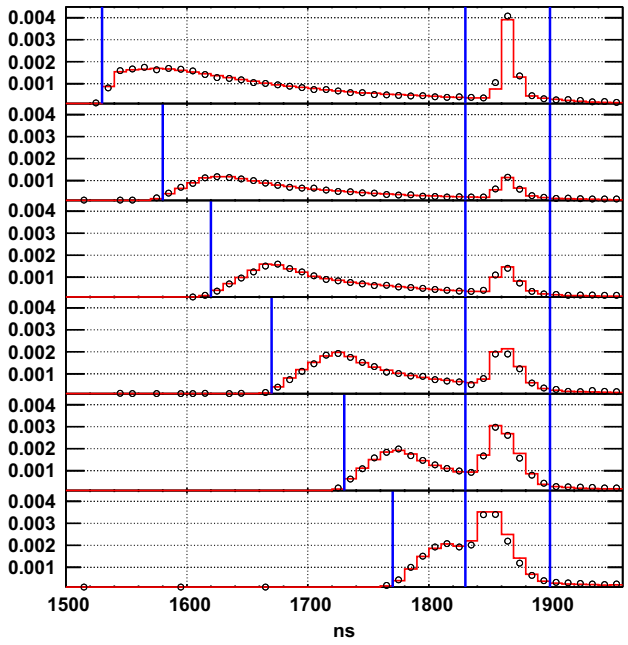

Figure 4.10: The comparison between laser MC and calibration data. Typical Time-Of-Flight-subtracted timing distributions for the vertical down-going laser beam with the wavelength at 405 nm between data (black circle) and MC (red histogram, the best tuned) normalized by observed number of total photoelectrons. The top plot is for the PMTs at the SK tank top wall. The second to the sixth plots correspond to the five barrel wall regions from top to bottom of the SK. Taken from [80]

Ni(n,γ)Ni reaction (9.0 MeV and etc.), ^{137}Cs (0.662 MeV), ^{60}Co (1.33 MeV). Figures 4.15 and 4.16 show the output charge of the Ge detector as a function of γ-ray energy and the difference of the deviation between data and the fitted line. The electron energy measured by the germanium detector is used as input of MC simulation for LINAC calibration. After the LINAC calibration data is taken, the SK simulation is tuned to match the detector response. Figure 4.17 shows the difference of the effective number of hit PMTs, $N_{\rm eff}$, which is defined in Eq. 6.2.4 after tuning MC in SK-IV. The conversion function from $N_{\rm eff}$ to energy is determined by MC simulation of mono-energetic electrons.

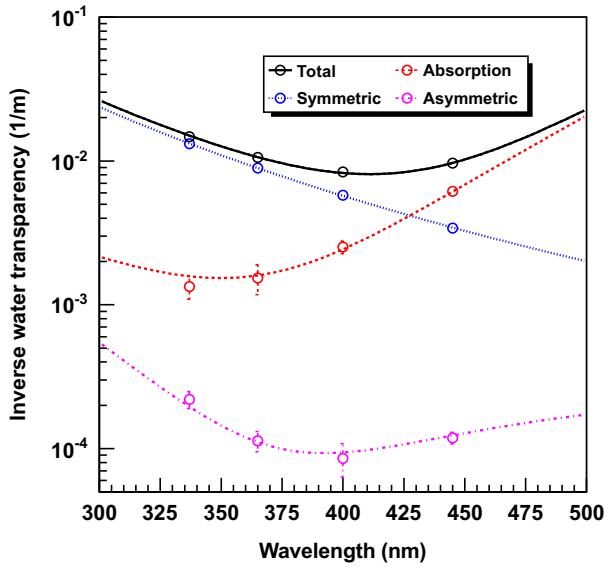

Figure 4.11: Typical fitted water coefficient functions used in the MC. The points are the data obtained in April 2009. Each curves for absorption, symmetric scattering, and asymmetric scattering show the fitted function for each case while the black curve shows the total of all fitted functions added together. Taken from [80]

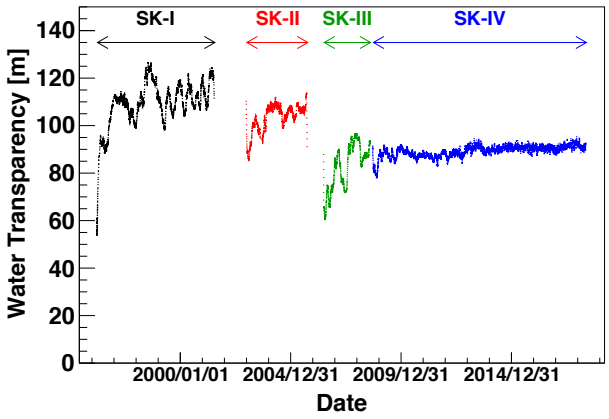

Figure 4.12: Time variation of water transparency. Absolute values are sensitive to the detector configurations and can not be compared among different detector phases.

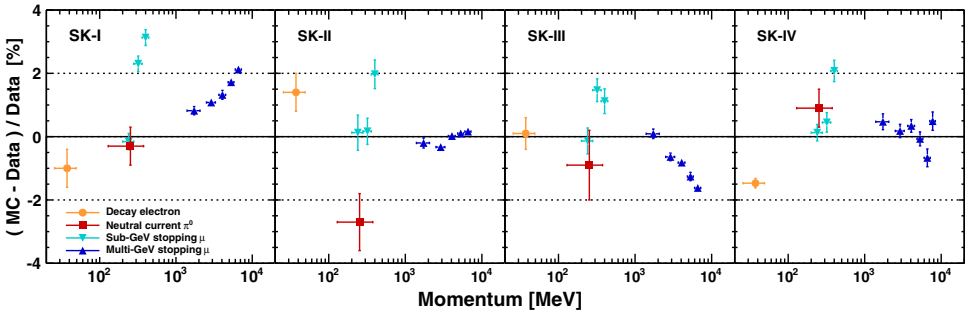

Figure 4.13: Summary of absolute energy scale measurements for each SK phase. The percentage of differences between data and MC are shown. Vertical error bars denote the statistical uncertainty and horizontal error bars denote the momentum range spanned by each analysis. Taken from [82].

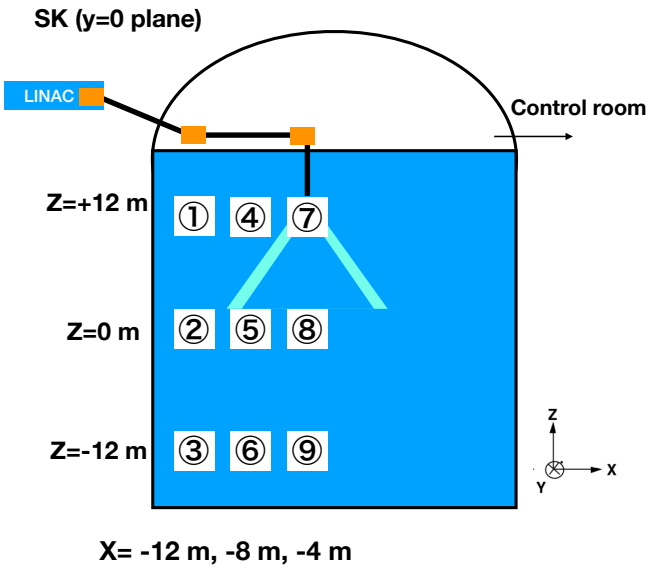

Figure 4.14: A schematic diagram of LINAC calibration system. Orange squares show steering magnets and circled numbers show injection points of mono-energitic electrons. Based on Fig.1 of Ref. [83]

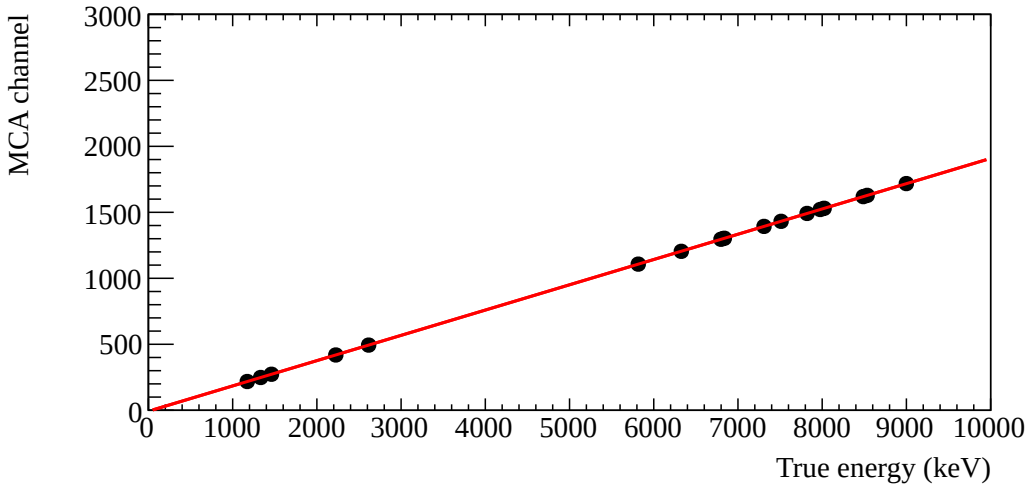

Figure 4.15: The linearity of the germanium detector. The red line shows a linear fuction used for fitting. The vertical axis shows the output from the germanium detector (Multi Channel Analyser channels) and the horizontal axis shows the energy of the calibration γ-ray sources in unit of keV.

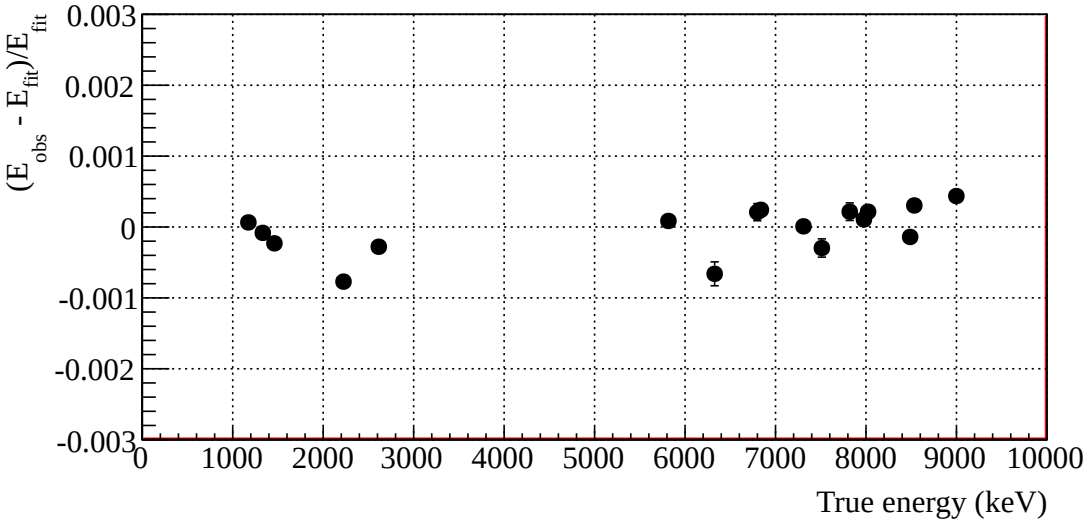

Figure 4.16: The difference between the data and the fitted line in Fig. 4.15. The horizontal axis shows the energy of γ-ray in unit of keV and the vertical axis shows the difference.

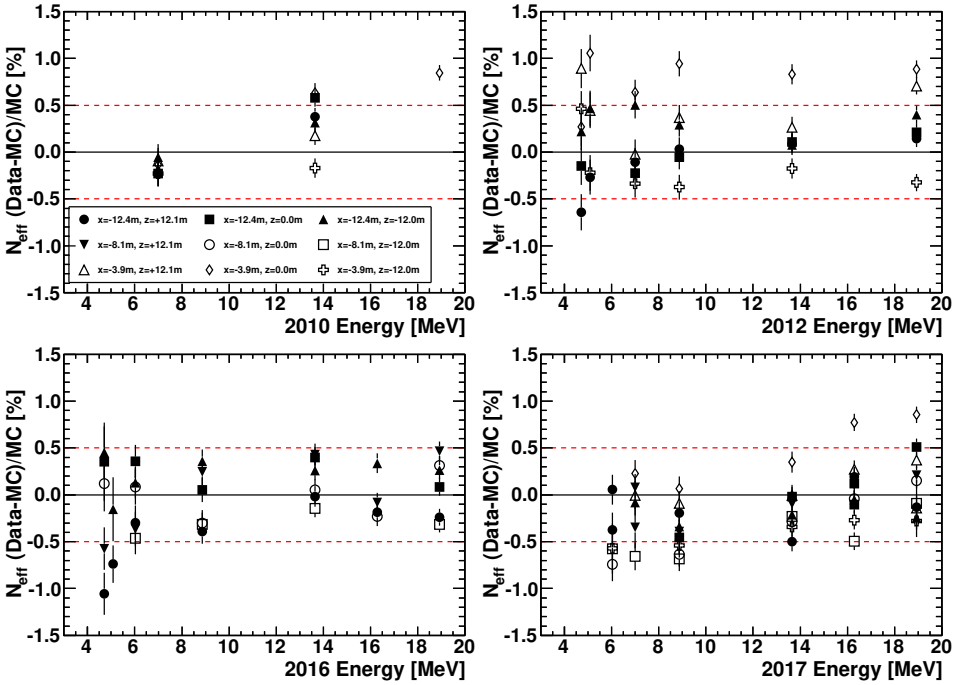

Figure 4.17: The difference of the $N_{\rm eff}$ between the LINAC calibration data and the MC simulation in SK-IV. The markers show the positions of the calibration. The red horizontal lines shows $\pm 0.5\%$.

Chapter 5

Simulation

In this chapter, the Monte Carlo (MC) simulation for solar flare neutrinos in SK is described.

5.1 Neutrino Interactions

For events with neutrino energies above 100 MeV (defined as "high-energy" events as follows), the tools for atmospheric neutrino oscillation analysis were used, and for events with energies below 100 MeV (defined as "low-energy" events as follows), the tools for solar neutrino analysis and supernova neutrino searches were used in this study. More detailed information about data reduction will be described in Chap. 6.

5.1.1 High-Energy neutrino interactions

For High-Energy events, neutrino interactions inside the detector are simulated based on NEUT [84]. They are classified into two categories, Charged Current (CC) and Neutral Current (NC) interactions. A neutrino exchanges a $W^{\pm}$ boson with the target in the CC interaction. After the CC interaction, a charged lepton is left in the final state. By distinguishing the flavor of the charged lepton inside the detector, the flavor of incoming neutrino can be identified. On the other hand, in the NC interaction, a neutrino interacts with the target mediated by a Z^0 boson. After this NC interaction, no signs of the neutrino flavor are left within the detector.

In the NEUT simulation, the following interactions are considered:

- CC and NC (quasi-)elastic scattering. CCQE (NCQE): $\nu + N \rightarrow l(\nu) + N'(N)$.
- CC meson exchange current, CCMEC : $\nu + NN' \rightarrow l + N''N'''$,
- CC and NC single meson production: $\nu + N \rightarrow l(\nu) + N'(N) + \text{meson}$,
- CC and NC coherent pion production, CCCOH (NCCOH): $\nu + {}^{16}\text{O} \rightarrow l(\nu) + {}^{16}\text{O} + \pi$,
- CC and NC deep inelastic scattering, CCDIS (NCDIS): $\nu + N \rightarrow l(\nu) + N'(N) +$ hadrons,

where N,N',N'', and N''' stand for nucleons, l stands for a charged lepton, and ν stands for a neutrino.

Brief explanations for each interaction are described below.

(Quasi-)Elastic Scattering

For the CCQE interaction in NEUT, Llewellyn Smith model [85] is used. The CCQE cross-sections as a function of incoming neutrino energy in NEUT and various experimental results are shown in Fig. 5.1.

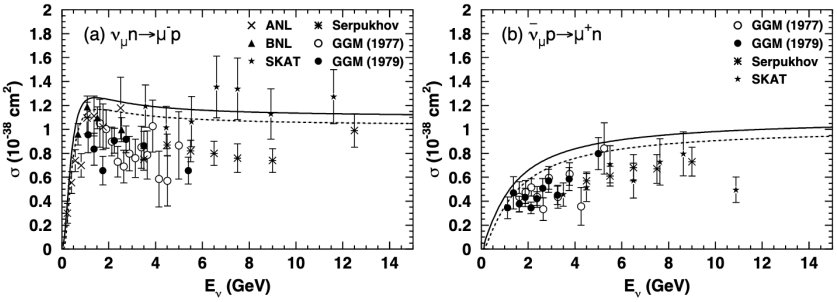

Figure 5.1: Cross-section for the CCQE scattering of muon neutrinos (left panel) and muon anti-neutrinos (right panel). Solid lines show the calculated curves for free targets, and the dashed lines show the calculated bound targets. Experimental data points are from: ANL [86], BNL [87], Gargamelle [88], Serpukhov [89], and SKAT [90]. Taken from [84].

CC meson exchange current

The CCQE interaction is approximated so that the neutrino interacts with a single nucleon only if it ignores the direct correlation between the nucleons in the nucleus. However, it is suggested that a process in which an incoming neutrino interacts with multiple nucleons in the target nucleus simultaneously by MiniBooNE experiment [91]. The Meson Exchange Current (MEC) model by Nieves et al. [92] is adopted in NEUT.

CC and NC single meson production

Single meson production occurs via a baryon resonance excitation state in a neutrino interaction as following:

$$\nu + N \to l(\nu) + N^*, \tag{5.1.1}$$

$$N^* \to N' + \text{meson} \tag{5.1.2}$$

where N^* is the baryon resonance, and a single meson is produced from N^*.

When the invariant mass of the hadron system, W, is less than about 2.0 GeV/c^2, the interactions are dominant hadron production processes. Figure 5.2 shows the cross-sections of single pion production as a function of incoming neutrino energy.

CC and NC coherent pion production

The reaction in which a single pion has the same charge as the incoming weak current can be generated by the interaction between an oxygen nucleus and the neutrino. This interaction is called coherent pion production. Because the momentum transmitted to the oxygen nucleus is

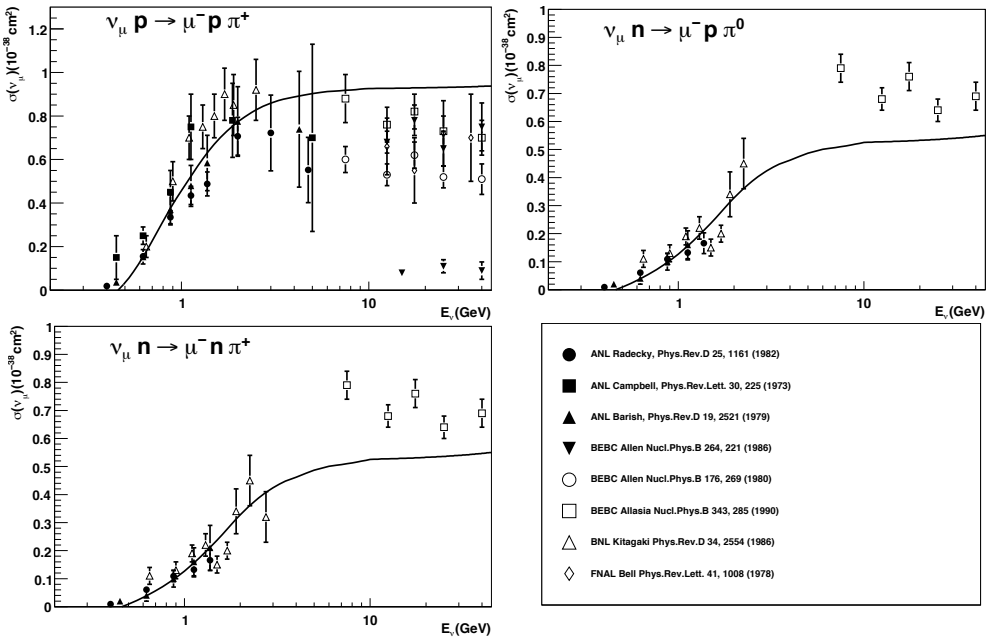

Figure 5.2: Cross-section for single pion production of the muon neutrino. The solid lines show the calculated cross-section. The experimental data are summarized in the bottom right panel [93–100]. Taken from [84]

very small, the angular distribution of the outgoing leptons and pions are peaked in the forward direction. Coherent pion production is simulated based on the Rein and Sehgal model [101].

CC and NC deep inelastic scattering

The interaction of incident neutrinos with the constituent quarks of the target nucleon often generates multiple hadrons via CC deep inelastic scattering (DIS). When the invariant mass of the hadron system, W, is greater than 1.3 GeV/c^2, this process becomes dominant. For interactions with $W < 2.0$ GeV/c^2, only pions are produced as generated hadrons in the final state. Since this hadronic invariant mass region, $W < 2.0$ GeV/c^2, is overlapped with the region for the single pion production interaction, the multiple pion production is simulated as the DIS process.

Figure 5.3 shows the total cross-section of the CC interaction, including CCQE, single meson productions, and DIS.

5.1.2 Low-Energy neutrino interaction

For Low-Energy events, neutrino interactions inside the detector are simulated based on invers-beta-decay (IBD):

$$\bar{\nu_e} + p \rightarrow e^+ + n. \tag{5.1.3}$$

The IBD cross-section is the largest in the energy region of the low-energy sample and can be analytically expressed. Only IBD was considered to obtain a conservative limit because other

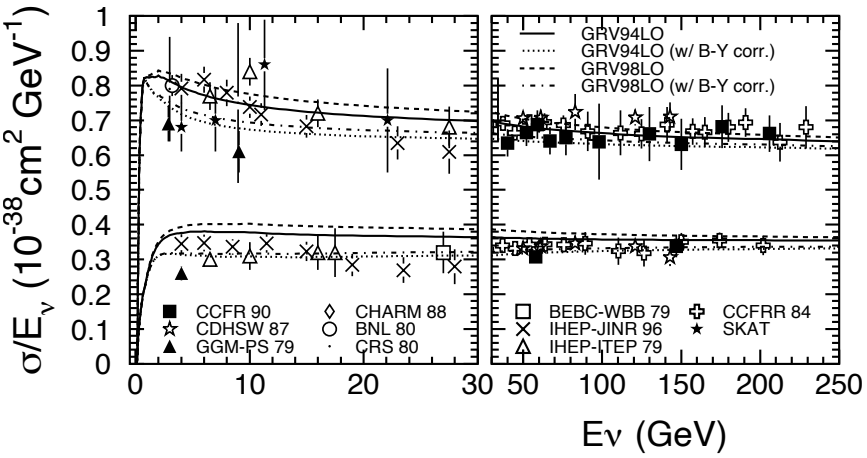

Figure 5.3: Comparison between experimental data and calculated curves of the total cross-sections of the CC interaction for ν and $\bar{\nu}$. The experimental data were taken from CCFR [102], CDHSW [103], GGM-PS [104], CHARM [105], BNL [106], CRS [107], BEBC-WBB [108], IHEP-JINR [109], IHEP-ITEP [110], CCFRR [111], and SKAT [112]. Taken from [84]

interactions are not known precisely, especially about energy and angular distributions of exiting γ-ray emissions. Although only IBD is considered in this thesis, obtained flux limit will be conservative. In this study, Strumia and Vissani's model [113] is used for the IBD cross-section as shown in Fig. 5.4.

5.2 SK Detector Simulation

The secondary particles produced by NEUT are propagated in the SK detector simulation using a GEANT3 based simulation called SKDETSIM. Interactions of the particles in water, particle decays, and production of Cherenkov photons are simulated in SKDETSIM. Detector responses including the water property, optical modeling as well as PMT and electronics responses to the produced photons are simulated based on the detector calibration results (See Chap. 4). The opening angle of the Cherenkov ring is calculated using Eq. 2.1.1. For the propagation of charged particles, the number of Cherenkov photons and their wavelengths are calculated using Eq. 2.1.4.

Cherenkov photons produced by the charged particles can be scattered or absorbed in water. The probability of either of these processes occurring is characterized by parameters that depend on the transparency of the water, which is also based on the detector calibration results. When the Cherenkov photons arrive at the wall of the tank, reflections on the surface can occur. The calculated reflection value, including the polarization, is used for the SKDETSIM.

SK is an experiment that spans 20 years, and the detector conditions have fluctuated somewhat. Short-term fluctuations include water transparency fluctuations and long-term fluctuations include increased gain in PMT. In order to incorporate these changes into the simulation, a time-dependent detector simulation has been introduced in SKDETSIM.

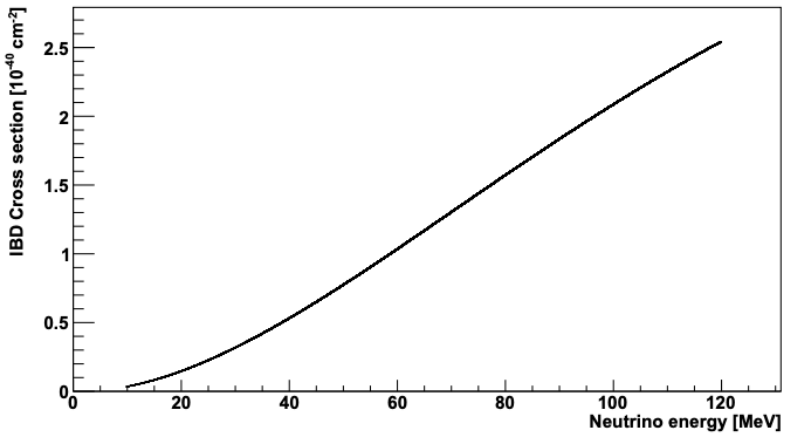

Figure 5.4: IBD cross-section on a free proton as a function of neutrino energy as calculated by Strumia and Vissani [113].

5.3 Solar Flare Neutrino Flux

The generation processes of solar flare neutrinos in theoretical models are described in Chap. 1. The assumptions of the total energy of the solar flare neutrinos and the solar atmosphere model are different in each model, and the flux predictions of the solar flare neutrinos reaching the earth in each model are derived by the Monte Carlo simulation. The neutrino energy spectrum from the solar flare neutrino model was used as input to simulate the solar flare neutrino signal. For the high-energy MC sample, the expected visible energy spectrum of solar flare neutrinos is obtained based on the atmospheric neutrino simulations using a re-weighting method. In the re-weighting method, the result is obtained by re-weighting each simulated event with the ratio of the actual neutrino energy spectrum of solar flares and that of atmospheric neutrinos. The energy spectra thus obtained for various solar flare simulations are shown in Fig. 5.5 and 5.6.

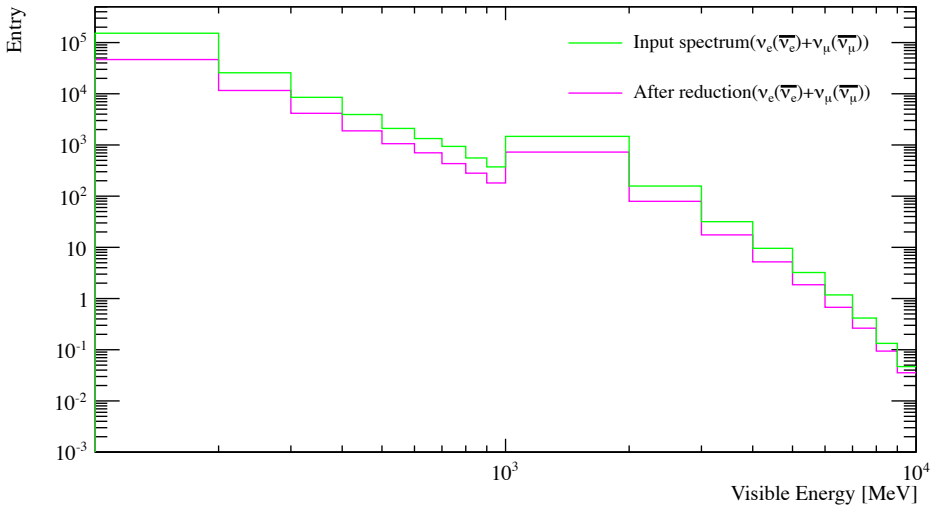

Figure 5.5: The energy spectra of solar flare neutrino from Fargion and Moscat [42]. The horizontal axis is reconstructed positron kinetic energy and the vertical axis shows the number of events. The yellow-green histograms represent the energy spectrum of the generated events, and the magenta histograms represent the energy spectrum after the reduction (See Chap. 6) is applied.

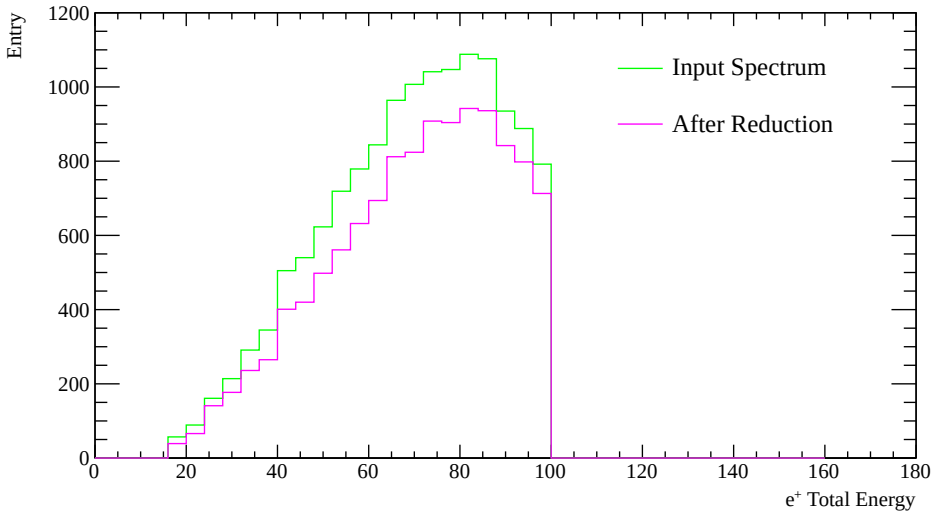

Figure 5.6: The energy spectra of solar flare neutrinos from Fargion and Moscat [42]. The horizontal axis is the visible energy in SK and the vertical axis shows the number of events. The yellow-green histograms represent the energy spectrum of the generated events, and the magenta histograms represent the energy spectrum after the reduction (See Chap. 6) is applied.

Chapter 6

SK Data Analysis

In this chapter, a method to search for events in the Super-Kamiokande detector is described. Solar flare neutrinos are considered to have energies ranging from several MeV to several GeV. For events with energies above 100 MeV (defined as "high-energy" events hereafter), the tools for the atmospheric neutrino oscillation analysis were used, and for events with energies below 100 MeV (defined as "low-energy" events hereafter), the tools for the solar neutrino analysis and the supernova neutrino search were used in this study. The data sets obtained by those tools are described below.

6.1 High-Energy Event Analysis

The atmospheric neutrino events observed in Super-Kamiokande can be classified into several types, as shown in Fig. 6.1. If a neutrino interacts in the inner detector (ID) and producted charged particles lose all their energy in ID, the event is called a fully contained (FC) event. If a neutrino interacts in ID and deposits energy both in the inner and outer detectors, the event is called a Partially Contained (PC) event. When a muon-neutrino interacts with the rock in the vicinity of the detector, the generated muon enters from the outer detector (OD) and emit Cherenkov light in OD and ID. Downward-incident events are not used in the analysis because it is difficult to distinguish them from cosmic-ray muon backgrounds, but upward-incident events are used in the analysis of neutrino oscillations because they are mainly induced by neutrino interactions. They are called upward-going muons (UPMU).

In this study, we analyzed only the FC data sample, since the energy of solar flare neutrinos peaks around 70 MeV, and the track of the charged particles is usually contained in ID. The event selection method for the FC sample is described below.

6.1.1 First Reduction

The number of triggered events in a day is about 10^6 events/day, most of which are due to downward cosmic ray muons and low-energy radioactive events. To remove such background, the following conditions are given as the first step of the FC event selection.

- $PE_{300} > 200$ p.e.'s : The PE_{300}, the total number of photoelectrons observed in ID within 300 ns, is greater than 200 photoelectrons (p.e.'s).
- $NHITA_{800} < 55$: Number of OD hits within a range of ± 400 ns around the event trigger, $NHITA_{800}$, is less than 55.

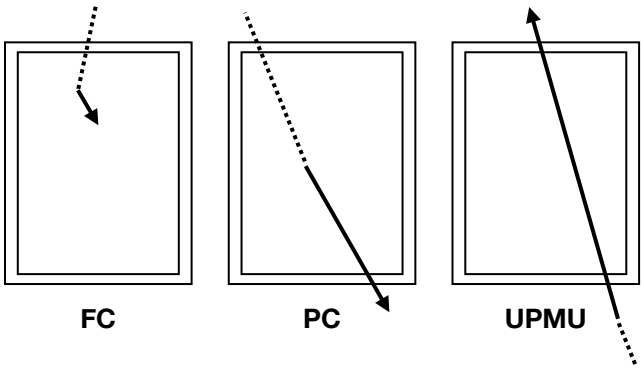

Figure 6.1: Three types of high-energy events at SK. The solid arrows show charged particles and dashed lines show neutrinos.

The first condition corresponds to a threshold of about 22MeV/c for the electron momentum, which cuts out most low-energy events such as radiation background. The second condition is to cut out cosmic ray muons that come into the detector.

6.1.2 Second Reduction

In the second stage of the FC event selection, the following conditions are given.

- $PE_{max}/PE_{300} < 0.5$: The ratio of the largest number of photoelectrons among all hit ID PMTs, PE_{max}, to the total number of photoelectrons PE_{300} is less than 0.5.
- $NHITA_{800} < 25$ (30 for SK-IV) or $PE_{tot} > 100,000$ p.e.'s (50,000 p.e.'s for SK-II) : $NHITA_{800}$ is less than 25 (30 for SK-IV) or total number of photoelectrons in the inner tank PE_{tot} is more than 100,000 photoelectrons (50,000 photoelectrons for SK-II).

The first condition cuts out events where one PMT has an extremely large signal compared to the surrounding PMTs due to electrical noises in the PMTs, and the second condition further cuts out events such as cosmic ray muons left over from the first event selection.

6.1.3 Third Reduction

A third reduction comprises of several cuts optimized to reduce various types of muons, flasher events, low energy radioactive events, and electric noise events.

Through-going Muon Cut

A high energy cosmic-ray muon that passes through ID is called a through-going muon. To eliminate these events, a through-going muon fitter is applied if an event that PE_{max} is greater than 231 p.e.'s and number of ID PMT hits is more than 1000 hits. The fitter finds them by

maximizing the following goodness

$$\text{goodness} = \frac{1}{\sum_i \frac{1}{\sigma_i^2}} \times \sum_i \frac{1}{\sigma_i^2} \exp\left(-\frac{({t'}_i - t_0)}{2 \times (\sigma_i \times 1.5)^2}\right), \tag{6.1.1}$$

where σ_i is the timing resolution of i-th PMT, ${t'}_i$ is the i-th PMT's time-of-flight corrected residual time and t_0 is chosen so that the goodness is maximal at each tested entering and exiting point. The event rejection criteria are as follows:

- goodness > 0.75 : The goodness greater than 0.75.
- $\text{NHITA}_{\text{in}} > 10$ or $\text{NHITA}_{\text{out}} > 10$: NHITA_{in} ($\text{NHITA}_{\text{out}}$) is the number of OD PMT hits located within 8 m from the reconstructed entering (exiting) point in a fixed 800 nsec timing window.

When those criteria are met, the event is rejected as a through-going muon.

Stopping Muon Cut

Stopping muons are cosmic-ray muons that stop inside ID. In a similar manner to through-going muons, a special stopping muon fitter identifies a cluster of earliest timing ID PMT hits as a muon entering point from those PMT's position, and the fitting goodness is evaluated using Eq. 6.1.1. The criteria to reject those events are following:

- goodness > 0 : The stopping muon fit is succeeded, the goodness is greater than 0.
- $\text{NHITA}_{\text{in}} > 10$: If NHITA_{in} is greater than than 10.

When those criteria are met, the event is rejected as a stopping muon.

Cable Hole Muon Cut

There are cable holes on the top of the SK tank to supply HV on PMTs and take PMT signals. The cosmic-ray muons that enter through cable holes are removed using the veto counters, as shown in Fig. 6.2. When one of the veto counters hit and the distance between the cable hole and the reconstructed vertex is less than 4 m, the event is rejected.

Low Energy Event Cut

In order to reject low energy events in the high-energy analysis, the following rejection criteria are applied:

- NHIT < 500 : The number of ID PMT hits (NHIT) is less than 500.
- $\text{N}_{50} < 50$ ($\text{N}_{50} < 25$ for SK-II) : N_{50} is the maximum number of ID PMT hits in a sliding 50 nsec window after subtracting the photon time-of-flight. The vertex position used for the time-of-flight subtraction is reconstructed with a dedicated low energy event fitter.

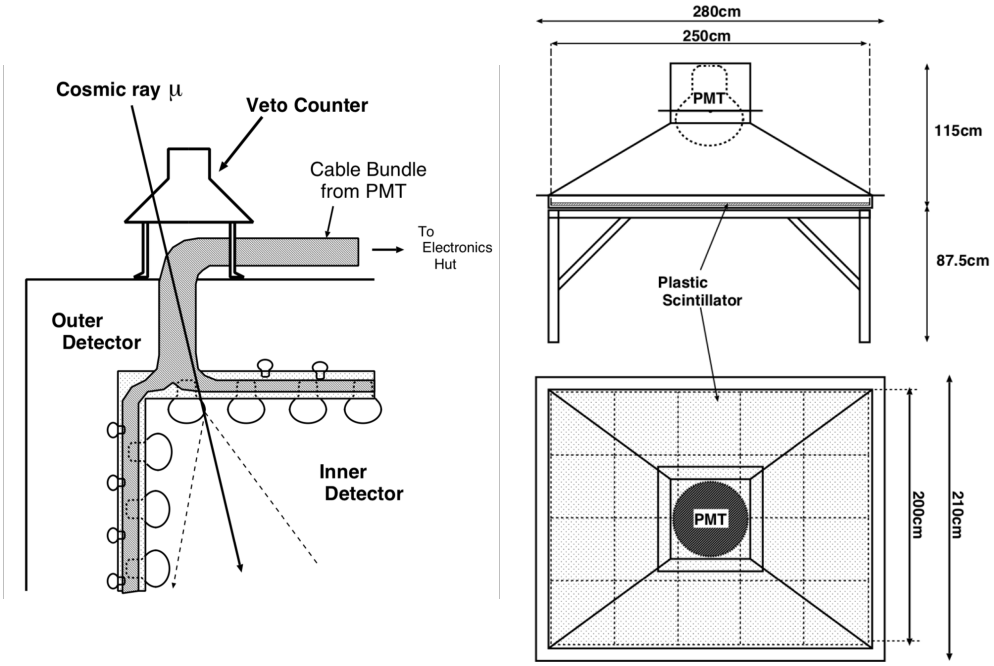

Figure 6.2: The schematic view of the cable hole and the veto counter. Plastic scintillation counters are used as veto counters for four large cable holes.

Flasher Event Cut

Flasher events often have a broad timing distribution compared to events produced by charged particles. The flasher event rejection criteria are as follows:

- $\mathrm{NHIT}_{\mathrm{min},100} > 15$ (For SK-I) : $\mathrm{NHIT}_{\mathrm{min},100}$ is the minimum number of ID PMT hits in a sliding 100 nsec timing window from +300 nsec to +800 nsec after the trigger timing.
- NHIT < 800 and $\mathrm{NHIT}_{\mathrm{min},100} > 10$ (For SK-II to SK-IV) : NHIT is the number of ID PMT hits.

Accidental Coincidence Event Cut

A cosmic-ray muon and low energy activities sometimes accidentally coincide. In case the cosmic-ray muon comes in the detector several hundred nsec after the low energy activity, the event trigger is issued by the low energy activity, and no obvious OD PMT hits are found around the trigger timing. The event rejection criteria are as follows to prevent them from contaminating the data set:

- $\mathrm{PE}_{\mathrm{LATE}} > 5,000$ p.e.'s ($\mathrm{PE}_{\mathrm{LATE}} > 2,500$ p.e.'s for SK-II) : $\mathrm{PE}_{\mathrm{LATE}}$ is the total number of photoelectrons in ID within a fixed 500 nsec timing window from +300 nsec to +800 nsec after the trigger timing.

- $\mathrm{NHITA_{LATE}} > 20$: $\mathrm{NHITA_{LATE}}$ is the number of OD PMT hits within a fixed 500 nsec timing window from +300 nsec to +800 nsec after the trigger timing.

6.1.4 Fourth Reduction

To remove remaining flasher events, an intelligent pattern matching algorithm is applied. The flasher events usually repeat with similar hit patterns, because the flasher events occur when a light is emitted from a flasher PMT. The algorithm tries to find if two different events in which PMT hit patterns are similar or not. The procedure of the algorithm of the pattern matching is as follows:

- Divide ID wall into 1,450 patches of a 2 $\times$ 2 m square.
- Calculate the correlation factor r by comparing the total charge in each patch of two events, A and B. The correlation is defined as:

$$r = \frac{1}{N}\sum_i \frac{(Q_i^{\mathrm{A}} - \langle Q^{\mathrm{A}}\rangle) \times (Q_i^{\mathrm{B}} - \langle Q^{\mathrm{B}}\rangle)}{\sigma^{\mathrm{A}} \times \sigma^{\mathrm{B}}}, \tag{6.1.2}$$

  where N is the number of patches, Q_i^{A} (Q_i^{B}) is the ith patch's total observed charge in event A (B), $\langle Q^{\mathrm{A}}\rangle$ ($\langle Q^{\mathrm{B}}\rangle$) is the average charge over all patches in event A (B), σ^{A} (σ^{B}) is is the standard deviation of the observed charge in event A (B).
- Calculate the distance ($\mathrm{DIST_{max}}$) between the PMTs with the maximum pulse heights in the two compared events.
- If $\mathrm{DIST_{max}}$ is less than 75 cm, an offset value (0.15) is added to r.
- If r exceeds a threshold (r_{thr}), events A and B are recognized as matched. The r_{thr} is defined as

$$r_{\mathrm{thr}} = 0.168 \times \log\left(\frac{\mathrm{PE}_{300}^{A} + \mathrm{PE}_{300}^{B}}{2}\right) + 0.13, \tag{6.1.3}$$

  where $\mathrm{PE_{300}}$ is the total number of photoelectrons observed in ID within 300 nsec.
- Repeat the above calculation over 10,000 events around the target event and count the number of matched events.
- Remove the events with large r, or a large number of matched events.

6.1.5 Fifth Reduction

The fifth reduction is designed to remove still remaining cosmic ray muons and flasher events.

Stopping Muon Cut

The remaining stopping muons are rejected more tightly than that of the third reduction. The goodness which is defined by Eq.6.1.1 and $\mathrm{NHITA_{in}}$, the number of OD PMT hits located within 8 m from the reconstructed entering point, are used again. The criteria follows:

- *goodness* ≥ 0.5 and $\mathrm{NHITA_{in}} \geq 5$: This is a tighter criteria condition than that of in the third reduction.

Invisible Muon Cut

If the momentum of cosmic ray muon is too low to generate Cherenkov light, it can not be detected. They are called an invisible muon. A cluster of OD PMT hits, which are produced earlier than the ID trigger timing and are induced by the muon before its decay, are often found in such events. Events satisfying at least one of the following criteria are rejected as invisible muon events:

- $\mathrm{PE}_{tot} < 1,000$ p.e.'s (500 p.e.'s for SK-II) and $\mathrm{NHITA}_{\mathrm{early},200} \geq 5$ and $\mathrm{NHITA}_{\mathrm{sum}} \geq 10$: PE_{tot} is the total ID PMT charge and $\mathrm{NHITA}_{\mathrm{early},200}$ is the maximum number of OD PMT hits in a sliding 200 nsec timing window from -9000 nsec to -200 nsec from the trigger timing. $\mathrm{NHITA}_{\mathrm{sum}}$ is defined as following:

$$\mathrm{NHITA}_{\mathrm{sum}} = \begin{cases} \mathrm{NHITA}_{\mathrm{early},200} + \mathrm{NHITA}_{500}(d_{\mathrm{OD}} < 500cm) \\ \mathrm{NHITA}_{\mathrm{early},200} + \mathrm{NHITA}_{500}(\mathrm{otherwise}) \end{cases} \tag{6.1.4}$$

  where NHITA_{500} is the number of OD PMT hits in a fixed 500 nsec timing window from -200 nsec to $+300$ nsec from the trigger timing, and d_{OD} is the distance between the position of the OD PMT hit cluster in $\mathrm{NHITA}_{\mathrm{early},200}$ and the position of the OD PMT hit cluster in NHITA_{500}.

Flasher Event Cut

In order to further reject flasher events, there are flasher rejection criteria at the fifth reduction step. The goodness-of-vertex fit and the variable described in the third reduction NMIN_{100} are used. The criteria are as follows:

- goodness-of-vertex < 0.4 and $\mathrm{NHIT}_{\mathrm{min},100} > 6$: The goodness-of-vertex fit is described in Sec. 6.1.7.

6.1.6 Final Sample Selection

After five reduction steps, the neutrino events that satisfy the following three criteria are finally selected in this study.

- The number of hit PMTs in the largest OD hit cluster (NHITAC) is less than 16 (10 for SK-I).
- The reconstructed vertex (d_{wall}) of neutrino interaction is located at more than 200 cm away from the ID wall.
- The visible energy (E_{vis}) obtained from the reconstruction algorithm should be greater 100 MeV for an electron.

The overall efficiency of the FC sample selections for the true neutrino events is estimated by the signal MC as shown in Tab. 6.1.6. Here, we use atmospheric neutrino MC events for the signal efficiency estimation. The background contamination i.e. non-neutrino events in the final sample is estimated to be about 0.1% based on the eye-scant of the selected events.

In addition to this, the search time window which is described in Chap. 3 is applied to search neutrinos associated with solar flares.

Table 6.1: Reduction efficiency after each FC reduction step calculated by the signal MC.

Efficiency	SK-I	SK-II	SK-III	SK-IV
1st Reduction	100.0	99.96	100.0	100.0
2nd Reduction	100.0	99.90	99.98	99.99
3rd Reduction	99.91	99.97	99.81	99.83
4th Reduction	99.51	99.51	99.68	99.00
5th Reduction	99.47	99.43	99.62	98.85

6.1.7 Event Reconstruction

Event information can be obtained by the reconstruction of the Cherenkov light cones in SK. In this section, the event reconstruction method of high-energy event is briefly described. A detailed explanation of the reconstruction can be found in Shiozawa et. al [114].

Vertex Reconstruction

The vertex reconstruction algorithm consists of three steps, point-fit, ring edge finding, and TDC-fit. Since this step is prior to the ring counting algorithm described later, the following calculation assumes a single-ring event and focuses on the most energetic ring. An initial vertex position is estimated by maximizing the following estimator (G), assuming all photons are emitted at the same time and position:

$$G = \frac{1}{N}\sum_i \frac{1}{\sigma_i^2}\exp\left(-\frac{({t'}_i - t_0)^2}{2(\langle\sigma\rangle \times 1.5)^2}\right), \tag{6.1.5}$$

where N is the number of hit PMTs, $\langle\sigma\rangle$ is fixed to 2.5 nsec here, and ${t'}_i$ is the i-th PMT's time-of-flight subtracted residual time for an assumed vertex position. The vertex fitter searches for a vertex position where the estimator G takes the maximum value.

The direction and the outer edge of the dominant ring are measured in the second step. A pair consisting of the direction and the opening angle, $Q(\theta_{\rm edge})$, is tested by a parameter as follows:

$$Q(\theta_{\rm edge}) = \frac{\int_0^{\theta_{\rm edge}} {\rm PE}(\theta){\rm d}\theta}{\sin(\theta_{\rm edge})} \times \left(\frac{{\rm dPE}(\theta)}{{\rm d}\theta}_{\theta=\theta_{\rm edge}}\right)^2 \times \exp\left(\frac{(\theta_{\rm edge}-\theta_{\rm exp})^2}{2\sigma_\theta^2}\right), \tag{6.1.6}$$

where $\theta_{\rm exp}$ and σ_θ are the Cherenkov opening angle expected from the charge within the cone and its resolution. ${\rm PE}(\theta)$ is the angular distribution of the observed charge as a function of opening angle θ from the particle direction. For the first factor, the numerator of the first element favors more of the charge in the reconstructed ring and the denominator is enhanced against the narrower ring. The middle factor favors sharper rings and the last factor enhances the estimator if it is close to the expectation. The direction and the ring edge position are determined to maximize the estimator. The vertex position is then determined using TDC-fit, wherein track length of a charged particle and the scattering are taken into account. The time residuals for PMTs inside and outside the Cherenkov ring are calculated, and the goodness of the algorithm proceeds step by step, and the later reconstruction steps use results obtained in the former steps.

Ring Counting

When the vertex and the first Cherenkov ring are found, the ring counting algorithm is applied to search for other such rings in the event. Other rings are searched for using an algorithm with a Hough transformation and the likelihood technique. Figure 6.3 shows the illustration of the method. The dashed circles centered at each hit PMT are drawn with 42°. The direction of the Cherenkov ring is identified as the intersection point of those dashed circles. By selecting the ring direction using this method, the second and subsequent ring candidates are searched for. The likelihood method is used to determine whether a candidate ring is consistent with ring properties.

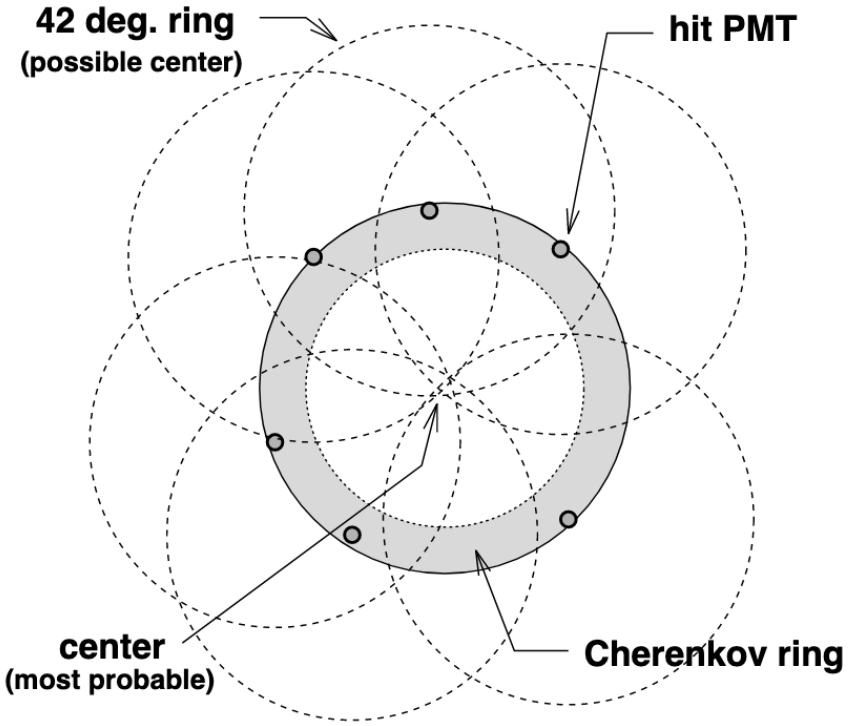

Figure 6.3: Basic idea of finding ring candidates. The shaded ring represents the Cherenkov ring image, and the dashed circles are virtual Cherenkov rings centered at each PMT hit. The overlapping point is to be the center of the real Cherenkov ring.

When N rings are found for an event, we test whether the $(N+1)$-th ring candidate is true

using the likelihood. The likelihood function is defined as

$$\mathcal{L} = \sum_i \log\left(\mathrm{prob}(q_i^{\mathrm{obs}}, \sum_{n=1}^{N+1} \alpha_n \cdot q_{i,n}^{\mathrm{exp}})\right), \tag{6.1.7}$$

$$\mathrm{prob}(q^{\mathrm{obs}}, q^{\mathrm{exp}}) = \begin{cases} \frac{1}{\sqrt{2}} \exp\left(-\frac{(q^{\mathrm{obs}} - q^{\mathrm{exp}})^2}{2\sigma}\right) & (q^{\mathrm{exp}} > 20 \text{ p.e.}) \\ \text{Single p.e. and Poisson convolution } (q^{\mathrm{exp}} \leq 20 \text{ p.e.}), \end{cases} \tag{6.1.8}$$

where hit PMTs inside N + 1 Cherenkov rings are summed. q^{obs} is the observed p.e. in the i-th PMT, $\alpha_n \cdot q_{i,n}^{\mathrm{exp}}$ is the expected p.e. at the i-th PMT from the nth ring, σ is the resolution for q^{exp}, and the probability function determines how well the expected charge reproduces the charge observed in the i-th PMT. The likelihood is maximized by varying the α_n factors with a lower momentum constraint.

6.2 Low-Energy Event Analysis

The lowest threshold for the Super-Kamiokande detector analysis is 3.5 MeV, but in the neutrino energy region below 14.06 MeV, the steady-state ^{8}B neutrinos are dominant. Therefore the energy region to be analyzed is above 16 MeV for the solar flare neutrino search. For low-energy events, the vertex of the event is reconstructed from the hit timing of each PMT, the direction of the event from the hit pattern of the PMTs, and the energy is reconstructed from the parameters obtained from the calibration of the detector and used in the reduction processes.

6.2.1 Event Reconstruction

Vertex Reconstruction

The hit timing of each PMT is used to reconstruct the vertex. The maximum distance that a charged particle with an energy of less than 100 MeV can travel in pure water is about 50 cm, which is small compared to the positional resolution. Therefore, the track of charged particles is assumed to be point-like. The maximum likelihood method is used to reconstruct the vertex position, and the likelihood function is defined as follows.

$$\mathcal{L}(\boldsymbol{v}, \Delta t_i) \equiv \sum_{i=1}^{N_{\mathrm{hit}}} \log(P(\Delta t_i(\boldsymbol{v}))), \tag{6.2.1}$$

where Δt_i is defined using TOF corrected residual time of the i-th PMT ($t_{\mathrm{res,i}}$) and time of occurrence of the event (t_0) as

$$\Delta t_i \equiv t_{\mathrm{res},i} - t_0. \tag{6.2.2}$$

$P(\Delta t_i(\boldsymbol{v}))$ is the probability density function of Δt_i and it is determined by the LINAC calibration. Vertex position reconstruction is done by maximizing the likelihood function in an event reconstruction program called BONSAI (Branch Optimization Naviating Successive Annealing Iterations).

Direction Reconstruction

Since Cherenkov light photons create a ring pattern of events, it is possible to determine the direction of the events. The direction reconstruction, the maximum likelihood method is used, and the likelihood function is defined as follows:

$$\mathcal{L}(\boldsymbol{d}) \equiv \sum_{i=1}^{N_{20}} \log(f(\cos\theta_i, E)) \times \frac{\cos\theta_i}{a(\theta_i)}, \tag{6.2.3}$$

where θ_i is the angle of incidence of a photon to the i-th PMT as shown in Fig. 6.4, N_{20} is the maximum number of ID PMT hits in a sliding 20 nsec window after subtracting the photon time-of-flight and $f(\cos\theta_i, E)$ is the distribution function of the angle between the direction of the charged particle and the direction of the observed photon from the vertex. The $\cos(\theta_i)/a(\theta_i)$ term is a correction term for the acceptance of the i-th PMT as shown in Fig. 6.5.

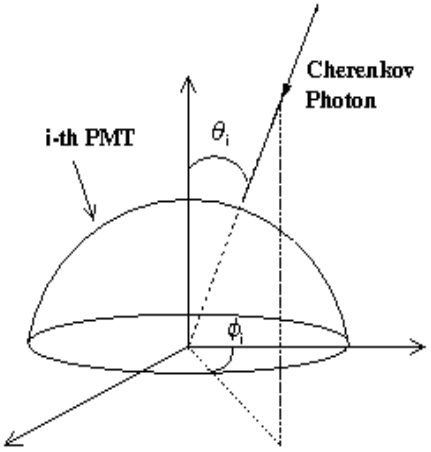

Figure 6.4: Definition of θ_i and ϕ_i. Taken from [115]

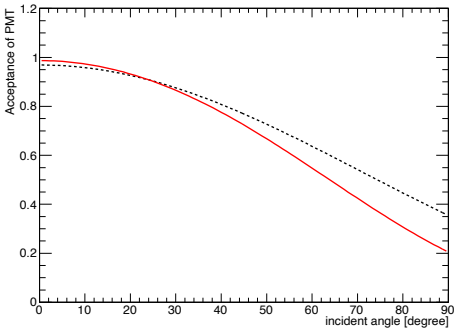

Figure 6.5: Angular dependence of acceptance of PMT ($a(\theta_i)$). Taken from [116]. The black line is for PMT only (SK-I). The red line indicates the case with shock wave protection (SK-II and later).

Energy Reconstruction

Since the number of emitted Cherenkov photons is essentially proportional to the energy of the charged particles, the energy of the charged particles can be estimated from the observed number of photons. However, for low-energy events, the number of PMTs which detected photons, called "hit PMTs" hereafter, is used to reconstruct the energy instead of the total number of photons. The reason for using the number of hit PMTs is as follows.

- The number of photons emitted in low-energy events is small, and the average number of photoelectrons in each PMT is mostly one.
- The resolution of one photoelectron of PMT is not good.

The number of PMT hits depends on the vertex position and the direction of an event, the transparency of the water, and the quantum efficiency of each PMT. The number of effective

hits, $N_{\rm eff}$, is calculated by making the following corrections to the hit PMTs of N_{50} which is the maximum number of ID PMT hits in a sliding 50 nsec window.

$$N_{\rm eff} = \sum_{i=1}^{N_{50}} \left[(X_i + \varepsilon_{\rm tail} - \varepsilon_{\rm dark}) \times \frac{N_{\rm all}}{N_{\rm alive}} \times \frac{R_{\rm cover}}{S(\theta_i, \phi_i)} \times \exp(r_i/\lambda) \times G(i) \right] \tag{6.2.4}$$

where X_i is the multiple hit correction, $\varepsilon_{\rm tail}$ is the delayed hit correction, $\varepsilon_{\rm dark}$ is the dark noise correction, $N_{\rm all}$ is the number of ID PMTs in SK, $N_{\rm alive}$ is the number of non bad PMTs, $R_{\rm cover}$ is the coverage of ID PMTs, the effective area of the i-th PMT's photocathode from view of the direction of photon incidence, the $\exp(r_i/\lambda)$ term is water transparency correction term and $G(i)$ is the quantum efficiency correction term. From the above corrections, $N_{\rm eff}$ is determined. The conversion function from $N_{\rm eff}$ to energy is determined by Monte Carlo simulation of mono-energitic electrons.

6.2.2 First Reduction

The 1st reduction is used to remove typical detector-derived noises and cosmic ray events. The cutting criteria are as follows.

First of all, events with Low Energy (LE) triggers are selected for low-energy sample. In addition, we remove events most likely due to muons by vetoing OD triggers or events with a charge deposition larger than 1000 p.e.'s.

Some well-reconstructed events in FV can be electrons from muon decays or charged particles from showers associated with cosmic muons induced spallation events. To remove these events, low-energy events occuring less than 50 μsec after a muon are rejected. There are many background events coming from the wall. To remove these, the fiducial volume (FV) cut is applied, which selects only events more than 200 cm away from the ID wall.

We then apply quality cuts to the remaining events by requiring the goodness of the vertex fit as defined in Eq. 6.2.6, which is called *bsgoodness*, and the azimuthal isotropy of the reconstructed ring as defined in Eq. 6.2.7, $bsdirKS$, to verify

$$bsgoodness > 0.5 \text{ and } Ovaq = bsgoodness^2 - bsdirKS^2 > 0.25. \tag{6.2.5}$$

Definition of *bsgoodness* is as follows:

$$bsgoodness = \frac{\sum_i \exp(\frac{(t_{{\rm res},i}-t_0)^2}{2w^2}) \exp(\frac{(t_{{\rm res},i}-t_0)^2}{2\sigma^2})}{\sum_i \exp(\frac{(t_{{\rm res},i}-t_0)^2}{2w^2})}, \tag{6.2.6}$$

where $t_{{\rm res},i}$ is the i-th PMT's hit time after subtracting the time of flight, and t_0 is the fit peak time of $t_{{\rm res},i}$ distribution,w is the RMS of the $t_{{\rm res},i}$ distribution and σ is the timing resolution of the PMTs.

Another parameter, $bsdirKS$, is defined as

$$bsdirKS = \frac{\max(A_{{\rm uniform},i} - A_{{\rm data},i}) - \min(A_{{\rm uniform},i} - A_{{\rm data},i})}{2\pi}, \tag{6.2.7}$$

where $A_{{\rm uniform},i}$ is the azimuthal angle of the i-th hit PMT, assuming that the hit PMTs are uniformly distributed along a Cherenkov cone. $A_{{\rm data},i}$ is that of the observed azimuthal angle of the i-th hit PMT.

6.2.3 Second Reduction

Since only half of the spallation background events are removed in the first reduction, a more in-depth study of the correlations between muons and low-energy events is necessary. We therefore pair each low-energy event that passes the first reduction with all muons up to 30 sec before and after the low-energy event and, for each of these pairs, compute the following observables. The former and the latter are called pre sample and post sample, respectively.

variables

dt: time difference between the muon and the low-energy event.

l_{t}: Transverse distance of the low-energy event to the muon track.

l_{l}: Longitudinal distance to the point of the muon track associated with the maximal energy deposition.

muqismsk: Total charge deposited by the muon in the detector. This directly reflects how likely oxygen nuclei are broken up by the muon track.

resQ: Residual charge deposited by a muon compared to the value expected from the minimum ionization. This observable can be expressed as

$$\mathrm{resQ} = \mathrm{muqismsk} - q_{\mathrm{MI}} \cdot L \tag{6.2.8}$$

where q_{MI} and L are the number of photoelectrons per centimeter expected from the minimum ionization and the track length, respectively. For muons with multiple tracks, L is the sum of the lengths of all tracks. This observable is not associated to an event pair but allows to determine how likely a given muon is to induce a shower.

In order to discriminate the spallation events from the random events more effectively, a likelihood is calculated from the spallation variables. For this, two probability density functions (PDFs), the spallation PDF (PDF_{spall}) and the random PDF (PDF_{random}), are prepared for each discriminating variable $i(= dt, lt, ll, muqismsk, resQ)$.The post sample distribution is subtracted from the pre sample distribution and the resulting distribution is area-normalized to produce PDF^i_{spall}. The post sample distributions are area-normalized to produce PDF^i_{random}. The ratios of PDF^i_{spall} to PDF^i_{random} are multiplied to each other to make spallation likelihood ($\mathcal{L}_{spall}$) as:

$$\mathcal{L}_{spall} = \log(\prod_i \frac{PDF^i_{\mathrm{spall}}}{PDF^i_{\mathrm{random}}}) \tag{6.2.9}$$

The cut points are determined by the shape of likelihood distributions as shown in Fig. 6.6.

6.2.4 Third Reduction

The low energy end of the search energy window is contaminated by radioactivity events that survive the fiducial volume cut. In order to reduce all these different contributions, we consider the following observables:

Effective distance to wall deff: the distance to the nearest detector wall along the event's

reconstructed direction. This observable allows to remove residual radioactivity background events which are mostly coming perpendicular to the wall.

Cherenkov angle θ_c: the opening angle of the Cherenkov light cone emitted by an electron is around 42° over a large energy range. Conversely, the angles heavier particles like muons and pions are significantly smaller than 42° in the low-energy analysis. In addition, neutral current (NC) interactions with multiple photon emissions can lead to superimposed Cherenkov cones as multiple MeV-scale photons can accelerate more than one electron through the Compton effect. These multiple overlapping cones will then be reconstructed as a single cone with a particularly large opening angle. Consequently, θ_c is one of the most powerful observables for reducing both NC and $\mu\pi$ atmospheric neutrino backgrounds.

Pion likeness *pilike*: electrons and positrons do not follow a straight trajectory in SK due to Coulomb multiple scatterings, which leads to fuzzy Cherenkov rings. Charged pions, on the other hand, lead to well-delineated ring patterns. In order to discriminate pion rings from electron rings we consider a 15 ns time-of-flight subtracted window around the main activity peak and compute the opening angles of the cones formed by the directions of all possible 3-hit combinations of the hit PMTs. We then identify the peak of this opening angle distribution θ_0 and estimate the "fuzzyness" of the ring by computing.

$$pilike = \frac{N_{\text{triple}}(\theta_0 \pm 3^\circ)}{N_{\text{triple}}(\theta_0 \pm 10^\circ)} \tag{6.2.10}$$

Rings with pilike close to one will be more pion-like.

Pre- and post-activity cuts: events where visible muons and pions decay into electrons can lead to two distinct activity peaks in the same trigger window. Depending on which particle deposits more light, unusually high activity can be noticed either before or after the main peak in the trigger window. For pre-activity we compute the maximal number of hits in a 15 ns time-of-flight subtracted window ending at least 12 ns before the main peak. We thus derive two observables, *maxpre* and *maxpregate*, by considering hits in the whole SHE trigger window and in the 1.3 μs gate around the main activity peak, respectively. For post-activity, we use the *muechk* function elaborated by the atmospheric neutrino analysis group to identify muon decays. This function evaluates the number of decay electrons.

6.2.5 Summary of Low-Energy Sample

After applying all reduction written above, the energy and $\cos\theta_{\text{Sun}}$ distribution is shown Fig. 6.7 and Fig. 6.8. θ_{Sun} is the angle between the reconstructed event direction and the vector pointing from the Sun to SK. Because of energy resolution of SK, the solar neutrino peak is seen in the right most bins of $\cos\theta_{\text{Sun}}$ distributions and the lowest energy bins of the energy distributions.

The overall efficiency of the low-energy samples for the true solar flare neutrino events is estimated by the signal MC as shown in Tab. 6.2.5.

Table 6.2: Reduction efficiency after each low-energy reduction step calculated by signal MC.

Efficiency	SK-I	SK-II	SK-III	SK-IV
1st Reduction	$> 99\%$	$> 99\%$	$> 99\%$	$> 99\%$
2nd Reduction	81.8%	76.2%	81.8%	82.7%
3rd Reduction	79.3%	85.2%	90.9%	90.2%

6.3 Summary for SK Data Analysis

The rate of BG events in this search was calculated from data other than the search time window. Table. 6.3 shows the background rate in each SK phase.

Table 6.3: Background event rate of each SK phase.

SK phase	SK-I	SK-II	SK-III	SK-IV
Low-energy (event/day)	0.20 ± 0.01	0.19 ± 0.02	0.20 ± 0.01	0.20 ± 0.01
High-energy (event/day)	7.45 ± 0.07	7.33 ± 0.09	7.53 ± 0.12	7.15 ± 0.05

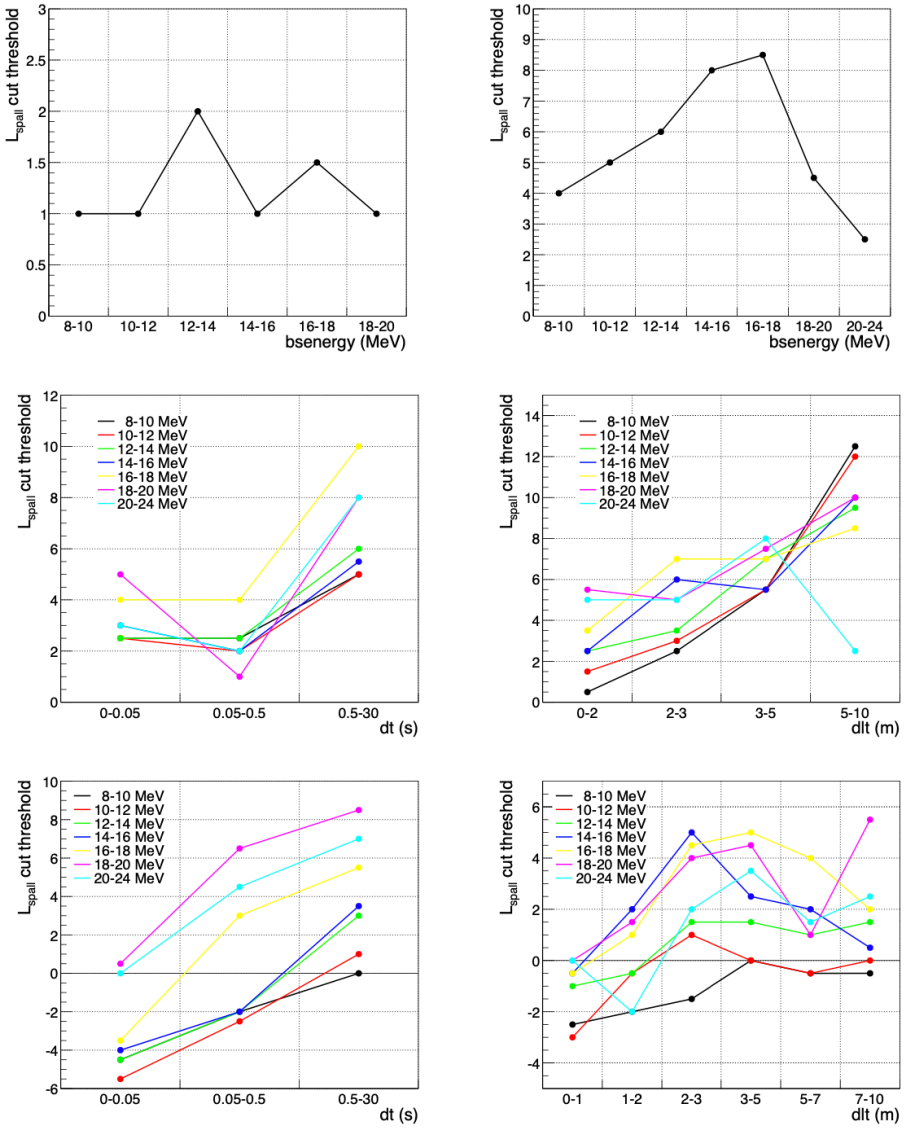

Figure 6.6: Likelihood cut thresholds for misfit (top left), stopping (top right), single through-going along dt (middle left) and dlt (middle right), and multiple muons along dt (bottom left) and dlt (bottom right). These are the exact cut conditions for misfit and stopping muons while give the initial points for the later scan.

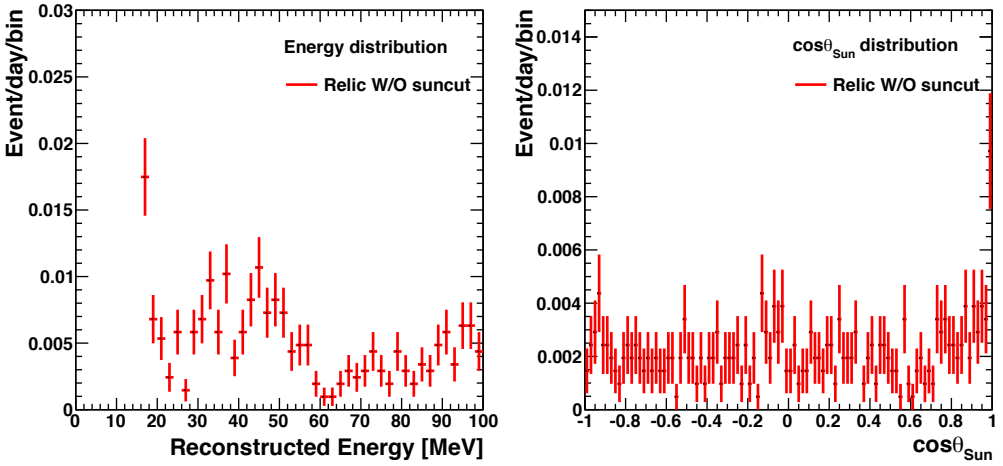

Figure 6.7: energy(left) and $\cos\theta_{\rm Sun}$(right) distribution SK I-III final sample. Because of energy resolution of SK, the solar neutrino peak is seen in most right bins of $\cos\theta_{\rm Sun}$ distributions and the lowest energy bin of the energy distributions.

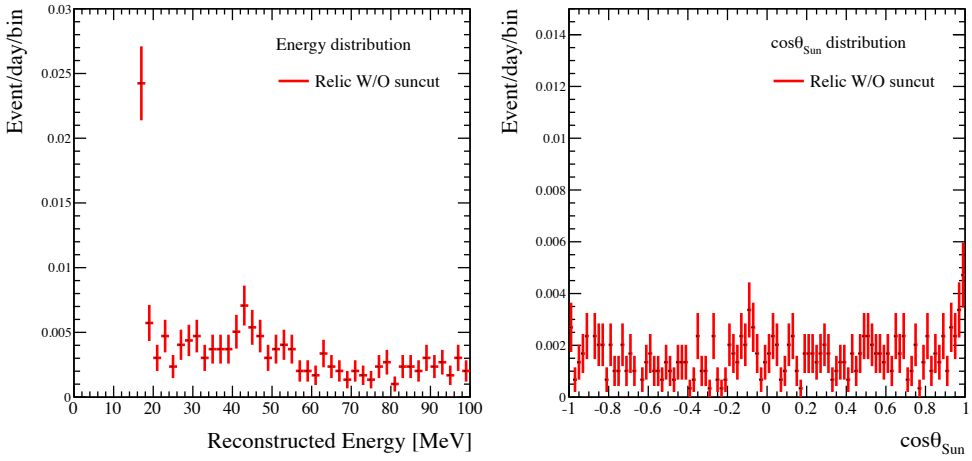

Figure 6.8: energy(left) and $\cos\theta_{\rm Sun}$(right) distribution SK IV final sample. Because of energy resolution of SK, the solar neutrino peak is seen in the most right bins of $\cos\theta_{Sun}$ distributions and the lowest energy bin of the energy distributions.

Chapter 7

Results and Discussions

7.1 Visible Side Solar Flares

Neutrino Search with the Time Windows Determined by Derivative of Soft X-ray light curves

As explained in Section 3.2, we selected twenty-three solar flares above X5.0 class occurring on the visible side of the solar surface. However, we can not search for solar flare neutrinos from the three solar flares occurring on August 25th, 2001, December 13th, 2001 and July 23rd, 2002 because no SK data is available due to the reconstruction work toward SK-II after the accident. Hence, we searched for solar flare neutrinos from the remaining twenty solar flares. As a consequence of the search, there is no signal detected in the low-energy data sample while two events in the high-energy data sample are detected as summarized in Table 7.1. Figures 7.1- 7.10 show the time distributions of neutrino events in SK around the search time windows. Figure 7.11 shows the time of observed events together with light curves recorded by the GOES satellite.

The event on November 4th, 2003 was observed during the impulsive phase of the solar flare, where particle acceleration is expected to be active. In addition to this, there was an observation of the neutron associated with this solar flare [117]. On the other hand, the event on September 6th, 2017 was observed during the dimming phase after the peak of the soft X-ray light curve, where all process of particle acceleration is likely to complete.

Figure 7.12 shows the energy of the observed event with the background energy spectrum. Here, the background sample is the events accumulated outside the search windows and the main component is the interaction of atmospheric neutrinos. The expected number of background events of high-energy data samples in the search time windows is 0.20 events (0.12 events) for solar flare event on November 4th, 2003 (September 6th, 2017). The probability of a background event is 18.1% (11.3%).

In order to investigate whether background events come from the direction of the Sun or not, we examined the angular distribution of θ_{Sun}, which is defined as the angle between the reconstructed direction of charged particle and the direction pointing from the Sun to SK.

Neutrino Search with the Time Windows Determined by Line γ-ray light curves

We set the search time windows by using 2.223 MeV γ-ray data that indicates hadron acceleration and neutrino existence in solar flares as described in Chap. 3. By using the search time windows

Table 7.1: The summary of two events observed within the search window for neutrinos associated with the solar flare occurring on the visible side of the Sun.

Date (UTC)	November 4th, 2003	September 6th, 2017
Solar flare class	X28.0	X9.4
SK phase	SK-II	SK-IV
Observed time (UTC)	19:42:26	12:03:05
Event topology	2-ring e-like	1-ring μ-like
Reconstructed energy	178.3 MeV	1.2 GeV
θ_{Sun}	67.1°	39.6°
Estimated background rate [event flare^{-1}]	0.20	0.12
Probability of background event	18.1%	11.3%

for solar flare events which occurring on November 2nd, 2003 and January 20th, 2005, the solar flare neutrino event has been sought in SK. However, there was no candidate neutrino event within the search time windows. For the solar flare occurring on July 23rd, 2002, we can not search for neutrino event because no SK data is available due to the reconstruction work toward SK-II after the accident.

7.2 Invisible Side Solar Flares

As explained in Section 3.3, we selected ten large CMEs occurring on the invisible side of the Sun by setting the criteria of their emission speed. Unfortunately, we can not search for solar flare neutrinos from the CMEs occurring on July 19th and 20th, 2002 because no SK data is available due to the reconstruction work toward SK-II after the accident. Hence, we searched for solar flare neutrinos from the remaining eight CMEs.

There is no signal in the low-energy data sample while six events in the high-energy data sample as summarized in Table 7.2. The numbers of observed events within the search time window are two events for the solar flares on November 7th, 2003 and July 24th, 2005 while one event for those on June 4th, 2011 and July 23rd, 2012. Figures 7.15-7.18 show the time distributions of neutrino events in SK around the search time windows.

In the case of two solar flares on November 7th, 2003, and on July 24th, 2005, we found two consecutive neutrino events within their search windows. Their time differences are 1131 s and 4065 s, respectively. We analyzed the time difference distribution between the consecutive events in the background sample in order to verify whether their time differences are rare or not. Figure 7.19 shows the time difference of two consecutive events observed within their search windows together with the time difference distribution of the background sample. Comparing the time difference distribution of the background sample, we estimated the occurrence probabilities for each solar flare, which corresponds to 10% and 29%. The black data points in Fig. 7.20 show the distribution of the number of neutrino candidates in each solar flare. It is consistent with the Poisson distribution with the estimated background rate of 0.62 event/flare as shown with the red histograms in the figure.

Figure 7.21 shows the energy of the observed event with the background energy spectrum. The expected number of background events of the high-energy data sample is 0.62 event/flare. It is the same for all the solar flares on the invisible side since the search time range is uniform for the solar flares on the invisible side.

Figures 7.22-7.27 show the angular distribution of the neutrino events from solar flares that

occurring on the invisible side of the solar surface and that of the signal simulation sample.

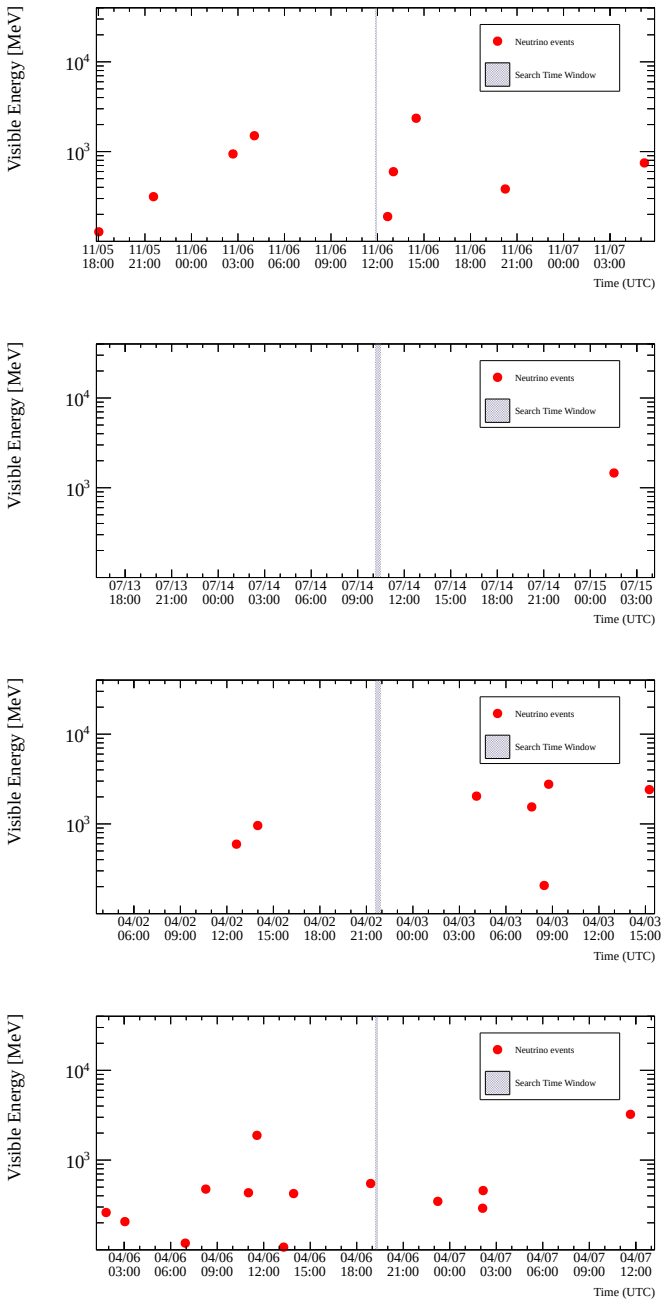

Figure 7.1: The time distributions of high-energy neutrino events around the solar flares occurring on the visible side of the Sun on November 6th, 1996 (top), July 14th, 2000 (upper-middle), April 2nd, 2001 (lower-middle), and April 6th, 2001 (bottom). The red points show the time of neutrino events.

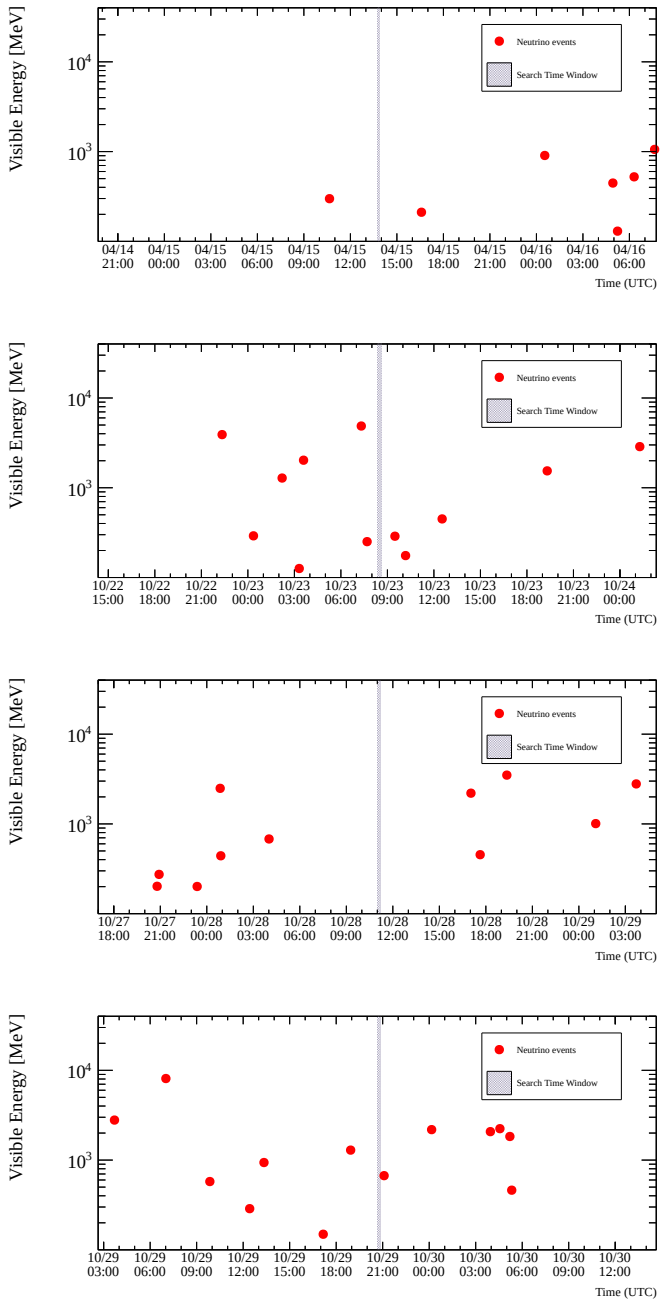

Figure 7.2: The time distributions of high-energy neutrino events around the solar flares occurring on the visible side of the Sun on April 15th, 2001 (top), October 23rd, 2003 (upper-middle), October 28th, 2003 (lower-middle), and October 29th, 2003 (bottom). The red points show the time of neutrino events.

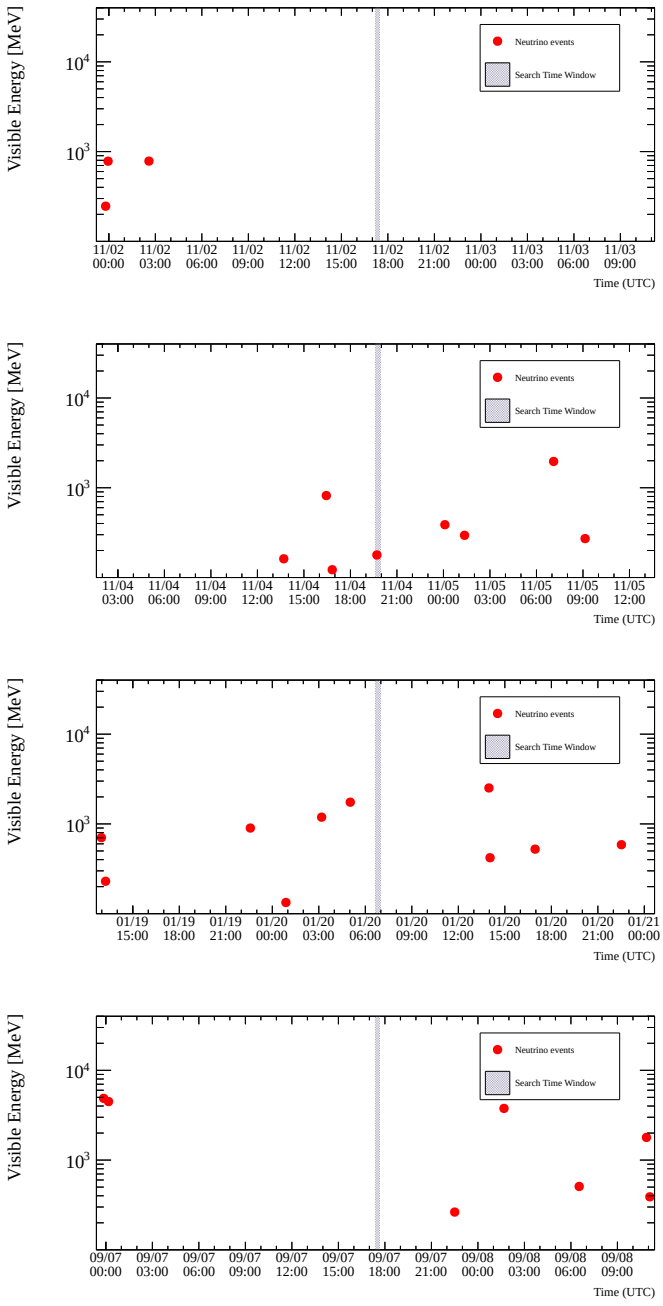

Figure 7.3: The time distributions of high-energy neutrino events around the solar flares occurring on the visible side of the Sun on November 2nd, 2003 (top), November 4th, 2003 (upper-middle), January 20th, 2005 (lower-middle), and September 7th, 2005 (bottom). The red points show the time of neutrino events.

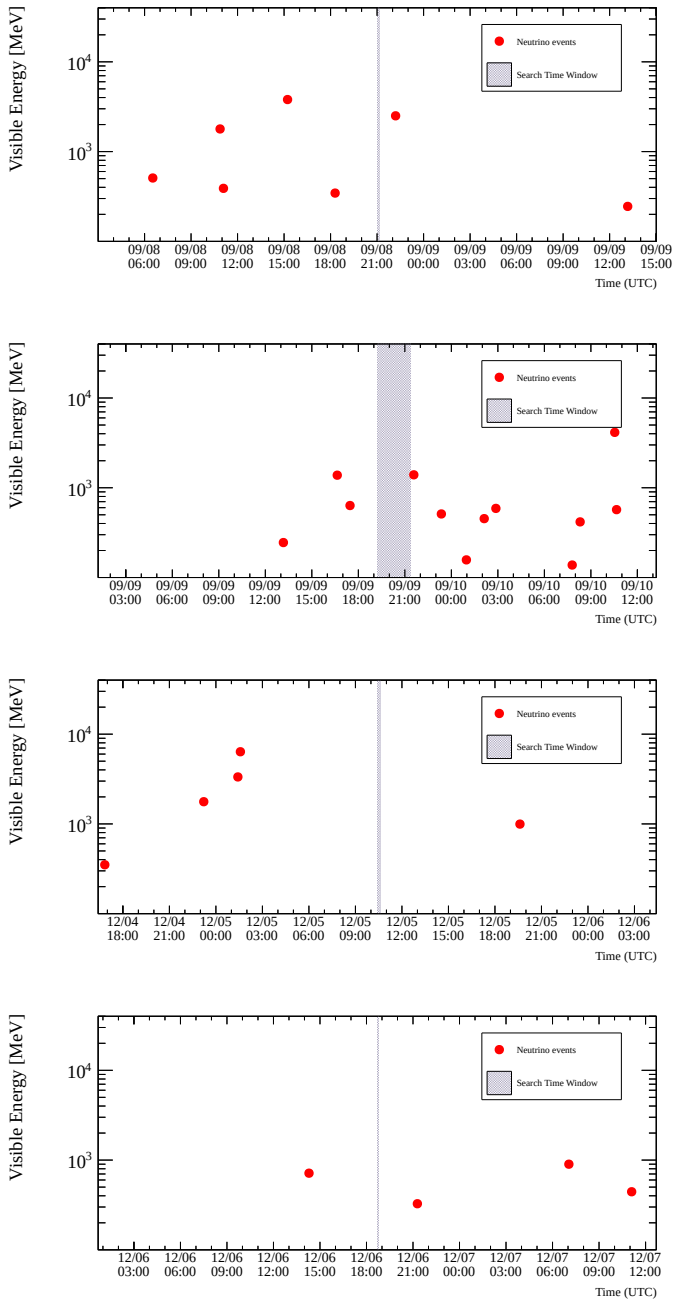

Figure 7.4: The time distributions of high-energy neutrino events around the solar flares occurring on the visible side of the Sun on September 8th, 2005 (top), September 9th, 2005 (upper-middle), December 5th, 2006 (lower-middle), and December 5th, 2006 (bottom). The red points show the time of neutrino events.

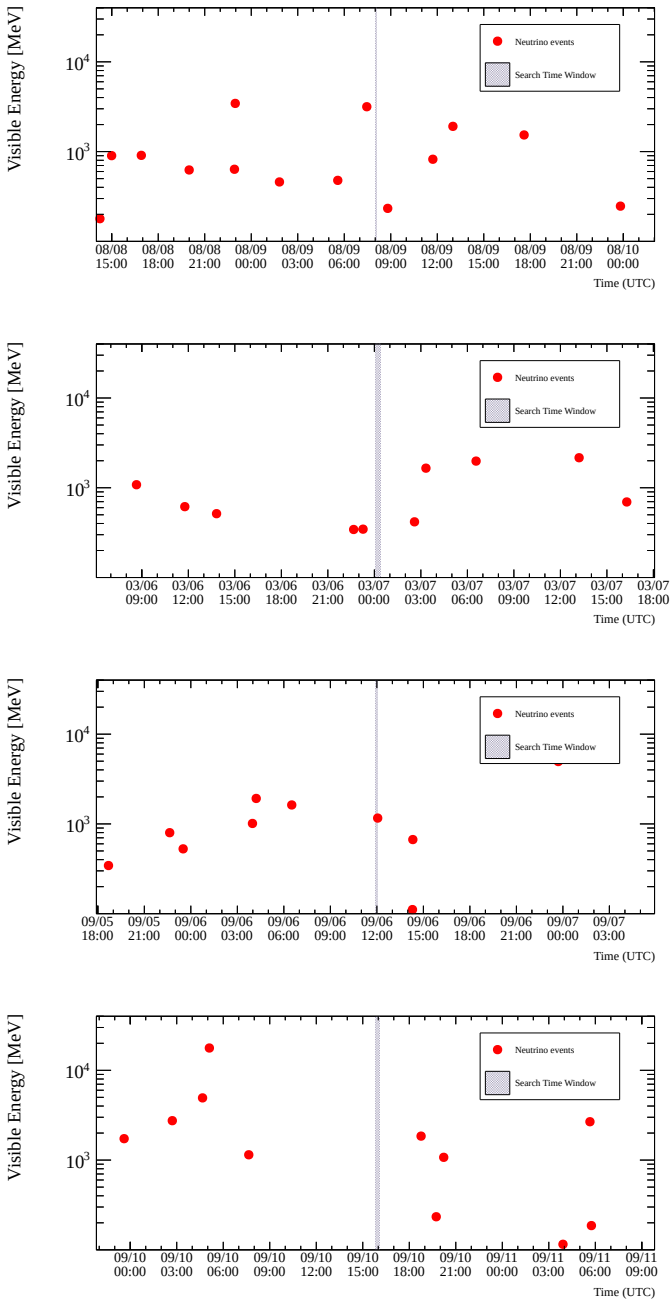

Figure 7.5: The time distributions of high-energy neutrino events around the solar flares occurring on the visible side of the Sun on August 9th, 2011 (top), March 7th, 2012 (upper-middle), September 6th, 2017 (lower-middle), and September 10th, 2017 (bottom). The red points show the time of neutrino events.

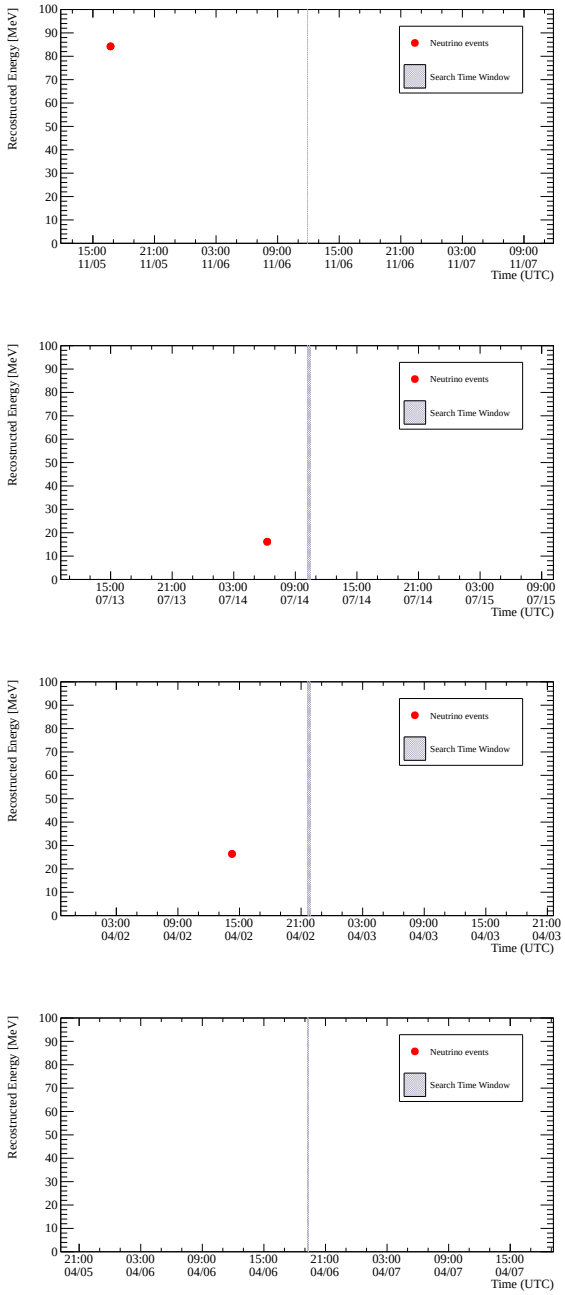

Figure 7.6: The time distributions of low-energy neutrino events around the solar flares occurring on the visible side of the Sun on November 6th, 1996 (top), July 14th, 2000 (upper-middle), April 2nd, 2001 (lower-middle), and April 6th, 2001 (bottom). The red points show the time of neutrino events.

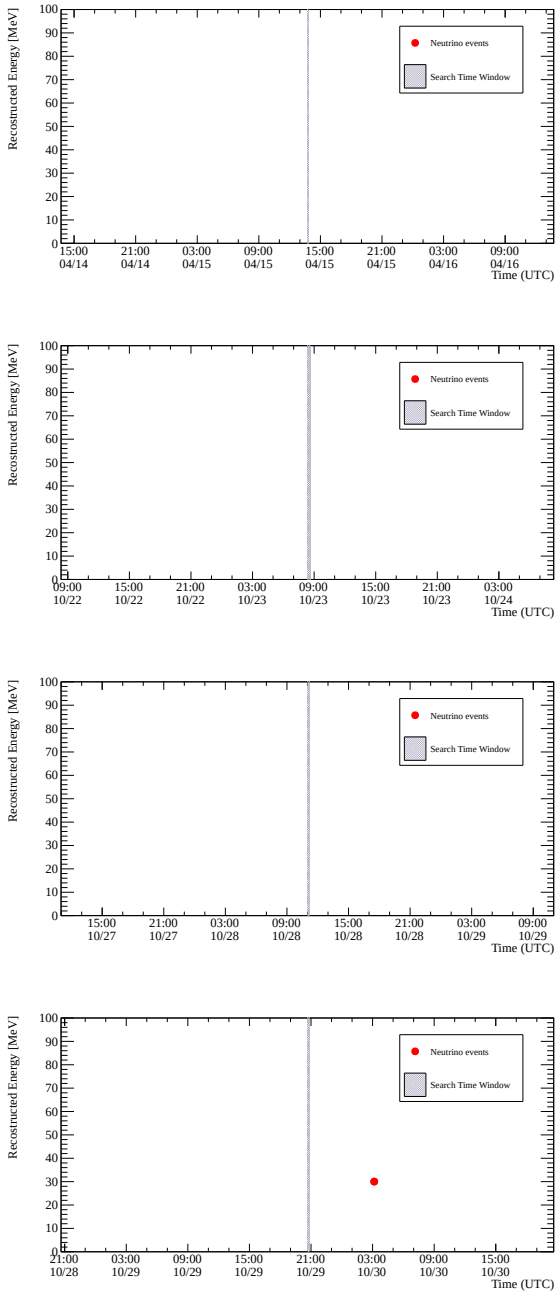

Figure 7.7: The time distributions of high-energy neutrino events around the solar flares occurring on the visible side of the Sun on April 15th, 2001 (top), October 23rd, 2003 (upper-middle), October 28th, 2003 (lower-middle), and October 29th, 2003 (bottom). The red points show the time of neutrino events.

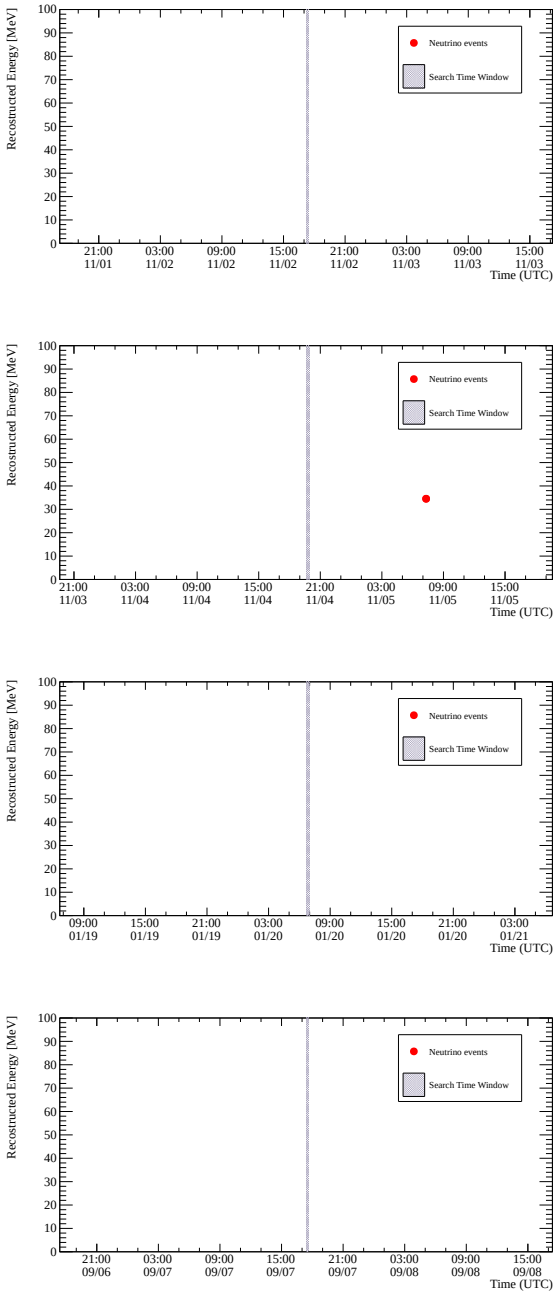

Figure 7.8: The time distributions of low-energy neutrino events around the solar flares occurring on the visible side of the Sun on November 2nd, 2003 (top), November 4th, 2003 (upper-middle), January 20th, 2005 (lower-middle), and September 7th, 2005 (bottom). The red points show the time of neutrino events.

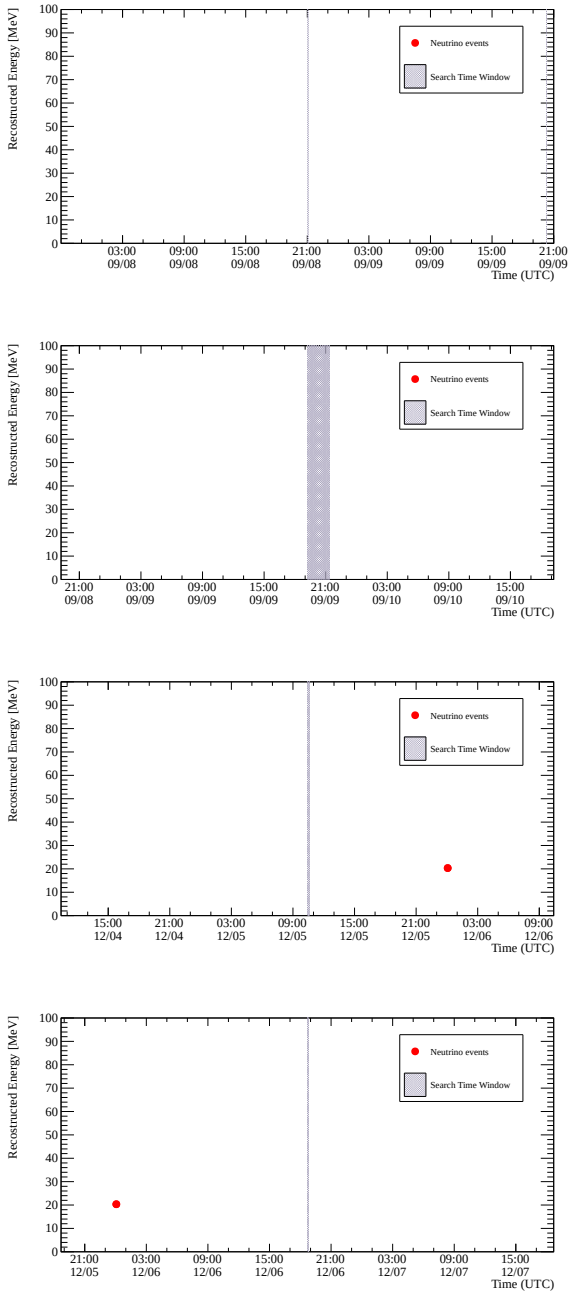

Figure 7.9: The time distributions of low-energy neutrino events around the solar flares occurring on the visible side of the Sun on September 8th, 2005 (top), September 9th, 2005 (upper-middle), December 5th, 2006 (lower-middle), and December 5th, 2006 (bottom). The red points show the time of neutrino events.

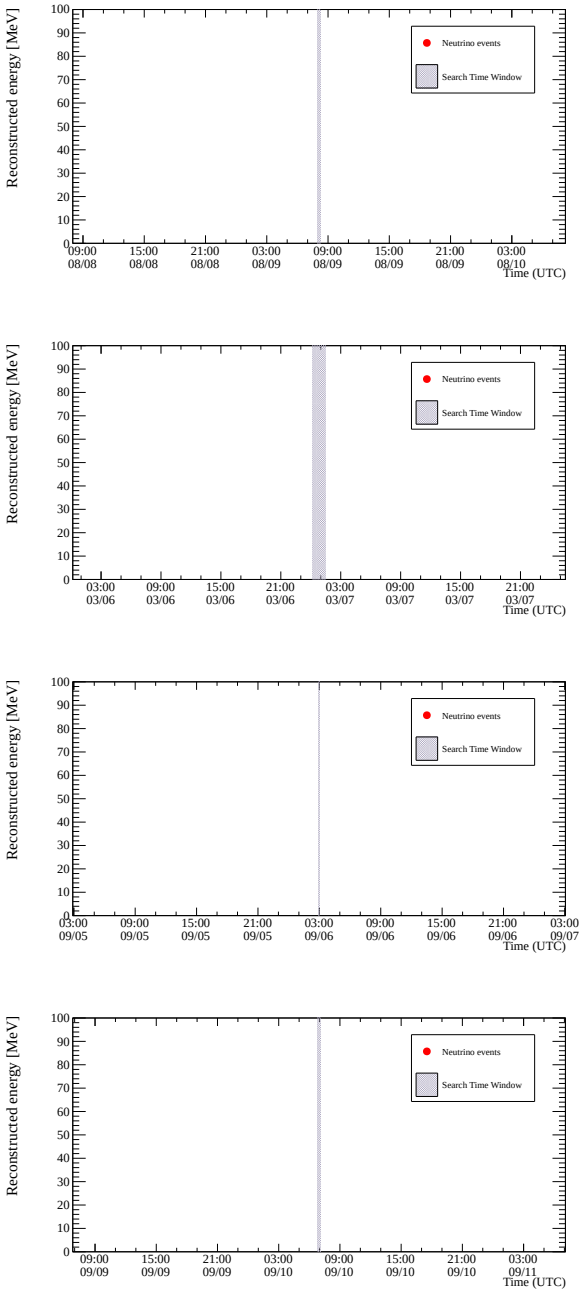

Figure 7.10: The time distributions of low-energy neutrino events around the solar flares occurring on the visible side of the Sun on August 9th, 2011 (top), March 7th, 2012 (upper-middle), September 6th, 2017 (lower-middle), and September 10th, 2017 (bottom). The red points show the time of neutrino events.

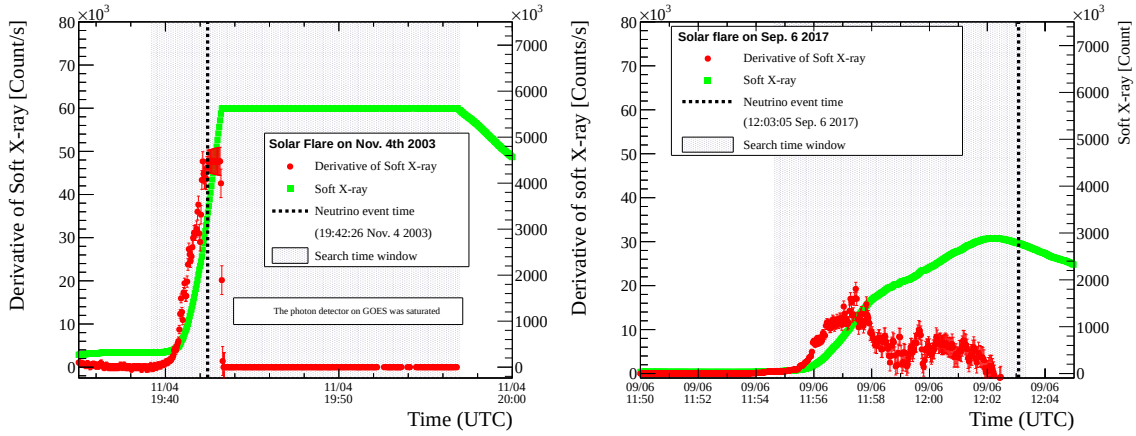

Figure 7.11: The time of observed neutrino events for the solar flare on November 4th, 2003 (left), and July 6th, 2017 (right). The black dotted line shows the time of neutrino event in the SK detector. The red (green) plot shows the derivative of the light curves (original light curve) recorded by the GOES satellite. The shaded region shows the search windows determined by using the derivative of soft X-ray light curve according to the method described in Chap. 3. In the case of the solar flare on November 4th, 2003 (left), the instrument on the GOES satellite saturated due to the high intensity of soft X-rays. This did not allow the satellite to record the data for more than 15 minutes from 19:45 to 20:00.

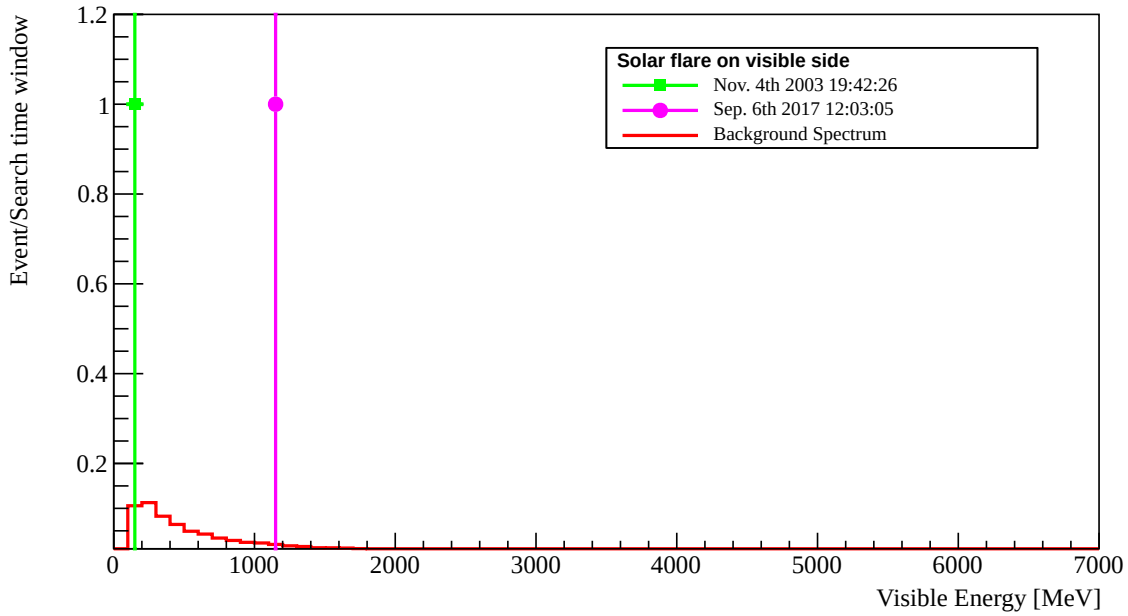

Figure 7.12: The energy distribution of the two neutrino events observed in the time window for solar flares occurring on the visible side of the Sun and that of the background sample. The first event (a green square) was observed as 2-ring e-like event on November 4th, 2003 while the other (a magenta circle) was observed as 1-ring μ-like event on September 6th, 2017. The background spectrum is normalized by the average duration of 700 s determined from the derivative of the soft X-ray light curve.

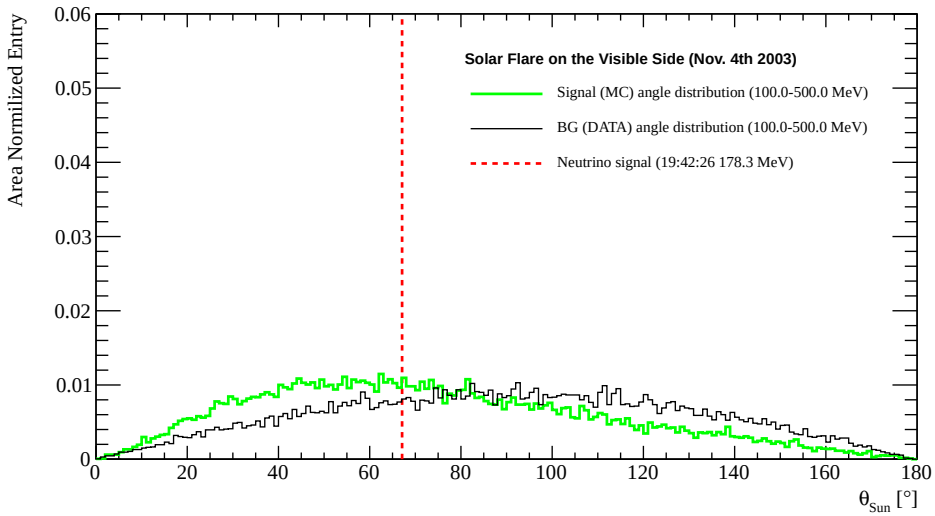

Figure 7.13: The angular distribution of the neutrino events from solar flares occurring on November 4th, 2003, and that of signal simulation sample. The green thick and the black thin line shows the angular distribution of signal MC and Background sample, respectively. The red dashed line shows the angular, θ_{Sun}, of the candidate neutrino event.

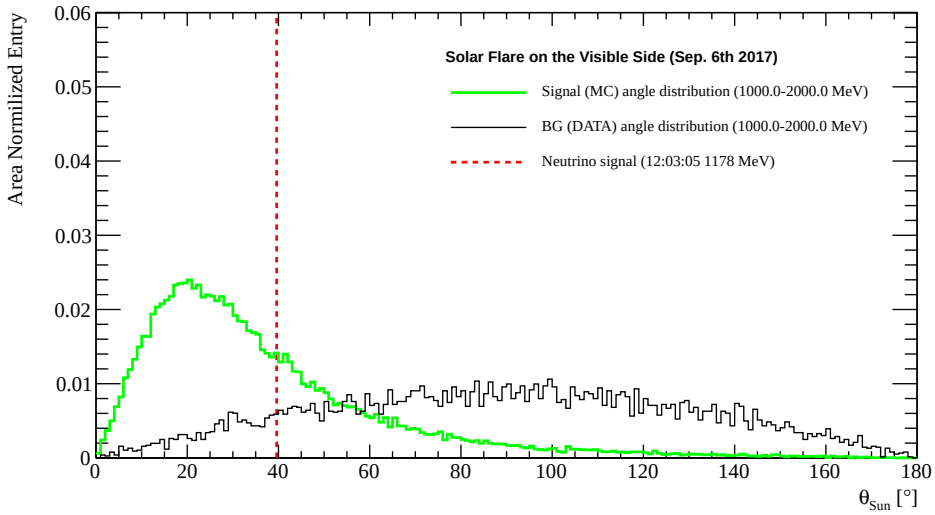

Figure 7.14: The angular distribution of the neutrino events from solar flares occurring on September 6th, 2017, and that of the signal simulation sample. The green thick and the black thin line shows the angular distribution of signal MC and Background sample, respectively. The red dashed line shows the angular, θ_{Sun}, of the candidate neutrino event.

Table 7.2: The summary of events observed within the search window for neutrinos associated with the solar flare occurring on the invisible side of the Sun.

Date (UTC)	November 7th, 2003	July 24th, 2005	June 4th, 2011	July 23rd, 2012
SK phase	SK-II	SK-II	SK-IV	SK-IV
Number of candidates	2	2	1	1
Observed time (UTC)	00:18:34	22:07:36	06:05:07	12:03:47
	00:40:45	23:15:21	–	–
Event topology	1-ring e-like	1-ring μ-like	4-ring e-like	3-ring two μ-like, e-like
	2-ring e-like	1-ring μ-like	–	–
Reconstructed energy	3.58 GeV	126 MeV	2.14 GeV	834 MeV
	493 MeV	1.35 GeV	–	–
Estimated background rate [event $\cdot$ flare^{-1}]	0.62	0.62	0.62	0.62
$\theta_{\rm Sun}$	20.0°	100.4°	101.0°	76.7°
	71.4°	94.0°	–	–
Probability of background event from background rate	12.8%	12.8%	46.2%	46.2%
Probability of background event from timing distribution	10.0%	29.0%	–	–

7.3 Fluence Calculation

Since the number of neutrino candidates is consistent with the number of expected backgrounds, we have converted that to the upper limit on the neutrino fluence. In this thesis, the limits of the solar flare neutrinos were calculated using the predictions from Fargion and Moscato [42], Kocharov et. al [43], and Takeishi et. al [44]. The probability density function of the number of the observed event for the low-energy data set is defined as follows:

$$\begin{aligned} P_{\rm Low}(S+B|n_{\rm obs}) &= \frac{1}{A}\iiint \frac{{\rm e}^{-(S+B)}(S+B)^{n_{\rm obs}}}{n_{\rm obs}!} \\ &\times\ G(\Delta\sigma_{\rm IBD})G(\Delta\varepsilon_{\rm Low})G(\Delta B){\rm d}(\Delta\sigma_{\rm IBD}){\rm d}(\Delta\varepsilon_{\rm Low}){\rm d}(\Delta B), \quad (7.3.1) \\ S &\equiv N_p t_{\rm emit}\int F(E_\nu)\sigma_{\rm IBD}(E_\nu)\varepsilon_{\rm Low}(E_\nu){\rm d}E_\nu, \quad (7.3.2) \end{aligned}$$

where S represents number of expected signal, A is a normalization factor representing the total integral of $P_{\rm Low}(S+B|n_{\rm obs})$, $n_{\rm obs}$ is number of observed events in the search time window, N_p is the number of target proton in SK relevant to the neutrino interactions, F is predicted neutrino flux in unit of cm^{-2} sec^{-1} MeV^{-1}, $t_{\rm emit}$ is time duration of neutrino emission in a solar flare, which is assumed as 100 sec, $\sigma_{\rm IBD} = \sigma_{0,\rm IBD} + \Delta\sigma_{\rm IBD}$ is the IBD cross section as a function of electron anti neutrino energy derived from the simulation, $\sigma_{0,\rm IBD}$ is the best estimate and $\Delta\sigma_{\rm IBD}$ is the deviation, $\varepsilon_{\rm Low} = \varepsilon_{0,\rm Low} + \Delta\varepsilon_{\rm Low}$ is the reduction efficiency of the low-energy sample, $\varepsilon_{0,\rm Low}$ is the best estimate and $\Delta\varepsilon_{\rm Low}$ is the deviation, and $B = B_0 + \Delta B$ is number of expected background events in the search window, B_0 is the best estimate and ΔB is the deviation. $G(\Delta\sigma_{\rm IBD})$, $G(\Delta\varepsilon_{\rm Low})$, $G(\Delta B)$ represent the prior probabilities for fluctuation of the IBD cross section, the reduction efficiency and number of expected background event in the search time window, respectively. They are assumed to be Gaussian functions,

$$G(\Delta\sigma_{\rm IBD}) = \frac{1}{\sqrt{2\pi\delta^2_{\sigma_{\rm IBD}}}}\exp(-\frac{(\Delta\sigma_{\rm IBD})^2}{2\delta^2_{\sigma_{\rm IBD}}}), \quad (7.3.3)$$

$$G(\Delta\varepsilon_{\rm Low}) = \frac{1}{\sqrt{2\pi\delta^2_{\varepsilon_{\rm Low}}}}\exp(-\frac{(\Delta\varepsilon_{\rm Low})^2}{2\delta^2_{\varepsilon_{\rm Low}}}), \quad (7.3.4)$$

$$G(\Delta B) = \frac{1}{\sqrt{2\pi\delta^2_B}}\exp(-\frac{(\Delta B)^2}{2\delta^2_B}), \quad (7.3.5)$$

where $\delta_{\sigma_{\rm IBD}}$, $\delta_{\varepsilon_{\rm Low}}$ and δ_B are systematic uncertainties of the the IBD cross section, the reduction efficiency and number of expected backgound event in the search time window, respectively.

Neutrino fluence can be calculated by using flux F,

$$\Phi = t_{\rm emit}\int F(E){\rm d}E, \quad (7.3.6)$$

With these definitions, the neutrino fluence limit at a given confidence level (C.L.) is caluculated as

$$\text{C.L.} = \frac{\int_0^{\Phi_{\rm lim}} P_{\rm Low}(S+B|n_{\rm obs}){\rm d}\Phi}{\int_0^{\infty} P_{\rm Low}(S+B|n_{\rm obs}){\rm d}\Phi}. \quad (7.3.7)$$

The fluence limits obtained from low-energy data set is given in Tables 7.3 and 7.4.

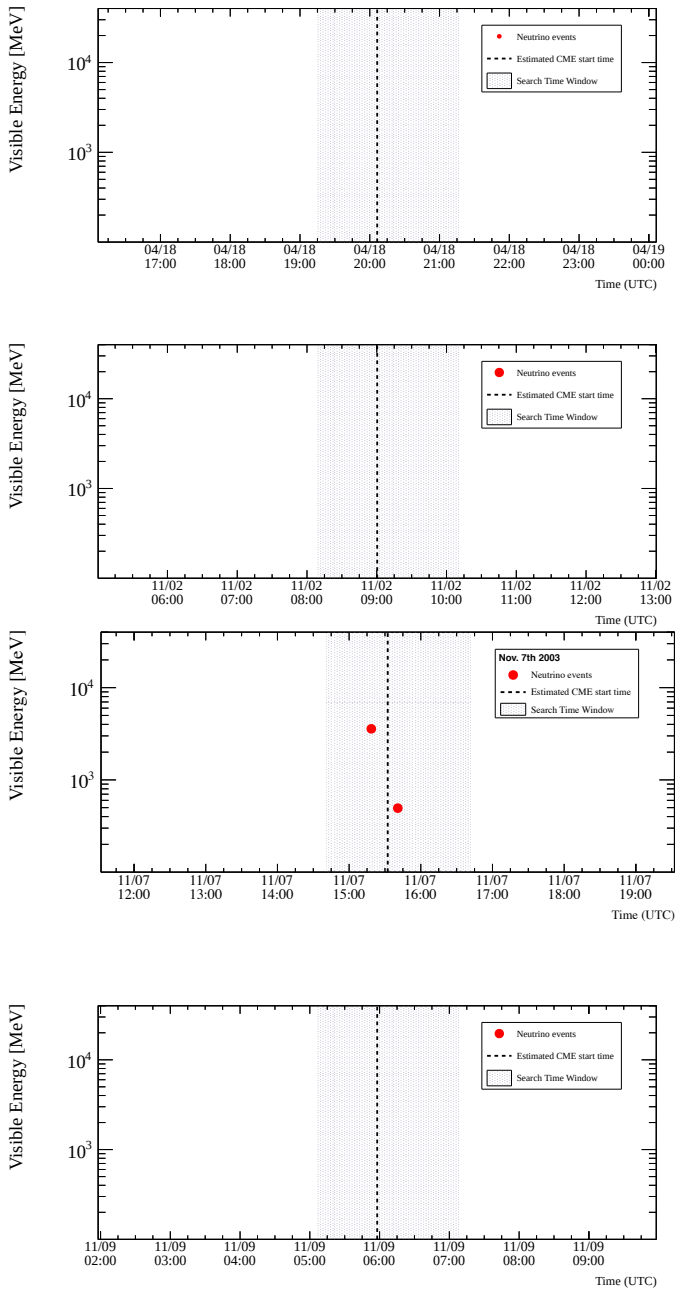

Figure 7.15: The time distributions of high-energy neutrino events around the solar flares occurring on the invisible side of the Sun on April 18th, 2001 (top), November 2nd, 2003 (upper-middle), November 7th, 2003 (lower-middle), and November 9th, 2003 (bottom). The red points show the time of neutrino events. The dashed vertical line shows the estimated start time of particular CME emission and the shaded regions show the search windows according to the method described in Section 3.3.2.

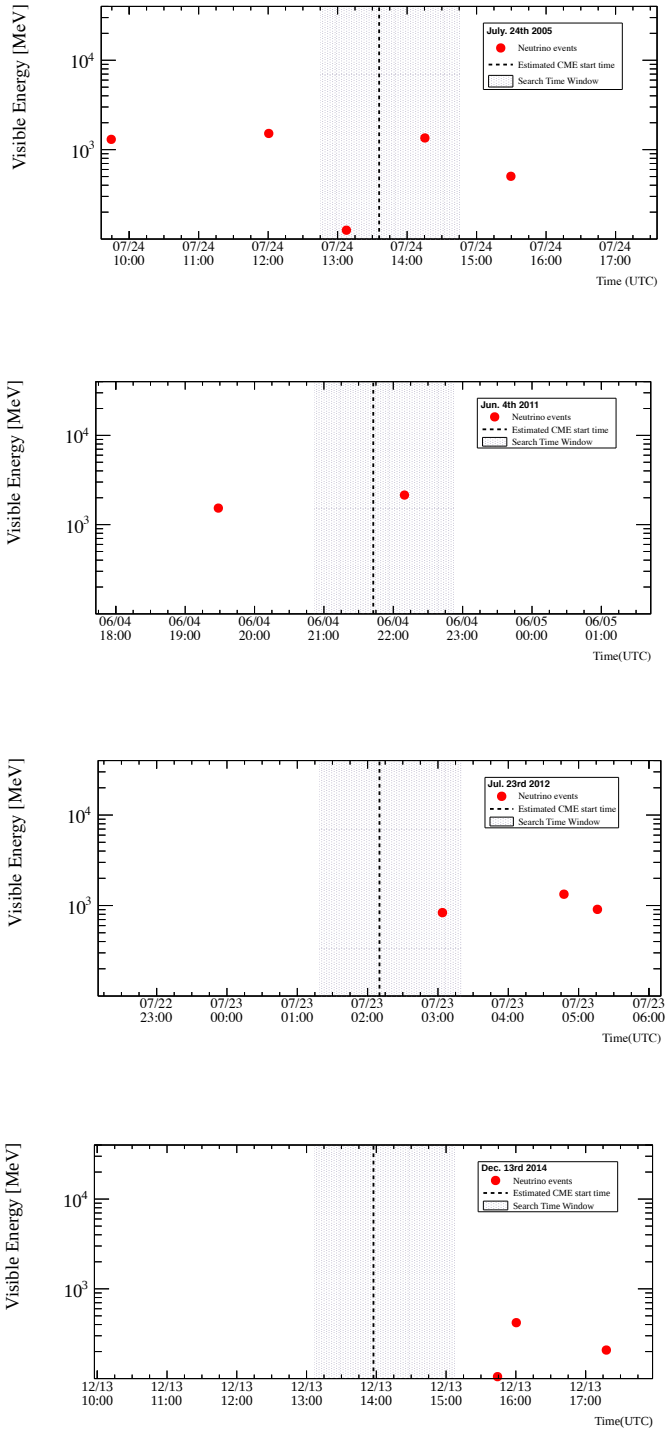

Figure 7.16: The time distributions of high-energy neutrino events around the solar flares occurring on the invisible side of the Sun on July 24th, 2005 (top), June 4th, 2011 (upper-middle), July 23rd, 2012 (lower-middle) December 13th, 2014 (bottom). The red points show the time of neutrino events. The dashed vertical line shows the estimated start time of particular CME emission and the shaded regions show the search windows according to the method described in Section 3.3.2.

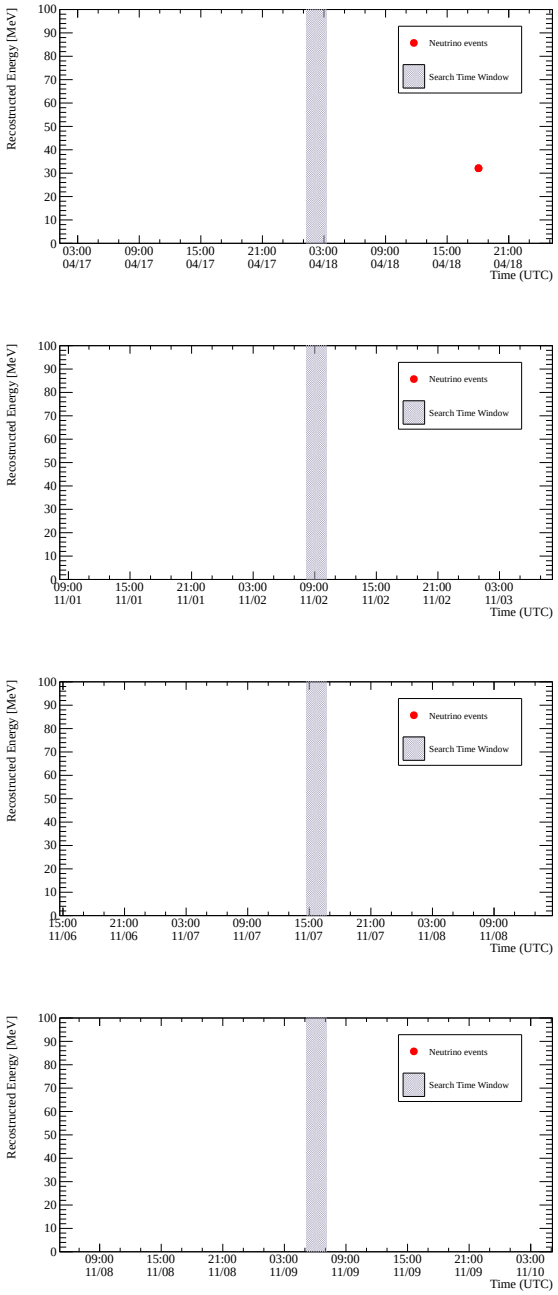

Figure 7.17: The time distributions of low-energy neutrino events around the solar flares occurring on the invisible side of the Sun on July 24th, 2005 (top), June 4th, 2011 (upper-middle), July 23rd, 2012 (lower-middle) December 13th, 2014 (bottom). The red points show the time of neutrino events.

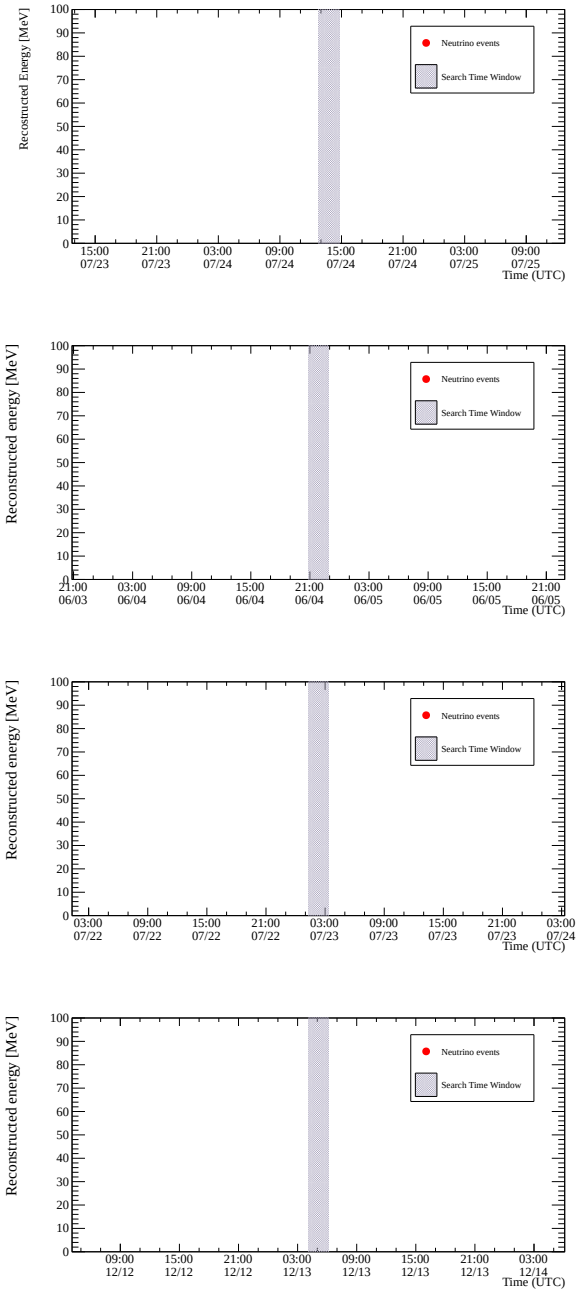

Figure 7.18: The time distributions of low-energy neutrino events around the solar flares occurring on the invisible side of the Sun on July 24th, 2005 (top), June 4th, 2011 (upper-middle), July 23rd, 2012 (lower-middle) December 13th, 2014 (bottom). The red points show the time of neutrino events.

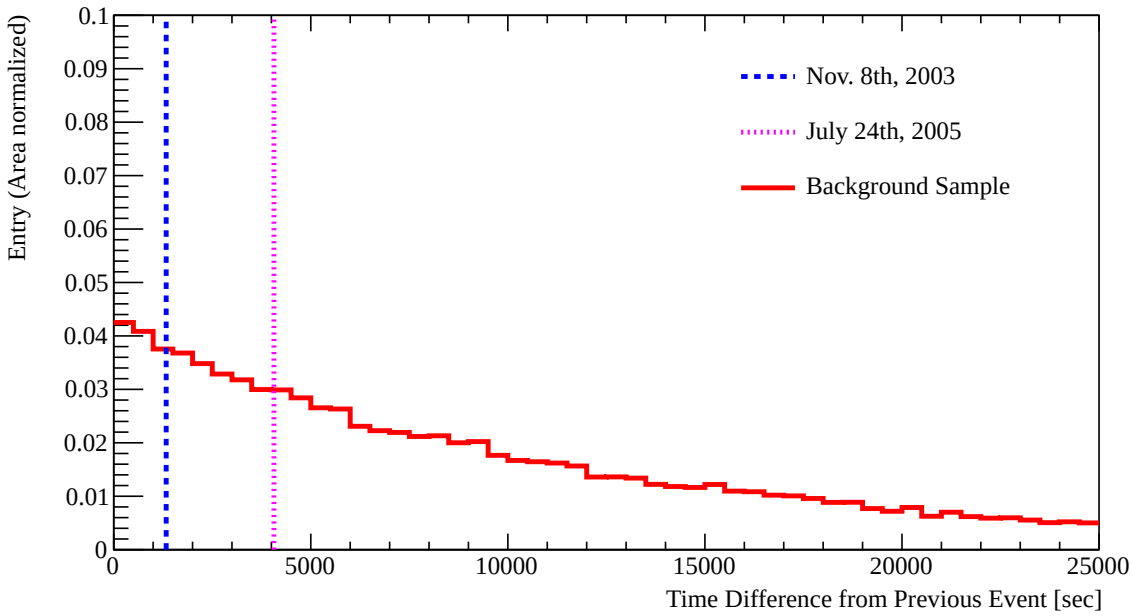

Figure 7.19: The time difference between the two events observed within the search windows for solar flares on November 8th, 2003 (dashed blue line) and July 24th, 2005 (dotted pink line). The red histograms show the area normalized distribution of the time difference between the consecutive events in the background sample.

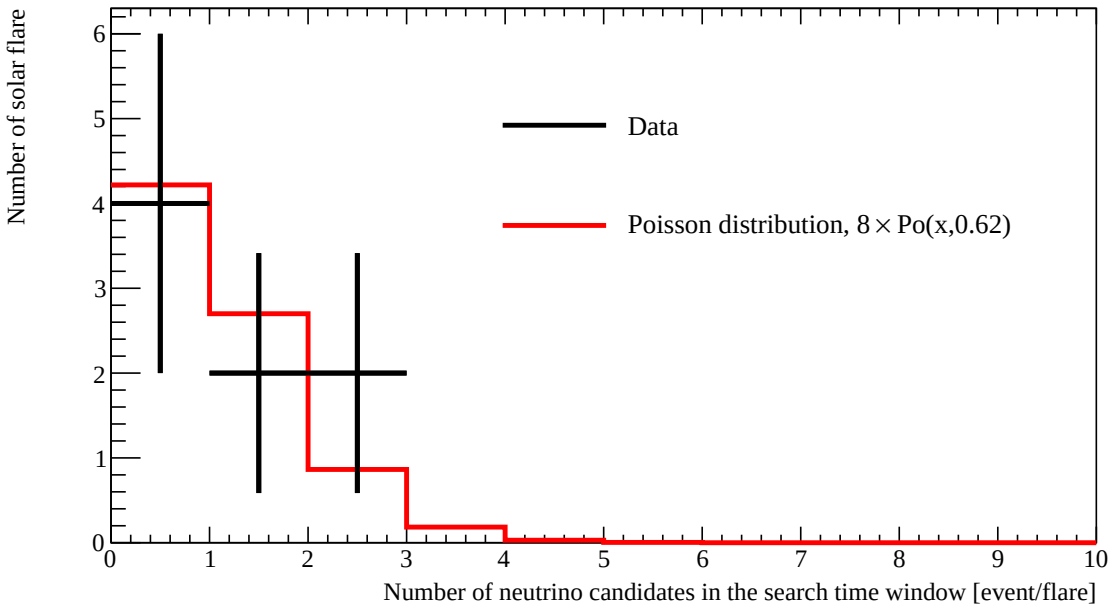

Figure 7.20: The distribution of the number of neutrino candidates in the search time window per one solar flare. The black lines show the distribution of the number of neutrino candidates from solar flares on the invisible side. The red histograms show the Poisson distribution with the estimated background rate, 0.62 event/flare, as the mean. The red histograms is normalized as the area to be 8, which is the number of solar flares occurring on the invisible side.

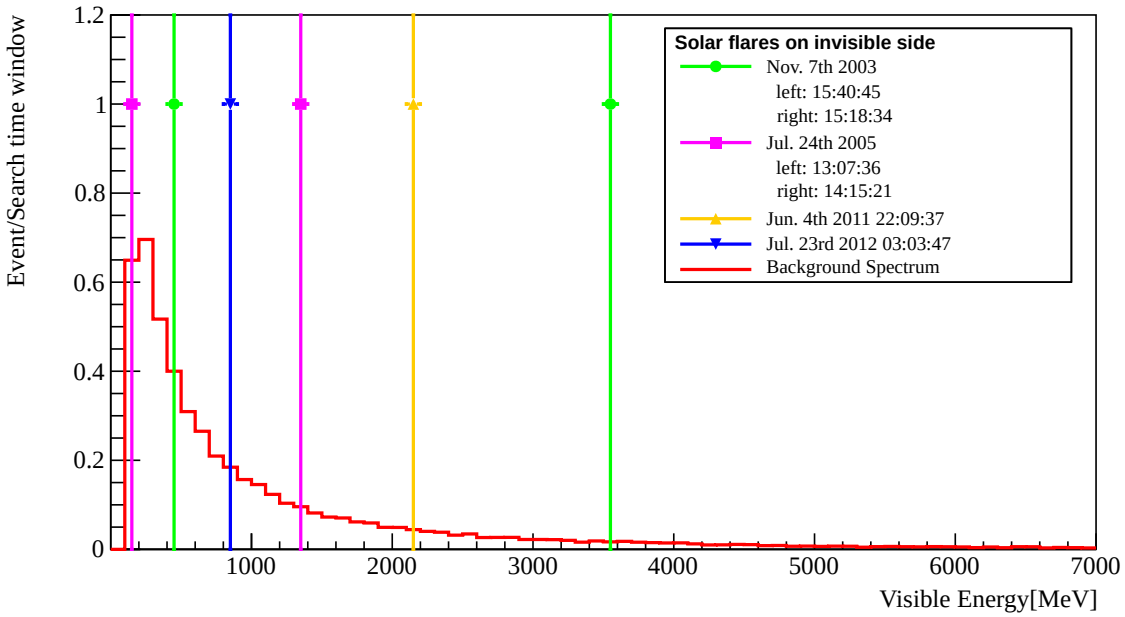

Figure 7.21: The energy distribution of the neutrino events observed in the time window for solar flares occurring on the invisible side of the Sun and that of the background sample. The green circle, magenta square, yellow upward triangle, blue downward triangle are the energy of observed events on November 7th, 2003, July 24th, 2005, June 4th, 2011, and July 23rd, 2012, respectively. The background spectrum is normalized by the time duration of 7238 s according to the method described in Section 3.3.1.

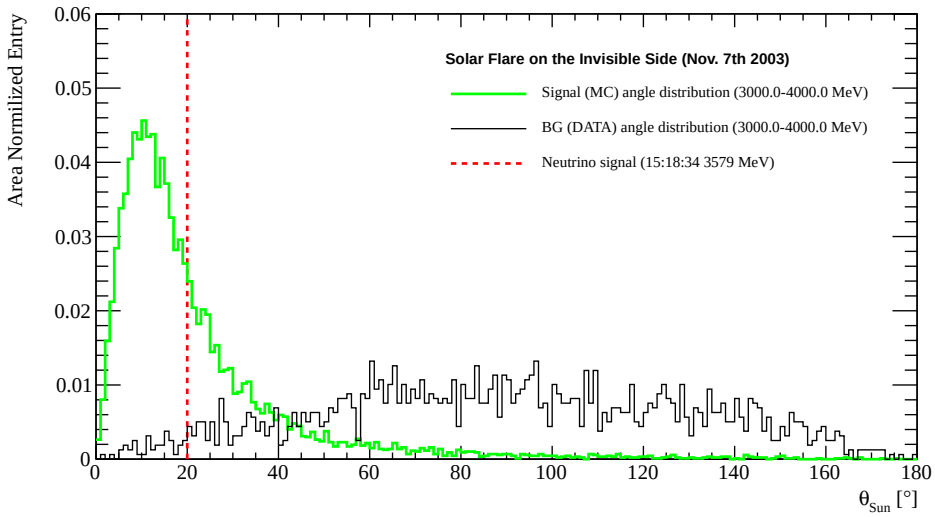

Figure 7.22: The angular distribution of the neutrino events from the solar flare occurring on November 7th, 2003, and that of the signal simulation sample. The green thick and the black thin histograms show the angular distribution of signal MC and Background sample, respectively. The red dashed line shows the angle from the Sun, θ_{Sun}, of the candidate neutrino event.

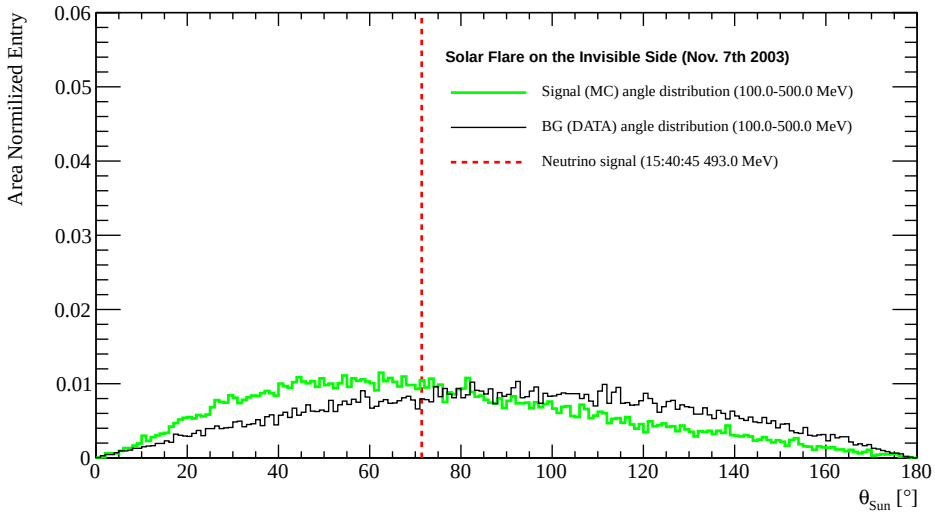

Figure 7.23: The angular distribution of the neutrino events from the solar flare occurring on November 7th, 2003, and that of the signal simulation sample. The green thick and the black thin histograms show the angular distribution of signal MC and Background sample, respectively. The red dashed line shows the angle from the Sun, θ_{Sun}, of the candidate neutrino event.

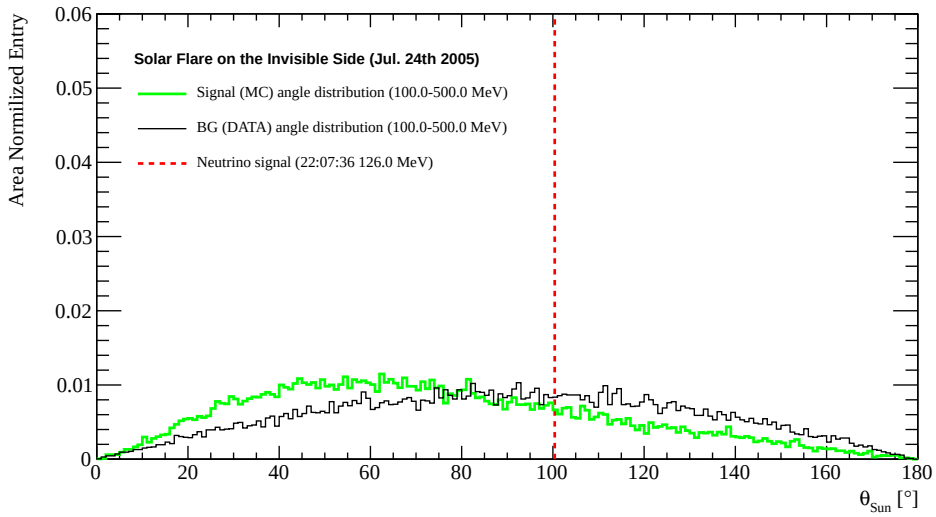

Figure 7.24: The angular distribution of the neutrino events from the solar flare occurring on July 23rd, 2005, and that of the signal simulation sample. The green thick and the black thin histograms show the angular distribution of signal MC and Background sample, respectively. The red dashed line shows the angle from the Sun, $\theta_{\rm Sun}$, of the candidate neutrino event.

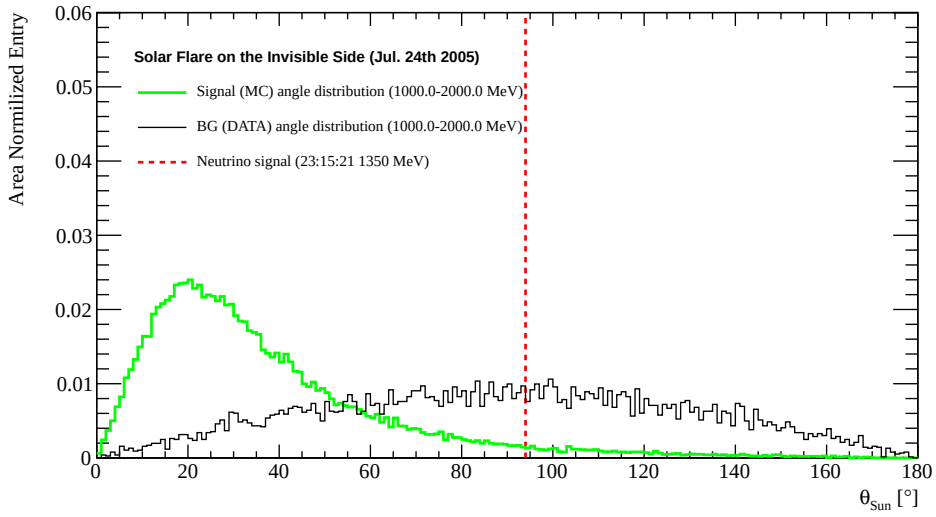

Figure 7.25: The angular distribution of the neutrino events from the solar flare occurring on July 23rd, 2005, and that of the signal simulation sample. The green thick and the black thin histograms show the angular distribution of signal MC and Background sample, respectively. The red dashed line shows the angle from the Sun, $\theta_{\rm Sun}$, of the candidate neutrino event.

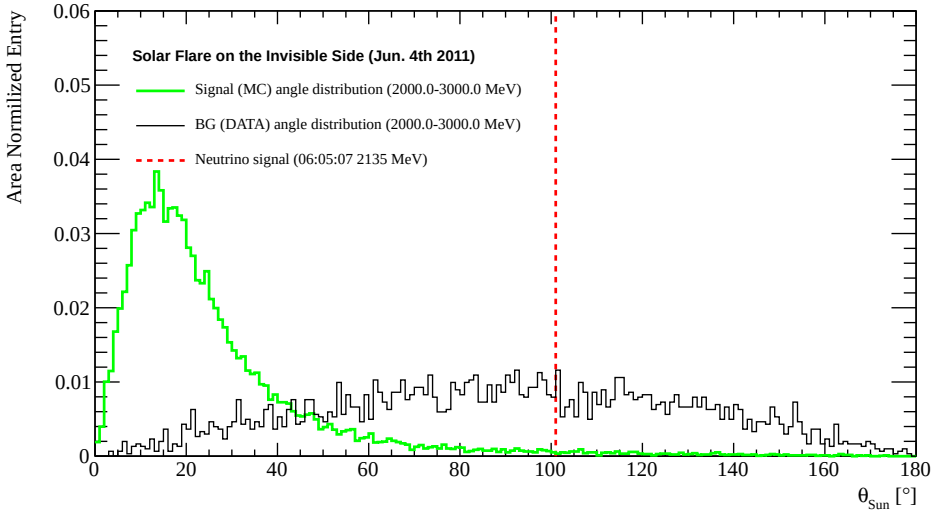

Figure 7.26: The angular distribution of the neutrino events from the solar flare occurring on June 4th, 2011, and that of the signal simulation sample. The green thick and the black thin histograms show the angular distribution of signal MC and Background sample, respectively. The red dashed line shows the angle from the Sun, θ_{Sun}, of the candidate neutrino event.

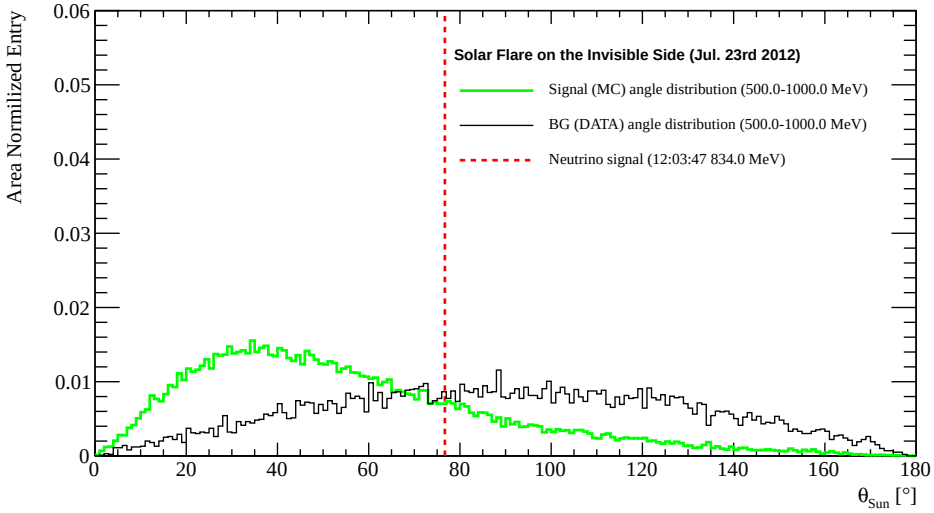

Figure 7.27: The angular distribution of the neutrino events from the solar flare occurring on July 23rd, 2012, and that of the signal simulation sample. The green thick and the black thin histograms show the angular distribution of signal MC and Background sample, respectively. The red dashed line shows the angle from the Sun, θ_{Sun}, of the candidate neutrino event.

Table 7.3: The summary of fluence limits for the low-energy sample for solar flares on the visible side. We assumed the energy spectrum from Fargion and Moscato [42] and the neutrino interactions from Strumia and Vissani [113]. The search time windows are same as in Table 3.9

Date	Derivative of soft X-rays		Line γ-ray (RHESSI)		Number of candidate	Expected background	Fluence limits
	Start	End	Start	End	event [event]	rate [event/flare]	[$\mathrm{cm}^{-2}\,\mathrm{flare}^{-1}$]
1997 Nov. 6	11:52:13	11:54:58	–	–	0	0.0004	$< 1.7 \times 10^7$
2000 Jul. 14	10:08:44	10:28:31	–	–	0	0.0027	$< 1.7 \times 10^7$
2001 Apr. 2	21:35:10	21:52:57	–	–	0	0.0025	$< 1.7 \times 10^7$
2001 Apr. 6	19:12:32	19:21:31	–	–	0	0.0012	$< 1.7 \times 10^7$
2001 Apr. 15	13:43:48	13:51:03	–	–	0	0.0010	$< 1.7 \times 10^7$
2001 Aug. 25	16:28:36	16:33:38	–	–	No SK data	-	-
2001 Dec. 13	14:24:25	14:31:05	–	–	No SK data	-	-
2002 Jul. 23	00:25:08	00:31:36	00:26:28	00:56:22	No SK data	-	-
2003 Oct. 23	08:20:32	08:36:03	–	–	0	0.0022	$< 1.7 \times 10^7$
2003 Oct. 28	10:59:30	11:10:57	–	–	0	0.0016	$< 1.7 \times 10^7$
2003 Oct. 29	20:38:46	20:50:07	–	–	0	0.0016	$< 1.7 \times 10^7$
2003 Nov. 2	17:12:01	17:26:03	17:14:14	17:36:41	0	0.0019	$< 1.7 \times 10^7$
2003 Nov. 4	19:36:59	19:56:03	–	–	0	0.0026	$< 1.7 \times 10^7$
2005 Jan. 20	06:39:22	06:57:12	06:42:54	07:09:52	0	0.0025	$< 1.7 \times 10^7$
2005 Sep. 7	17:23:34	17:39:48	–	–	0	0.0023	$< 1.7 \times 10^7$
2005 Sep. 8	21:00:27	21:08:05	–	–	0	0.0011	$< 1.7 \times 10^7$
2005 Sep. 9	19:13:00	21:20:36	–	–	0	0.018	$< 1.7 \times 10^7$
2006 Dec. 5	10:24:18	10:35:43	–	–	0	0.0016	$< 1.7 \times 10^7$
2006 Dec. 6	18:41:29	18:47:06	–	–	0	0.0008	$< 1.7 \times 10^7$
2011 Aug. 9	08:00:50	08:05:40	–	–	0	0.0007	$< 1.7 \times 10^7$
2012 Mar. 7	00:04:21	00:25:16	–	–	0	0.0029	$< 1.7 \times 10^7$
2017 Sep. 6	11:54:39	12:03:20	–	–	0	0.0012	$< 1.7 \times 10^7$
2017 Sep. 10	15:49:12	16:06:32	–	–	0	0.0024	$< 1.7 \times 10^7$

Table 7.4: The summary of fluence limits for the low-energy sample for solar flares on the invisible side. We assumed the energy spectrum from Fargion and Moscato [42] and the neutrino interactions from Strumia and Vissani [113]. The search time windows are same as in Table 3.10

Date	Search Time Window		Number of candidate	Expected background	Fluence limits
	Start	End	event [event]	rate [event/flare]	[$\mathrm{cm}^{-2}\,\mathrm{flare}^{-1}$]
2001 Apr. 18	01:15:24	03:16:02	0	0.002	$< 1.7 \times 10^7$
2002 Jul. 18	18:07:20	20:07:58	No SK data	-	-
2002 Jul. 19	15:13:34	17:14:12	No SK data	-	-
2003 Nov. 2	08:09:23	10:10:01	0	0.002	$< 1.7 \times 10^7$
2003 Nov. 7	14:41:19	16:41:57	0	0.002	$< 1.7 \times 10^7$
2003 Nov. 9	05:06:57	07:45:29	0	0.002	$< 1.7 \times 10^7$
2005 Jul. 24	12:44:51	14:45:29	0	0.002	$< 1.7 \times 10^7$
2011 Jun. 4	20:51:42	22:52:20	0	0.002	$< 1.7 \times 10^7$
2012 Jul. 23	01:19:07	03:19:45	0	0.002	$< 1.7 \times 10^7$
2014 Dec. 13	13:06:34	15:07:12	0	0.002	$< 1.7 \times 10^7$

For the high-energy data set, we considered reactions of all neutrino flavors because the distance between the Sun and the Earth is sufficiently long compared with the oscillation length of neutrinos whose energy is less than 100 GeV [118]. The flavor ratio of solar flare neutrinos at the production point is $\nu_e : \nu_\mu : \nu_\tau = 1 : 2 : 0$ due to its origin from $\pi^\pm$ and $\mu^\pm$ decays while the flavor ratio at the detector is approximately $\nu_e : \nu_\mu : \nu_\tau = 1 : 1 : 1$, where we also assume that the ratio of neutrino to anti-neutrino is approximately equal, as $\nu : \bar{\nu} = 1 : 1$. The fluence limit of solar flare neutrino using the high-energy sample can be obtained by a similar procedure to the one for the low-energy sample. The difference in the calculation procedure of the upper limit between the high and the low-energy data sets is the definition of the probability density function of the number of observed events. For the high-energy data set, it is defined as follows:

$$\begin{aligned} P_{\mathrm{High}}(S+B|n_{\mathrm{obs}}) &= \frac{1}{A'}\iiint \frac{\mathrm{e}^{-(S+B)}(S+B)^{n_{\mathrm{obs}}}}{n_{\mathrm{obs}}!} \\ &\times G(\Delta\sigma(E_\nu))G(\Delta\varepsilon_{\mathrm{High}})G(\Delta B)\mathrm{d}(\Delta\sigma(E_\nu))\mathrm{d}(\Delta\varepsilon_{\mathrm{High}})\mathrm{d}(\Delta B), \quad (7.3.8) \\ S &= N_T t_{\mathrm{emit}} \int \mathrm{d}E_\nu \sum_{i=e,\mu,\tau,\bar{e},\bar{\mu},\bar{\tau}} \left(\frac{F(E_{\nu_i})\sigma(E_{\nu_i})\varepsilon_{\mathrm{High}}(E_{\nu_i})}{6}\right), \quad (7.3.9) \end{aligned}$$

where N_T is the number of target nuclei relevant to the neutrino interactions, $F(E_\nu)$ is the expected energy spectrum from each theoretical model [42–44], $\sigma(E_\nu)$ is the combined cross section for all interactions, and $\varepsilon_{\mathrm{High}}(E_\nu)$ is the reduction efficiency of the high-energy sample. Figure 7.28 shows a comparison between fluence prediction from solar flare neutrino models and the upper limits in this study. The Fargion's model is experimentally excluded. The Kocharov's model will be testified by the next-generation neutrino detector such as Hyper-K. The Takeishi's model is difficult to test even if the next-generation neutrino detector.

Fargion and Moscato [42] define energy conversion factor, η, as the amount of energy carried away by $\pi^\pm$ out of the total energy of a solar flare. If the total energy of a solar flare is known, the energy conversion factor can be calculated by using our result, based on the following equation:

$$n_{\mathrm{obs}} = 7.5\eta\left(\frac{E_{\mathrm{FL}}}{10^{31}\ \mathrm{erg}}\right) \quad (7.3.10)$$

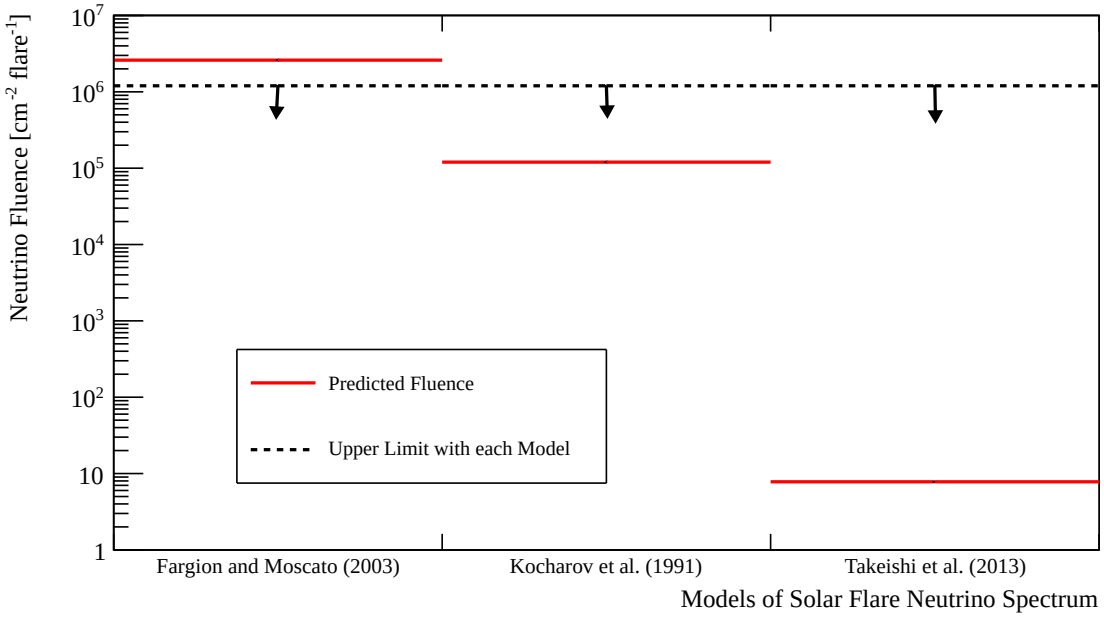

Figure 7.28: The comparison between predicted fluence by solar flare neutrino models and fluence upper limits obtained in this study. Red solid lines (black dashed line) show predicted neutrino fluence of each model (fluence upper limit).

where E_{FL} is the total energy of solar flare and n_{obs} is observed event in SK. According to Ref. [61], The total energy of the solar flare event that occurred on November 4th, 2003 is estimated to be 1.3×10^{34}erg. In the case of this solar flare, the energy conversion factor is determined as $\eta = 0.004$, which is two order of magnitude smaller than the estimation by Fargion and Moscato [42]. Therefore, this experimental result suggests that the theoretical assumption of energy conversion during solar flares should be re-considered. The 90% C.L. upper limits of the fluence for solar flare neutrino in the high-energy data sample in each flare are summarized in Tables 7.5 and 7.6.

Table 7.5: The summary of fluence upper limits at 90% C.L. for the high-energy sample. We assumed the energy spectrum from Fargion and Moscato [42] and the neutrino interactions from Hayato et. al [84]. The search time windows are same as in Table 3.9

Date	Derivative of soft X-rays		Line γ-ray (RHESSI)		Number of candidate	Expected background	Fluence limits
	Start	End	Start	End	event [event]	rate [event/flare]	[$\mathrm{cm}^{-2}\,\mathrm{flare}^{-1}$]
1997 Nov. 6	11:52:13	11:54:58	–	–	0	0.04	$< 5.6 \times 10^5$
2000 Jul. 14	10:08:44	10:28:31	–	–	0	0.20	$< 5.6 \times 10^5$
2001 Apr. 2	21:35:10	21:52:57	–	–	0	0.20	$< 5.6 \times 10^5$
2001 Apr. 6	19:12:32	19:21:31	–	–	0	0.10	$< 5.6 \times 10^5$
2001 Apr. 15	13:43:48	13:51:03	–	–	0	0.08	$< 5.6 \times 10^5$
2001 Aug. 25	16:28:36	16:33:38	–	–	No SK data	-	-
2001 Dec. 13	14:24:25	14:31:05	–	–	No SK data	-	-
2002 Jul. 23	00:25:08	00:31:36	00:26:28	00:56:22	No SK data	-	-
2003 Oct. 23	08:20:32	08:36:03	–	–	0	0.16	$< 5.6 \times 10^5$
2003 Oct. 28	10:59:30	11:10:57	–	–	0	0.12	$< 5.6 \times 10^5$
2003 Oct. 29	20:38:46	20:50:07	–	–	0	0.12	$< 5.6 \times 10^5$
2003 Nov. 2	17:12:01	17:26:03	17:14:14	17:36:41	0	0.14	$< 5.6 \times 10^5$
2003 Nov. 4	19:36:59	19:56:03	–	–	1	0.20	$< 8.5 \times 10^5$
2005 Jan. 20	06:39:22	06:57:12	06:42:54	07:09:52	0	0.18	$< 5.6 \times 10^5$
2005 Sep. 7	17:23:34	17:39:48	–	–	0	0.18	$< 5.6 \times 10^5$
2005 Sep. 8	21:00:27	21:08:05	–	–	0	0.08	$< 5.6 \times 10^5$
2005 Sep. 9	19:13:00	21:20:36	–	–	0	0.67	$< 5.6 \times 10^5$
2006 Dec. 5	10:24:18	10:35:43	–	–	0	0.12	$< 5.6 \times 10^5$
2006 Dec. 6	18:41:29	18:47:06	–	–	0	0.06	$< 5.6 \times 10^5$
2011 Aug. 9	08:00:50	08:05:40	–	–	0	0.06	$< 5.6 \times 10^5$
2012 Mar. 7	00:04:21	00:25:16	–	–	0	0.20	$< 5.6 \times 10^5$
2017 Sep. 6	11:54:39	12:03:20	–	–	1	0.12	$< 8.9 \times 10^5$
2017 Sep. 10	15:49:12	16:06:32	–	–	0	0.18	$< 5.6 \times 10^5$

Table 7.6: The summary of fluence upper limits at 90% C.L. for the high-energy sample for solar flares on the invisible side. We assumed the energy spectrum from Fargion and Moscato [42] and the neutrino interactions from Hayato et. al [84]. The search time windows are same as in Table 3.10

Date	Search Time Window		Number of candidate	Expected background	Fluence limits
	Start	End	event [event]	rate [event/flare]	[$\mathrm{cm}^{-2}\,\mathrm{flare}^{-1}$]
2001 Apr. 18	01:15:24	03:16:02	0	0.62	$< 5.6 \times 10^5$
2002 Jul. 18	18:07:20	20:07:58	No SK data	-	-
2002 Jul. 19	15:13:34	17:14:12	No SK data	-	-
2003 Nov. 2	08:09:23	10:10:01	0	0.62	$< 5.6 \times 10^5$
2003 Nov. 7	14:41:19	16:41:57	2	0.62	$< 1.2 \times 10^6$
2003 Nov. 9	05:06:57	07:45:29	0	0.62	$< 5.6 \times 10^5$
2005 Jul. 24	12:44:51	14:45:29	2	0.62	$< 1.2 \times 10^6$
2011 Jun. 4	20:51:42	22:52:20	1	0.62	$< 8.2 \times 10^5$
2012 Jul. 23	01:19:07	03:19:45	1	0.62	$< 8.2 \times 10^5$
2014 Dec. 13	13:06:34	15:07:12	0	0.62	$< 5.6 \times 10^5$

To compare the results of this work with the other experimental results, the model-independent fluence upper limit was also calculated for the low-energy sample. In this case, the probability density function at an energy E is defined as follows:

$$\begin{aligned} P_{\mathrm{Low}}(S+B|n_{\mathrm{obs}})(E) &= \frac{1}{A}\iiint \frac{\mathrm{e}^{-(S(E)+B)}(S(E)+B)^{n_{\mathrm{obs}}}}{n_{\mathrm{obs}}!} \\ &\times G(\Delta\sigma_{\mathrm{IBD}})G(\Delta\varepsilon_{\mathrm{Low}})G(\Delta B)\mathrm{d}(\Delta\sigma_{\mathrm{IBD}})\mathrm{d}(\Delta\varepsilon_{\mathrm{Low}})\mathrm{d}(\Delta B), \quad (7.3.11) \\ S(E) &= N_p t_{\mathrm{emit}} \int F(E_\nu)\theta(E,E_\nu)\sigma_{\mathrm{IBD}}(E_\nu)\varepsilon_{\mathrm{Low}}(E_\nu)\mathrm{d}E_\nu \quad (7.3.12) \end{aligned}$$

where $\theta(E, E_\nu)$ is a function which is defined as,

$$\theta(E,E_\nu) = \begin{cases} 1\ (E - 5\ \mathrm{MeV} < E_\nu \leq E + 5\ \mathrm{MeV}) \\ 0\ (\mathrm{otherwise}), \end{cases} \quad (7.3.13)$$

and other variables and functions are same as that used in Eq. (7.3.2). The fluence limit was calculated every 10 MeV in the energy range from 20 to 120 MeV. Figure 7.29 shows the results of the upper limits of fluence for solar flare neutrinos with the model-independent method. Compared to the Kamiokande-II result [52], the sensitivity was improved by an order of magnitude in the energy region from 20 to 110 MeV. SNO, Borexino, and KamLAND collaborations searched for neutrinos from solar flares in the energy range of MeV by analyzing light curves from the GOES satellite. Because their methods (as well as assumptions) differ from each other, we can not directly compare the experimental results with these results.

7.4 Discussions and Future Prospects

Neutrinos from solar flares are important to understand the mechanism of proton acceleration at the astrophysical site. For solar flares that occurred on the visible and invisible sides, we firstly estimated the time of neutrino emission from optical light curves and CMEs observations by the

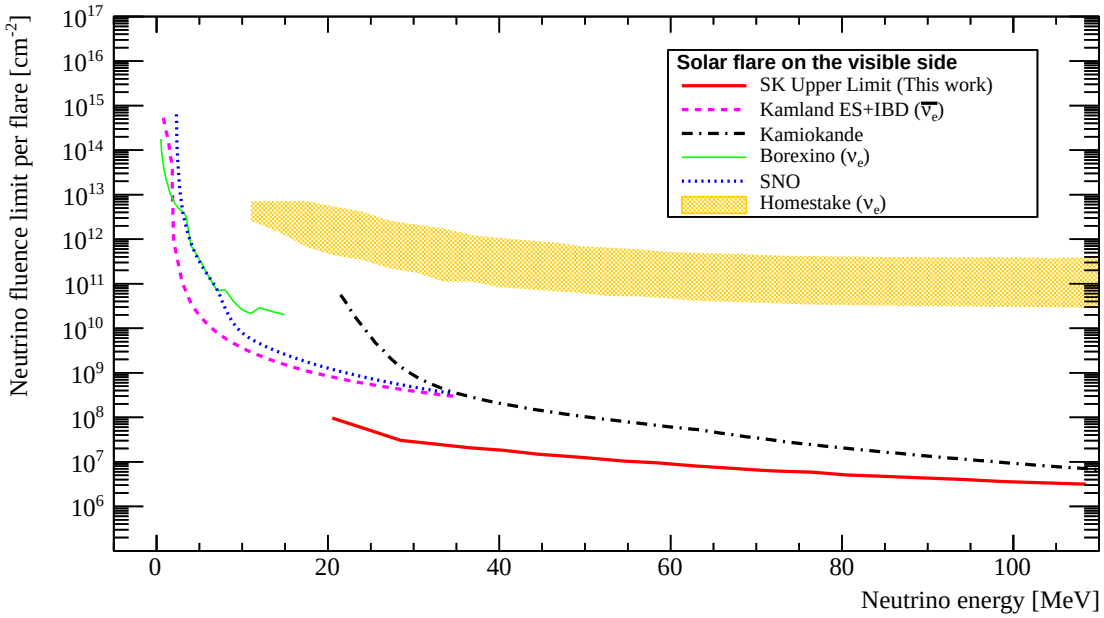

Figure 7.29: The fluence limit obtained by the SK-I, II, III, and IV (red thick-solid) together with the other experimental results by Kamiokande (black long-dashed-dotted) [52], KamLAND (pink dashed) [119], Borexino (Green thin-solid) [54], SNO (blue dotted) [53] below 100 MeV. The results from other experiments have been scaled to fit the definition of calculation in this study.

solar satellites. Then, we searched for neutrino events coincident with solar flares in the Super-Kamiokande detector. Two neutrino events from solar flares occurring on the visible side, while six neutrino events from solar flares that occurred on the invisible side were observed, but all of them are consistent with the background rate estimated from the usual data of the SK detector. Since no significant excess of events is observed, we obtained the upper limit of the solar flare neutrino fluence. For example, the fluence limit at 90% C.L. for the largest solar flare with the class of X28.0 occurring on the visible side of the Sun on November 4th, 2003 is 8.5×10^5 cm^{-2}. In addition, the fluence limit for the solar flare occurring on the invisible side on November 7th, 2003, which followed the largest solar flare from April 1996 to May 2018, is 1.2×10^6 cm^{-2}.

In order to compare the results with the other experimental fluence limits, the model-independent fluence limit is also obtained below 100 MeV. Our result gave the most stringent upper limit on the fluence of solar flare neutrinos.

In July 2020, 13 tons of $Gd_2(SO_4)_3 \cdot 8H_2O$ (gadolinium sulfate octahydrate) was dissolved into the detector's water tank in order to improve its neutron detection efficiency. This Gd loading is mainly motivated to increase the detector's sensitivity to the diffuse supernova anti-electron neutrinos by applying the delayed coincidence technique between primary neutrino interaction and about 8 MeV γ-rays from Gd-neutron capture due to large neutron cross-section of Gd [120]. This technique also enhances the sensitivity to solar flare neutrinos as well. In addition to SK-Gd, further searches are required to understand the production of solar flare neutrinos by the large scale neutrino detectors such as Hyper-Kamiokande [45], IceCube gen-2 [121], and JUNO [122] during the next solar cycle 25 staring from the late 2019. The fiducial volume of Hyper-K is about ten times that of Super-K. Assuming that the reduction efficiency of Hyper-K is the same as that of Super-K, the sensitivity of the solar flare neutrino detection is estimated to be about six times better.

In this study, we searched for solar flare neutrinos coincident with the impulsive phase of solar flares. On the other hand, the late arrival of prompt solar charged particles results in the delayed neutrino flux originating from the collisions with the Earth's atmosphere. Search for neutrinos originated from the long time-scale acceleration would be an interesting topic in future.

Chapter 8

Conclusion

We have performed searches for neutrinos associated with solar flares with the Super-Kamiokande detector. Neutrinos from solar flares are important to understand the mechanism of proton acceleration at the astrophysical site. When the protons are traveling downward towards the solar core along with the magnetic field line, a beam-like acceleration of protons efficiently collides with a nucleus in the dense plasma. Such a process results in enhancing the production rate of the neutrinos. If this beam-like acceleration occurs on the invisible side of the Sun, the large neutrino intensity at the neutrino detectors at the Earth would be expected.

The first step of the solar flare neutrino search was to select the large solar flares and estimate the neutrino emission time for both the visible and invisible sides of the Sun. Twenty-three solar flares on the visible side above the X5.0 class, and ten solar flares accompanied with CMEs whose emission speed is faster than 2000 $\mathrm{km\,s^{-1}}$ on the invisible side occurring between April 1996 and May 2018 were selected. For solar flares occurring on the visible side, we estimated the time of neutrino emission from optical light curves which are observed by the solar satellites. For solar flares occurring on the invisible side, we set the search time window from CMEs observations. The average duration of the search windows used in this study are 700 s (derivative of soft X-ray by GOES) and 1586 s (line γ-ray by RHESSI) for the visible side solar flares. We conservatively set the search time window of 7238 s/flare (3060 s before the time of CMEs emission and 4178 s after the time of CME emission), where this duration is determined from the study of the visible side solar flares, since all processes, such as acceleration, energy release, etc, occurring during a solar flare complete within this time duration. As a result, the average background rate for a solar flare in Super-Kamiokande becomes 0.24 event/flare for the visible side and 0.62 event/flare for the invisible side.

Then, we searched for neutrino events coincident with the solar flares in the Super-Kamiokande detector. The SK data is divided into two samples as high-energy samples (above 100 MeV) and low-energy samples (16 - 100 MeV). For the three solar flares on the visible side, the SK data is not available because the SK detector was under reconstruction. Therefore, the number of solar flares on the visible side for solar flare neutrino search is twenty. No low-energy neutrino candidates are found in the search time windows while the backgrond rate is 0.001 event/flare. On the other hands, there are two solar flares occurring on the visible side of the Sun with one high-energy neutrino candidate in the search time windows. For the other solar flares on the visible side, there are not any neutrino candidates. The solar flares with the neutrino candidate occurred on November 4th, 2003, and September 6th, 2017, and background rates are 0.20 event/flare and 0.12 event/flare, respectively. The probabilities that the neutrino candidate is from a background source are 18.1% and 11.3%, respectively. So we have concluded they are

consistent with the background rate.

For the solar flares occurring on the invisible side of the Sun, the SK data is not available for the two solar flares because of the reconstruction work of the SK detector. Hence, we have searched for solar flare neutrinos by using eight solar flares occurring on the invisible side, finally. No low-energy neutrino candidates are found in the search time windows while the backgrond rate is 0.002 event/flare. There are two solar flares with two high-energy neutrino candidates and two solar flares with one high-energy neutrino candidate. There are not any neutrino candidates with the other four solar flares. The background rate for each solar flare on the invisible side is 0.62 event/flare. The probabilities that the neutrino candidates are from background sources are 12.8% for solar flares with two neutrino candidates and 46.2% for solar flares with one neutrino candidate, respectively. So we have concluded they are also consistent with the background rate. It is the first time that the solar flare neutrino search from solar flares on the invisible side of the Sun has been carried out.

Based on the observed events within the search window, the upper limit of the solar flare neutrino fluence was calculated for each solar flare. The fluence upper limits at 90% C.L. for the solar flares occurring on the visible side of the Sun without neutrino candidates are 5.6×10^5 cm^{-2}. For the solar flares occurring on the invisible side of the Sun, The fluence upper limits at 90% C.L. in the energy region from 100 MeV to 10 GeV are 5.6×10^5 cm^{-2}, 8.2×10^5 cm^{-2} and 1.2×10^6 cm^{-2} for solar flares with zero, one and two neutrino candidates, respectively. The fluence upper limit for the solar flare occurring on November 4th, 2003 is 8.5×10^5 cm^{-2}. This is the largest solar flare since 1996. From the obtained fluence upper limit, the upper limit on the conversion factor, η, which is the efficiency of energy conversion from the total energy of solar flare to the energy of the neutrinos, is estimated based on Fargion and Moscato [42]. In the case of the largest solar flare on November 4th, 2003, it is determined as $\eta < 0.004$, which is two orders of magnitude smaller than the estimation by Fargion and Moscato [42]. Therefore, this experimental result suggests that the theoretical assumption adopted in Ref. [42] of the energy conversion during solar flares should be re-considered. In addition, the fluence upper limit at 90% C.L. for the solar flare occurring on the invisible side on November 7th, 2003, which followed the largest solar flare, is 1.2×10^6 cm^{-2}. From the comparison between the fluence upper limit and prediction of the solar flare neutrino fluence expected by the theoretical model [42] of Fargion and Moscato, we have concluded the theoretical model is excluded. The fluence upper limits at 90% C.L. in the energy region from 16 to 100 MeV for the solar flares occurring on the visible and invisible side of the Sun are 1.7×10^7 cm^{-2}. In order to compare the results with the fluence limits from other experiments, the model independent fluence upper limit below 100 MeV is also obtained. The result does not rule any theoretical models but gives the most stringent upper limits on the fluence of solar flare neutrinos in the tens of MeV region.

Reference

[1] R. Davis, Progress in Particle and Nuclear Physics 32 (1994) 13–32.

[2] K. S. Hirata *et al.*, Phys. Rev. D 38 (1988) 448–458.

[3] M. Aartsen *et al.*, Science 361 (6398) (2018) eaat1378.

[4] Y. Fukuda *et al.* (Super-Kamiokande Collaboration), Phys. Rev. Lett. 81 (1998) 1562–1567.

[5] Q. R. Ahmad *et al.* (SNO Collaboration), Phys. Rev. Lett. 87 (2001) 071301.

[6] B. Pontecorvo, Zh. Eksp. Teor. Fiz. 37 (1959) 1751–1757.

[7] Z. Maki, M. Nakagawa, S. Sakata, Progress of Theoretical Physics 28 (5) (1962) 870–880.

[8] K. Abe *et al.* (Super-Kamiokande Collaboration), Phys. Rev. D 94 (2016) 052010.

[9] B. Aharmim *et al.* (SNO Collaboration), Phys. Rev. C 72 (2005) 055502.

[10] S. Abe *et al.* (The KamLAND Collaboration), Phys. Rev. Lett. 100 (2008) 221803.

[11] K. Abe *et al.* (Super-Kamiokande Collaboration), Phys. Rev. D 97 (2018) 072001.

[12] M. H. Ahn *et al.* (K2K Collaboration), Phys. Rev. D 74 (2006) 072003.

[13] P. Adamson *et al.* (MINOS Collaboration), Phys. Rev. Lett. 106 (2011) 181801.

[14] K. Abe *et al.* (T2K Collaboration), Phys. Rev. Lett. 111 (2013) 211803.

[15] J. K. Ahn *et al.* (RENO Collaboration), Phys. Rev. Lett. 108 (2012) 191802.

[16] A. Y *et al.*, Physical Review D 86 (2012) 052008.

[17] K. Abe *et al.* (T2K Collaboration), Phys. Rev. Lett. 112 (2014) 061802.

[18] K. Abe *et al.*, Nature 580 (7803) (2020) 339–344.

[19] S. R. Kane, Impulsive /flash/ phase of solar flares - Hard X-ray, microwave, EUV and optical observations, in: G. A. Newkirk (Ed.), Coronal Disturbances, Vol. 57 of IAU Symposium, 1974, pp. 105–141, provided by the SAO/NASA Astrophysics Data System.

[20] K. Shibata *et al.*, Publications of the Astronomical Society of Japan 65 (3) (2013) 49.

[21] A. Jafari, E. T. Vishniac, arXiv: High Energy Astrophysical Phenomena.

[22] T. Yokoyama, K. Shibata, The Astrophysical Journal 549 (2) (2001) 1160–1174.

[23] G. Heckman *et al.*, NOAA Space Environment Center mission and the GOES space environment monitoring subsystem, Vol. 2812 of Society of Photo-Optical Instrumentation Engineers (SPIE) Conference Series, 1996, pp. 274–280.

[24] N. W. M., Astro Physical Journal Letter 153 (1968) L59.

[25] E. L. Chupp *et al.*, Nature 241 (1973) 333–335.

[26] D. M. Smith *et al.*, Astrophys. J. 595 (2003) L81–L84.

[27] V. Domingo, B. Fleck, A. I. Poland, Solar Physics 162 (1) (1995) 1–37.

[28] G. E. Brueckner *et al.*, Solar Physics 162 (1) (1995) 357–402.

[29] S. Yashiro *et al.*, Journal of Geophysical Research: Space Physics 109 (A7).

[30] E. Fermi, Phys. Rev. 75 (1949) 1169–1174.

[31] M. J. Aschwanden, Particle Acceleration and Kinematics in Solar Flares, Springer, 2003.

[32] Z. E. Forman M.A., Ramaty R..

[33] B. A. Tverskoĭ, Soviet Journal of Experimental and Theoretical Physics 25 (1967) 317.

[34] A. A. Korchak, solar physics 56 (1) (1978) 223–234.

[35] L. Vlahos, solar physics 121 (1-2) (1989) 431–447.

[36] J. A. Miller *et al.*, Journal of Geophysical Research 102 (A7) (1997) 14631–14660.

[37] J. Bednarz, M. Ostrowski, Monthly Notices of the Royal Astronomical Society 283 (2) (1996) 447–456.

[38] R. G. Giovanelli, Month Notices Royal Astron Soc 107 (1947) 338.

[39] R. M. Wilson, Astrophys. J. 545 (2000) 532–546.

[40] O. M. Boyarkin, Phys. Rev. D 53 (1996) 5298–5309.

[41] O. Boyarkin, G. Boyarkina, Astropart.. Phys. 85 (2016) 39 – 42.

[42] D. Fargion, Journal of High Energy Physics 2004 (06) (2004) 045.

[43] G. E. Kocharov, G. A. Kovaltsov, I. G. Usoskin, Nuovo Cim. C14 (1991) 417–422.

[44] R. Takeishi, T. Terasawa, J. Kotoku, Numerical Studies of Neutrino Radiation in Solar Flares, in: International Cosmic Ray Conference, Vol. 33 of International Cosmic Ray Conference, 2013, p. 3656.

[45] K. Abe *et al.* (2018).
URL `https://ui.adsabs.harvard.edu/#abs/2018arXiv180504163H/abstract`

[46] H. Hudson, J. Ryan, Annu. Rev. Astron. Astrophys. 33 (1995) 239–282.

[47] R. Ramaty, B. Kozlovsky, R. E. Lingenfelter, Space Sci. Rev. 18 (1975) 341–388.

[48] J. N. Bahcall, G. B. Field, W. H. Press, Astrophys. J. Lett. 320 (1987) L69.

[49] J. N. Bahcall, Phys. Rev. Lett. 61 (1988) 2650–2652.

[50] A. Cisneros, Astrophys. Spa. Sci. 10 (1971) 87–92.

[51] L. B. Okun, M. B. Voloshin, M. I. Vysotsky, Sov. Phys. JETP 64 (1986) 446–452.

[52] K. S. Hirata *et al.*, Phys. Rev. Lett. 61 (1988) 2653–2656.

[53] B. Aharmim *et al.*, Astropart. Phys. 55 (2014) 1–7.

[54] M. Agostini *et al.*, Astroparticle Physics 125 (2021) 102509.

[55] S. Fukuda *et al.*, Nuclear Instruments and Methods in Physics Research Section A: Accelerators, Spectrometers, Detectors and Associated Equipment 501 (2) (2003) 418 – 462.

[56] T. Ymaguchi, Observation of 8b solar neutrinos from 300-day data at super-kamiokande, Ph.D. thesis, The University of Osaka (1998).

[57] Y. Nakano *et al.*, Nuclear Instruments and Methods in Physics Research Section A: Accelerators, Spectrometers, Detectors and Associated Equipment 977 (2020) 164297.

[58] H. Nishino *et al.*, Nuclear Instruments and Methods in Physics Research Section A: Accelerators, Spectrometers, Detectors and Associated Equipment 610 (3) (2009) 710–717.

[59] S. Yamada *et al.*, IEEE Transactions on Nuclear Science 57 (2) (2010) 428–432.

[60] G. de Wasseige (2016).
URL `https://ui.adsabs.harvard.edu/abs/2016arXiv160600681D`

[61] S. R. Kane, J. M. McTiernan, K. Hurley, Astron and Astrophysics 433 (2005) 1133–1138.

[62] A. Veronig *et al.*, Astro and Astrophysics 392 (2002) 699–712.

[63] V. Kurt *et al.*, Advances in Astronomy 2013 (2013) 690921.

[64] S. N. Kuznetsov *et al.*, Solar Physics 268 (1) (2011) 175–193.

[65] K. Hurley *et al.*, Astron and Astrophyics 92 (2) (1992) 401–410.

[66] M. Yoshimori *et al.*, Astrophysical Journal 90 (1994) 639.

[67] R. Lin *et al.*, Solar Phys. 210 (2002) 3–32.

[68] J. Kiener *et al.*, Astro and Astrophysics 445 (2) (2006) 725–733.

[69] J. W. Bieber *et al.*, Geophysical Research Letters 32 (3).

[70] W. Q. Gan, Astrophys. J. 496 (1998) 992–997.

[71] T. Mukai *et al.*, J. Geomag. Geoelectr. 46 (1994) 669–692.

[72] T. Terasawa *et al.*, Nature 434 (2005) 1110–1111.

[73] Y. T. Tanaka *et al.*, Astrophys. J. 665 (2007) L55–L58.

[74] Y. T. Tanaka *et al.*, Rev. Sci. Instrum. 78 (2007) 034501–034501.

[75] A. Y. Shih, R. P. Lin, D. M. Smith, Astrophys. J. 698 (2009) L152–L157.

[76] M. L. Kaiser *et al.*, Society for Scientific Study of Reading 136 (1-4) (2008) 5–16.

[77] C. J. Davis *et al.*, Geophysical Research Letters 36 (8) (2009) L08102.

[78] B. Zhu *et al.*, Astrophysical Journal 827 (2) (2016) 146.

[79] M. D. Andrews, Solar Physics 218 (1) (2003) 261–279.

[80] K. Abe *et al.*, Nuclear Instruments and Methods in Physics Research Section A: Accelerators, Spectrometers, Detectors and Associated Equipment 737 (2014) 253–272.

[81] R. M. Pope, E. S. Fry, Appl. Opt. 36 (33) (1997) 8710–8723.

[82] K. Abe *et al.* (Super-Kamiokande Collaboration), Phys. Rev. D 97 (2018) 072001.

[83] M. Nakahata *et al.*, Nuclear Instruments and Methods in Physics Research Section A: Accelerators, Spectrometers, Detectors and Associated Equipment 421 (1) (1999) 113–129.

[84] Y. Hayato, AcPP B. 40 (2009) 2477–2489.

[85] C. H. L. Smith, Physics Reports (3) (1972) 261.

[86] S. J. Barish *et al.*, Phys. Rev. D 16 (1977) 3103–3121.

[87] N. J. Baker *et al.*, Phys. Rev. D 23 (1981) 2499–2505.

[88] M. Pohl *et al.*, Lettere al Nuovo Cimento (1971-1985) 26 (11) (2007) 332.

[89] N. J. Baker *et al.*, Phys. Rev. D 23 (1981) 2499–2505.

[90] J. Brunner *et al.*, Zeitschrift für Physik C Particles and Fields 45 (4) (1990) 551–555.

[91] A. A. Aguilar-Arevalo *et al.* (MiniBooNE Collaboration), Phys. Rev. Lett. 100 (2008) 032301.

[92] J. Nieves, I. R. Simo, M. J. V. Vacas, Phys. Rev. C 83 (2011) 045501.

[93] G. M. Radecky *et al.*, Phys. Rev. D 25 (1982) 1161–1173.

[94] D. Hill *et al.*, Phys. Rev. Lett. 30 (1973) 239–242.

[95] S. J. Barish *et al.*, Phys. Rev. D 19 (1979) 2521–2542.

[96] P. Allen *et al.*, Nuclear Physics B 264 (1986) 221–242.

[97] A. Aurilia, H. Nicolai, P. Townsend, Nuclear Physics B 176 (2) (1980) 509–522.

[98] O. Espinosa, Nuclear Physics B 343 (2) (1990) 310–340.

[99] T. Kitagaki *et al.*, Phys. Rev. D 34 (1986) 2554–2565.

[100] J. Bell *et al.*, Phys. Rev. Lett. 41 (1978) 1008–1011.

[101] D. Rein, L. M. Sehgal, Annals of Physics 133 (1) (1981) 79–153.

[102] P. S. Auchincloss *et al.*, Zeitschrift für Physik C Particles and Fields 48 (3) (1990) 411–431.

[103] P. O. Berge *et al.*, Zeitschrift für Physik C Particles and Fields 35 (1987) 443–452.

[104] S. Ciampolillo *et al.*, Physics Letters B 84 (1979) 281–284.

[105] J. Allaby *et al.*, Zeitschrift fr Physik C 38 (1988) 403–410.

[106] G. S. Abrams *et al.*, Phys. Rev. Lett. 25 (1970) 617–621.

[107] C. Baltay *et al.*, Phys. Rev. Lett. 44 (1980) 916–919.

[108] S. O. D. C. Colley, G. T. Jones, Zeitschrift für Physik C Particles and Fields 2 (1979) 39.

[109] V. B. Anikeev *et al.*, Zeitschrift fuer Physik, C 70 (1996) 39–46.

[110] D. MacFarlane *et al.*, Zeitschrift fuer Physik C 26 (1984) 1–12.

[111] D. Baranov *et al.*, Physics Letters B 81 (2) (1979) 255–257.

[112] D. Rein, L. M. Sehgal, Nuclear Physics B 223 (1) (1983) 29–44.

[113] A. Strumia, F. Vissani, Physics Letters B 564 (1) (2003) 42–54.

[114] M. Shiozawa, Nuclear Instruments and Methods in Physics Research Section A: Accelerators, Spectrometers, Detectors and Associated Equipment 433 (1) (1999) 240–246.

[115] M. Ikeda, Precise measurement of solar neutrinos with super-kamiokande iii, Ph.D. thesis, The University of Tokyo (2009).
URL `http://www-sk.icrr.u-tokyo.ac.jp/sk/_pdf/articles/ikeda-dron.pdf`

[116] Y. Nakano, ^{8}B solar neutrino spectrum measurement using Super-Kamiokande IV, Ph.D. thesis, The University of Tokyo (2016).
URL `http://www-sk.icrr.u-tokyo.ac.jp/sk/_pdf/articles/2016/doc_thesis_naknao.pdf`

[117] K. Watanabe *et al.*, The Astrophysical Journal 636 (2008) 1135.

[118] G. L. Fogli *et al.*, Physical Review Letters 74 (9) (2006) 093004.

[119] S. Abe *et al.*, arXiv e-prints (2021) arXiv:2105.02458.

[120] M. B. Chadwick *et al.*, Nuclear Data Sheets 112 (12) (2011) 2887–2996.

[121] M. G. Aartsen *et al.*, J. Phys. G 48 (2021) 060501.

[122] T. Adam *et al.*, arXiv e-prints (2015) arXiv:1508.07166.